

MODELING, HARDWARE-IN-THE-LOOP SIMULATIONS AND CONTROL DESIGN
FOR A VERTICAL AXIS WIND TURBINE WITH HIGH SOLIDITY

by

AYKUT ÖZGÜN ÖNOL

Submitted to the Graduate School of Engineering and Natural Sciences
in partial fulfillment of the requirements for the degree of
Master of Science

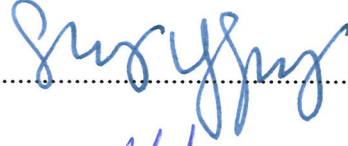
Sabanci University

August 2016

MODELING, HARDWARE-IN-THE-LOOP SIMULATIONS AND
CONTROL DESIGN FOR A VERTICAL AXIS WIND TURBINE WITH
HIGH SOLIDITY

APPROVED BY:

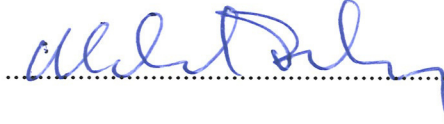
Prof. Dr. Serhat Yeşilyurt
(Thesis Supervisor)



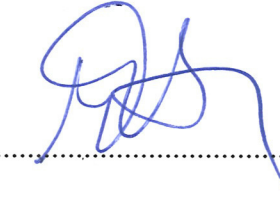
Assoc. Prof. Dr. Ahmet Onat
(Thesis Co-advisor)



Assoc. Prof. Dr. Melih Papila



Assist. Prof. Dr. Meltem Elitaş



Prof. Dr. Ata Muğan



DATE OF APPROVAL: 02/08/2016.....

© Aykut Özgün Önel 2016

All Rights Reserved

ABSTRACT

MODELING, HARDWARE-IN-THE-LOOP SIMULATIONS AND CONTROL DESIGN FOR A VERTICAL AXIS WIND TURBINE WITH HIGH SOLIDITY

AYKUT ÖZGÜN ÖNOL

Mechatronics Engineering, Master's Thesis, August 2016

Thesis Advisor: Prof. Dr. Serhat Yeşilyurt

Thesis Co-advisor: Assoc. Prof. Dr. Ahmet Onat

Keywords: Vertical axis wind turbine, computational fluid dynamics modeling, hardware-in-the-loop simulation, model predictive control, maximum power point tracking

Vertical axis wind turbines (VAWTs) are advantageous in gusty, turbulent winds with rapidly changing direction such as surface winds by the virtue of their omnidirectional and simple design. Thus, a small-scale VAWT is favorable in urban areas, e.g., on top of a building, as well as in rural areas away from integrated grid systems where it can be used as a portable generator.

In this thesis, a methodology is presented for the assessment of overall performance for a small-scale VAWT system that consists of a three-straight-bladed rotor with high solidity, electromechanical and power electronics components and controller. Salient features of this approach include a validated computational fluid dynamics (CFD) model and a hardware-in-the-loop (HIL) simulation. The time-dependent, two-dimensional CFD model is coupled with the dynamics of the rotor subject to inertia and generator load. The HIL test-bed consists of an electrical motor, a gearbox, a generator, a rectifier and a programmable electronic load. In this setup, the electrical motor emulates the VAWT rotor. The HIL simulation is used to study the impact of electromechanical energy conversion on the overall performance and to evaluate control algorithms in real-time. For variable-speed control of the turbine, maximum power point tracking (MPPT) and model predictive control (MPC) algorithms and a simple MPC-mimicking control are designed and tested.

According to results, the coupled CFD model is an effective tool in evaluation of the realistic transient behavior of the VAWT including the inertial effects of the rotor and the feedback control; the electromechanical energy conversion has a profound effect on the power characteristics and the efficiency of the VAWT system; the MPC and MPC-mimicking control algorithms outperform the MPPT algorithms in terms of energy output by allowing deviations from the maximum power instantaneously for future gains in energy generation; and all of the controllers perform satisfactorily under step wind, wind gust and real wind conditions.

ÖZET

YÜKSEK KATILIKLI BİR DİKEY EKSENLİ RÜZGAR TÜRBİNİ İÇİN MODELLEME, DÖNGÜDE DONANIM SİMÜLASYONLARI VE KONTROL TASARIMI

AYKUT ÖZGÜN ÖNOL

Mekatronik Mühendisliği, Yüksek Lisans Tezi, Ağustos 2016

Tez Danışmanı: Prof. Dr. Serhat Yeşilyurt

Tez Yardımcı-danışmanı: Doç. Dr. Ahmet Onat

Anahtar kelimeler: Dikey eksenli rüzgar türbini, hesaplamalı akışkanlar dinamiği ile modelleme, döngüde donanım simülasyonu, model öngörülü kontrol, maksimum güç noktası izleyici

Dikey eksenli rüzgar türbinleri tüm-yönlü ve basit tasarımlarından dolayı yüzey rüzgarları gibi hızlı yön değiştiren, fırtınalı ve türbülanslı rüzgarlarda avantajlıdırlar. Dolayısıyla, küçük-ölçekli bir dikey eksenli rüzgar türbini hem kentsel alanlarda, mesela bir binanın tepesinde, hem de taşınabilir bir jeneratör olarak kullanılabilen bütünsel şebeke sistemlerinden uzak kırsal alanlarda elverişlidir.

Bu tezde, küçük ölçekli, üç düz kanatlı ve yüksek katıllıklı dikey eksenli rüzgar türbini, elektromekanik ve güç elektroniği bileşenleri ve kontrolörden oluşan sistemin genel performansının değerlendirilmesinde kullanılacak bir yöntem sunulmaktadır. Bu yaklaşımın öne çıkan özellikleri geçerli bir hesaplamalı akışkanlar dinamiği (HAD) modeli ve bir döngüde donanım simülasyonu (DDS) kullanılmasıdır. Zamana bağlı, iki boyutlu HAD modeli eylemsizliğe ve jeneratör yüküne bağlı olarak türbinin rotor dinamikleriyle bağlantılandırılmıştır. DDS düzeneği bir elektrik motoru, bir dişli kutusu, bir doğrultucu ve bir programlanabilir elektronik yükten oluşmaktadır. Bu sistemde, elektrik motoru dikey eksenli rüzgar türbininin rotoruna benzetilmektedir. DDS elektromekanik enerji dönüşümünün genel performans etkisini incelemek ve kontrol algoritmalarını gerçek zamanlı olarak denemek için kullanılmaktadır. Türbinin değişken hızlı kontrolü için, maksimum güç noktası izleyici ve model öngörülü kontrol algoritmaları ile model öngörülü kontrolü taklit edecek basit bir kontrol tasarlanmış ve test edilmiştir.

Elde edilen sonuçlara göre, rotor dinamiğiyle bağlantılı HAD modeli rotorun atalet etkileri ve geribeslemeli kontrol de dahil olmak üzere dikey eksenli rüzgar türbininin gerçekçi geçici performansının değerlendirilmesinde etkili bir araçtır; elektromekanik enerji dönüşümünün dikey eksenli rüzgar türbini sisteminin güç karakteristikleri ve verimliliği üzerinde önemli bir etkisi vardır; model öngörülü kontrol ve model öngörülü kontrolü taklit eden kontrol algoritmaları enerji üretimindeki gelecek kazançlar için anlık olarak maksimum güçten sapmalara izin vererek enerji çıkışı açısından maksimum güç noktası izleyicilerinden daha iyi performans göstermektedirler; ve tüm kontrolörler basamak rüzgar, rüzgar hamlesi ve gerçek rüzgar koşullarında başarılı şekilde çalışmaktadırlar.

ACKNOWLEDGEMENTS

First, and foremost, I would like to express my sincere gratitude to my advisor, Prof. Dr. Serhat Yeşilyurt. I am honored to have the opportunity to work with him. During the course of this work, he has not been only an outstanding advisor, who has given me insight into how to conduct world-class research, but also a very good mentor, whose guidance has shaped my thoughts and ideals.

I would also like to express my thanks to my co-advisor, Assoc. Prof. Dr. Ahmet Onat, for his guidance and support. In addition, I am thankful to Prof. Dr. Yeşilyurt and Assoc. Prof. Dr. Onat for providing me continuous financial support during my master's studies. I gratefully acknowledge that this work was supported by the Sabanci University Internal Research Grant Program (SU-IRG-985).

I would like to thank Assoc. Prof. Dr. Melih Papila, Asst. Prof. Dr. Meltem Elitaş and Prof. Dr. Ata Muğan for their careful evaluation of my thesis and useful comments.

I am obviously indebted to the best teammate, Uğur Sancar, for his tremendous contribution to this work as well as for being the amazing guy he is.

I am thankful to the lab members Alperen Acemoğlu, Osman Saygıner, Ebru Demir, Murat Gökhan Eskin, Fırat Yavuz and Hakan Osman Çaldağ for their invaluable friendship. I also want to thank Ozan Özdenizci, Oğuzcan Zengin and İsmail Yılmaz, who have made my graduate student life at Sabanci University more enjoyable. I would also like to state my special thanks to Sarah Thumbeck.

I am deeply grateful to my parents and brother, Gülseren, Hürriyet and Can, as well as my wife's parents, Sakine and Ferit, for their immense love and trust.

Finally, I would like to express my heartfelt gratitude and sincere appreciation to my beloved wife as well as my best friend, Sezen Yağmur, for her endless love, support (both emotional and technical), care and patience. I am very fortunate to have her by my side.

TABLE OF CONTENTS

1. Introduction	1
1.1. Motivation & Objective	3
1.2. Outline	4
2. Background & Contributions	5
2.1. Background	5
2.2. Contributions	10
3. Modeling	13
3.1. Rotor dynamics	13
3.2. Computational Fluid Dynamics Model.....	15
3.2.1. Geometry and Computational Domain	16
3.2.2. k- ϵ Turbulence Model.....	17
3.2.3. Time-dependent solver	18
3.2.4. Domain Size.....	19
3.2.5. Mesh.....	19
3.2.6. Convergence Studies.....	21
3.2.7. Validation.....	23
4. Control	29
4.1. Simple Dynamic Simulation.....	29
4.2. Wind Profiles	32
4.3. Maximum Power Point Tracking.....	34
4.3.1. Fixed-step Maximum Power Point Tracking Algorithm	37
4.3.2. Variable-step Maximum Power Point Tracking Algorithm	38
4.4. Model Predictive Control.....	38

4.5. Simple Nonlinear Control	41
5. Hardware-in-the-loop Simulation	45
5.1. Electromechanical Simulation	48
5.1.1. Validation of Electromechanical Model	51
5.2. Control	52
5.2.1. Maximum Power Point Tracking.....	53
5.2.2. Model Predictive Control.....	56
5.2.3. Simple Nonlinear Control.....	58
6. Results & Discussion	64
6.1. Computational Fluid Dynamics Simulation Results.....	64
6.1.1. Quasi-Steady Power Coefficient Curves	64
6.1.2. Flow Fields & Shaft Effect	70
6.1.3. Angle of Attack.....	71
6.1.4. Blade Forces	74
6.1.5. Transient Response to Gusts.....	77
6.1.6. Unsteady Power Coefficient	83
6.2. Simple Dynamic Simulation Results	91
6.2.1. Comparison of Simple Dynamic and CFD Simulations.....	91
6.2.2. Control Results	96
6.3. Hardware-in-the-loop Simulation Results	106
6.3.1. Electromechanical Simulation Control Results	108
6.3.2. Hardware-in-the-loop Simulation Control Results	117
6.4. Effect of Measurement Noise	123
6.5. Effect of Power Coefficient Oscillations and Inertia.....	127
6.6. Effect of Inertia on Steady-periodic Performance	129

7. Conclusions & Future Work	132
7.1. Conclusions.....	132
7.2. Future Work.....	135

LIST OF FIGURES

Figure 1.1: Rotor configurations for VAWT and HAWT [16].....	2
Figure 3.1: Morphing process of a cambered NACA0020 airfoil profile.	16
Figure 3.2: Geometry of the domain and boundary conditions in the CFD model.	17
Figure 3.3: Mesh configurations for (a) whole domain, (b) rotor, and (c) the blade.....	20
Figure 3.4: Angular velocity transients of the torque-free rotor for different finite-element mesh and domain sizes for $U = 6$ m/s.....	21
Figure 3.5: CFD model for validation of the k- ϵ turbulence model.	24
Figure 3.6: C_L and C_D values with respect to the angle of attack, α , obtained from simulations and experiments.	25
Figure 3.7: Experimental VAWT with the same dimensions used in the CFD model.....	27
Figure 3.8: Measured and simulated angular velocities as a function of the wind velocity.	27
Figure 3.9: Variation of rotor velocity throughout a coast-down test along with the estimated rotor velocity for $C_f = 0.0376$	28
Figure 4.1: Tip-speed ratio – power coefficient curve obtained from CFD simulations for $U = 6$ m/s.	30
Figure 4.2: Step wind profile.	32
Figure 4.3: Wind gust profile.....	33
Figure 4.4: Real wind data.	34
Figure 4.5: Rotor velocity – power output relation for a fixed wind velocity with the conditions for power maximization.	35
Figure 4.6: Flowchart of the ω -feedback MPPT algorithm.....	37
Figure 4.7: Rotor velocity (b), generator torque (c), and generator power (d) responses of the MPC for step wind (a).	42
Figure 4.8: Estimation of the lower and upper tip-speed ratio limits.	44
Figure 5.1: Schematics of the VAWT system (a) and the HIL test-bed (b) [16].....	46
Figure 5.2: An image of the HIL test-bed consisting of a PC (a), a dSPACE toolkit (b), a motor driver (c), an electrical motor (d), a gearbox (e), a generator (f), a rectifier (g), and a programmable electronic-load (h).	46
Figure 5.3: $\lambda - C_P$ curve used for HIL simulations.....	47

Figure 5.4: Three-phase PMSG – rectifier – load model (a) and the equivalent DC model (b) [16].....	49
Figure 5.5: Voltage drop (a) and power output (b) values for fixed rotor velocity and load current conditions obtained from HIL simulations and electromechanical simulations.	52
Figure 5.6: Flowchart of the V_L -feedback MPPT algorithm.....	55
Figure 5.7: Generator power coefficient map interpolated from electromechanical simulation data.....	59
Figure 5.8: Reference power output (a), load voltage (b), and rotor velocity (c) data points and corresponding polynomial fits.	60
Figure 5.9: Estimation of the lower and upper load voltage limits.....	61
Figure 5.10: Rotor velocity (b), load current (c), load voltage (d), and power output (e) responses of the MPC for step wind (a).....	62
Figure 6.1: Variations of the load coefficient (a), rotor velocity (b), generator torque (c), and power output (d) for C_P curve generation process in a low resolution simulation for $U = 10$ m/s.....	66
Figure 6.2: $\lambda - C_P$ curves obtained from low resolution simulations for steady wind velocities varying between 5 and 10 m/s.	67
Figure 6.3: Variation of the rotor velocity (a), generator torque (b) and power output (c) throughout high resolution simulations for different values of the load coefficient for $U = 6$ m/s.....	68
Figure 6.4: $\lambda - C_P$ curves obtained from low and high resolution simulations for $U = 6$ m/s.	69
Figure 6.5: Turbulence kinetic energy surface plots at high (a) and low (b) tip-speed ratios along with the zoomed in rotor views in (c) and (d), respectively, from a high resolution simulation for $U = 6$ m/s.	71
Figure 6.6: Top view of the rotor.....	72
Figure 6.7: Net incident velocity magnitude (a) and the angle of attack (b) with respect to the angular position for the blade 1 for $U = 6$ m/s.....	73
Figure 6.8: Thrust coefficient for a two-second period at quasi-steady-state of the load-torque-free simulation for $U = 6$ m/s with respect to azimuth angle.	75

Figure 6.9: Surfaces of the \mathbf{x} -velocity with arrows representing the velocity field at the minimum (a) and the maximum (b) values of the thrust coefficient.	75
Figure 6.10: Forces in Cartesian (a) and polar coordinates (b) acting on the blade 1 throughout a full revolution in quasi-steady regime for $\lambda = 1.26$ with respect to azimuth angle.	76
Figure 6.11: Small wind gust profile (a); dynamic responses of the load coefficient (b), rotor velocity (c), generator power (d), wind and generator torques (e), and the power coefficient (f).	79
Figure 6.12: Local and geometric estimations of the net incident velocity (a) and the angle of attack (b) vs the angular position for the blade 1 during the small gust.	80
Figure 6.13: Large wind gust profile (a); dynamic responses of the load coefficient (b), rotor velocity (c), generator power (d), wind and generator torques (e), and the power coefficient (f).	81
Figure 6.14: Radial (a) and tangential (b) forces acting on the blade 1 and the torque generated by the blade 1 during the large gust.	83
Figure 6.15: Unsteady C_P vs θ during the large gust.	84
Figure 6.16: Variation of the C_P oscillations and the amplitude of the oscillations with respect to the tip-speed ratio for the large gust.	85
Figure 6.17: Unsteady instantaneous and unsteady average per revolution $\lambda - C_P$ values during the large gust, and steady average, minimum and maximum per revolution $\lambda - C_P$ values.	86
Figure 6.18: Steady and unsteady average per revolution $\lambda - C_P$ values and resulting $\lambda - C_P$ curves.	87
Figure 6.19: Variation of λ with respect to time (a) and unsteady C_P for the blade 1 (b) and cumulative C_P with respect to azimuth angle (c) at three revolutions with different λ values at transient-state.	88
Figure 6.20: Variation of $\alpha_{geometric}$ (a), α_{local} (b) and C_P per blade (c) and the variation of cumulative C_P (d) with azimuth angle for one revolution at steady-state.	90
Figure 6.21: Variation of C_P with α_{local} for the blade 1 at three revolutions with different λ values at transient-state.	91

Figure 6.22: Large wind gust profile (a); dynamic responses of the load coefficient (b), rotor velocity (c), generator power (d), and wind torque (e) for CFD and simple dynamic simulations.	93
Figure 6.23: Amplitude of C_P oscillations in quasi-steady regime of CFD simulations for steady wind.	94
Figure 6.24: Large wind gust profile (a); dynamic responses of the load coefficient (b), rotor velocity (c), generator power (d), and wind torque (e) for the CFD simulation and the simple dynamic simulation with C_P oscillations.	95
Figure 6.25: Step wind profile (a); dynamic responses of the load coefficient (b), rotor velocity (c), and generator power (d) for the MPPT and SNC algorithms for simple dynamic simulations.	97
Figure 6.26: Step wind profile (a); dynamic responses of the load coefficient (b), generator torque (c), rotor velocity (d), and generator power (e) for the MPC and the SNC for simple dynamic simulations.	99
Figure 6.27: Wind gust profile (a); dynamic responses of the load coefficient (b), rotor velocity (c), and generator power (d) for the MPPT and SNC algorithms for simple dynamic simulations.	101
Figure 6.28: Wind gust profile (a); dynamic responses of the load coefficient (b), generator torque (c), rotor velocity (d), and generator power (e) for the MPC and the SNC for simple dynamic simulations.	102
Figure 6.29: Real wind profile (a); dynamic responses of the load coefficient (b), rotor velocity (c), and generator power (d) for the MPPT and SNC algorithms for simple dynamic simulations.	103
Figure 6.30: Real wind profile (a); dynamic responses of the load coefficient (b), generator torque (c), rotor velocity (d), and generator power (e) for the MPC and the SNC for simple dynamic simulations.	104
Figure 6.31: Mechanical power produced by the rotor, P_{wind} , and electrical power produced by the complete system, P_{gen} , vs the rotor velocity for $U = 6$ m/s.	107
Figure 6.32: $V_L/U - C_{Pgen}$ curves for a range of steady wind velocities.	108

Figure 6.33: Step wind profile (a); dynamic responses of the load coefficient (b), rotor velocity (c), and generator power (d) for the MPPT and SNC algorithms for electromechanical simulations.....	110
Figure 6.34: Step wind profile (a); dynamic responses of the load coefficient (b), rotor velocity (c), and generator power (d) for the MPC and SNC for electromechanical simulations.....	111
Figure 6.35: Wind gust profile (a); dynamic responses of the load coefficient (b), rotor velocity (c), and generator power (d) for the MPPT and SNC algorithms for electromechanical simulations.....	112
Figure 6.36: Wind gust profile (a); dynamic responses of the load coefficient (b), rotor velocity (c), and generator power (d) for the MPC and the SNC for electromechanical simulations.....	113
Figure 6.37: Real wind profile (a); dynamic responses of the load coefficient (b), rotor velocity (c), and generator power (d) for the MPPT and SNC algorithms for electromechanical simulations.....	114
Figure 6.38: Real wind profile (a); dynamic responses of the load coefficient (b), rotor velocity (c), and generator power (d) for the MPC and SNC for electromechanical simulations.....	115
Figure 6.39: Step wind profile (a); dynamic responses of the load coefficient (b), rotor velocity (c), and generator power (d) for HIL simulations.....	118
Figure 6.40: Wind gust profile (a); dynamic responses of the load coefficient (b), rotor velocity (c), and generator power (d) for HIL simulations.....	119
Figure 6.41: Real wind profile (a); dynamic responses of the load coefficient (b), rotor velocity (c), and generator power (d) for HIL simulations.....	120
Figure 6.42: Step wind profile (a); dynamic responses of the load coefficient (b), rotor velocity (c), and generator power (d) for electromechanical simulations with noise.....	124
Figure 6.43: Wind gust profile (a); dynamic responses of the load coefficient (b), rotor velocity (c), and generator power (d) for electromechanical simulations with noise.....	125
Figure 6.44: Real wind profile (a); dynamic responses of the load coefficient (b), rotor velocity (c), and generator power (d) for electromechanical simulations with noise.....	126

Figure 6.45: Responses of the SNC for different values of the inertia, J , in the presence of C_P oscillations.	128
Figure 6.46: Responses of the SNC for different values of the inertia, J , for sinusoidal wind profile.	130

LIST OF TABLES

Table 3.1: Properties of the rotor and the blades used in simulations.	16
Table 3.2: CFD model convergence	22
Table 4.1: Results of the parametric study for the tuning of fixed step-size.	38
Table 4.2: Results of the parametric study for the tuning of variable-step gain.....	38
Table 4.3: Energy efficiency results of the parametric study for the tuning of SNC.	44
Table 5.1: Electromechanical model parameters	51
Table 5.2: Energy efficiency results of the parametric study for the tuning of SNC for HIL and electromechanical simulations.	63
Table 6.1: Mid-range values of the tip-speed ratio and the power coefficient for different values of the load coefficient for $U = 6$ m/s.	69
Table 6.2: Energy efficiency results for simple dynamic simulations.....	105
Table 6.3: Energy efficiency results for electromechanical simulations.....	116
Table 6.4: Energy efficiency results for HIL simulations.	122
Table 6.5: Energy efficiency results for electromechanical simulations with noise.	127

NOMENCLATURE

Acronym	Description
WPP	Wind power plant
WECS	Wind energy conversion system
VAWT	Vertical axis wind turbine
HAWT	Horizontal axis wind turbine
CFD	Computational fluid dynamics
HIL	Hardware-in-the-loop
MPPT	Maximum power point tracking
MPC	Model predictive control
SNC	Simple nonlinear control
PIV	Particle image velocimetry
URANS	Unsteady Reynolds-averaged Navier-Stokes
LES	Large eddy simulation
P	Proportional
PI	Proportional-integral
PID	Proportional-integral-derivative
PV	Photovoltaic
HCS	Hill-climb searching
PMSG	Permanent magnet synchronous generator
EMF	Electromotive force
BDF	Backward differentiation
IEC	International Electrotechnical Commission
MPP	Maximum power point
SQP	Sequential quadratic programming

Symbol	Description	Unit
t	time	s
U	Wind velocity	m/s
ω	Rotor angular velocity	rad/s
λ	Tip-speed ratio	-
C_P	Power coefficient	-
ρ	Air density	kg/m ³
L	Rotor height	m
R	Rotor radius	m
J	Moment of inertia of rotor	kg-m ²
P_{wind}	Mechanical power of rotor	W
T_{wind}	Torque of rotor	N-m
P_{gen}	Generator power	W
T_{gen}	Generator torque	N-m
T_f	Friction torque	N-m
σ_{ij}	Stress tensor	N/m ²
n_j	Surface normal	-
S	Blade surface	m ²
V_L	Load voltage	V
I_L	Load current	A
R_L	Load resistance	Ω
K_b	Back electromotive force constant	V-s/rad
K_t	Torque constant	N-m/A
K_L	Load coefficient	-
η_{gen}	Generator efficiency	-
μ	Dynamic viscosity	Pa-s
c	Blade airfoil chord length	m
r_c	Blade airfoil camber radius	m
N_b	Number of blades	-
σ	Solidity	-
β	Fixed pitch angle of blades	$^\circ$
k	Turbulent kinetic energy	m ² /s ²
ε	Turbulent dissipation rate	m ² /s ³
μ_t	Turbulent viscosity	Pa-s
\mathbf{u}	Velocity field	m/s
y^+	Dimensionless wall distance	-
τ	Time constant	s
C_D	Drag coefficient	-
C_L	Lift coefficient	-
α	Angle of attack	$^\circ$
Re	Reynolds number	-
C_f	Friction coefficient	-
ω_0	Initial rotor angular velocity	rad/s

Symbol	Description	Unit
η_E	Energy efficiency	-
E_{gen}	Actual energy output	J
E_{ref}	Reference energy output	J
U_0	Free-stream velocity	m/s
u_e	Gust amplitude	m/s
t_0	Gust starting time	s
T_g	Gust period	s
K_f	Fixed step-size	-
K_v	Variable step-size gain	-
T_S	Control sampling period	s
N	Length of prediction horizon	-
M	Length of control horizon	-
Φ_E	Cost function for energy maximization	-
Φ_V	Cost function for voltage constraint	-
Φ_I	Cost function for current constraint	-
Φ	Composite cost function	-
w_1	Weight on energy maximization	-
w_2	Weight on satisfying constraints	-
e	Error	-
K_P	Proportional gain	-
ω_L	Lower limit for rotor velocity	rad/s
ω_U	Upper limit for rotor velocity	rad/s
γ	Normalized level of power coefficient	-
ω_m	Motor angular velocity	rad/s
E	Three-phase back EMF voltage	V
L	Inductance	mH
R	Resistance	Ω
φ_s	Flux of permanent magnets	V-s/rad
p	Number of pole pairs	-
V_{th}	Diode threshold voltage	V
R_{over}	Additional resistance term	Ω
S	Apparent power	W
Q	Reactive power	W
P_R	Real power	W
$P_{L,phases}$	Power loss on phases	W
$P_{L,rectifier}$	Power loss on rectifier	W
$V_{L,L}$	Lower limit for load voltage	V
$V_{L,U}$	Upper limit for load voltage	V
C_{Pgen}	Generator power coefficient	-
u	x-component of velocity field	m/s
v	y-component of velocity field	m/s
θ	Azimuth angle	$^\circ$

Symbol	Description	Unit
U_r	Net incident velocity vector	m/s
F	Force	N
F_{thrust}	Thrust force	N
C_{thrust}	Thrust coefficient	-
F_θ	Tangential force	N
F_R	Radial force	N
T	Torque	N-m
$C_{P,amplitude}$	Amplitude of power coefficient oscillations	-

Subscript	Description
i	i th component
j	j th component
k	k th component/step
x	x-direction
y	y-direction
max	Maximum
min	Minimum
opt	Optimum
ref	Reference
LN	Line-to-neutral
S	Stator phase
dc	Direct current equivalent
local	From local velocity field
geometric	From geometric approach
blade k	For k th blade

Chapter 1

INTRODUCTION

Wind energy has become the fastest growing segment of all renewable energy sources as a sustainable alternative to fossil fuels that can irreparably harm the environment [1-5]. Furthermore, wind power plants (WPPs) are not only environmentally-friendly owing to their low CO₂ emissions and safe operation, but also have a growing economic advantage because of numerous incentives such as low operation, maintenance, decommissioning, and land costs compared to the other energy sources like fossil fuels and nuclear plants [6]. Moreover, wind energy on Earth is abundant with an estimated continuous potential of around 10 million MW [2].

Majority of modern wind energy conversion systems (WECSs), i.e., wind turbines, basically consist of a rotor with airfoil-shaped blades to capture the power of the wind and a generator that converts the mechanical energy of the rotor to electricity. Wind turbines can be categorized based on the axis of rotation as horizontal axis wind turbines (HAWTs) and vertical axis wind turbines (VAWTs). Although HAWTs were invented later than VAWTs, they received most attention during the 20th century and have evolved more than VAWTs [7, 8]. Predominant HAWTs have high energy conversion efficiency when the wind quality is high; hence, the majority of large-scale WPPs comprise of HAWTs. On the other hand, since that large-scale WPPs (i.e., a capacity of 1-3 MW per turbine) may cause adverse effects on the climatic conditions, distributed and small-scale (i.e., a capacity of 1.4-20 kW per turbine) wind power generation has recently become an attractive and promising option [9]. Omnidirectional VAWTs are advantageous in gusty, turbulent winds with rapidly changing direction such as surface winds; furthermore, VAWTs are slower and quieter than HAWTs owing to their lower rotation rates [10]. Thus, a small-scale VAWT is favorable in urban

areas, e.g., on top of a building, as well as in rural areas away from the integrated grid systems where it can be used as a portable generator [10-14].

The mechanical structure of a VAWT is comprised of a rotor consisting of airfoil-shaped blades and arms and a vertical shaft that connects the rotor to a generator. Prevalent VAWTs have three basic types: drag-based Savonius and lift-based Darrieus egg-beater and H rotor types, which are illustrated along with a conventional HAWT in Figure 1.1 [15,16]. Among small-scale applications, the most common type, also the type that is investigated in this thesis, is the straight-bladed Darrieus type owing to its simple structure, high efficiency, and low cost [17].

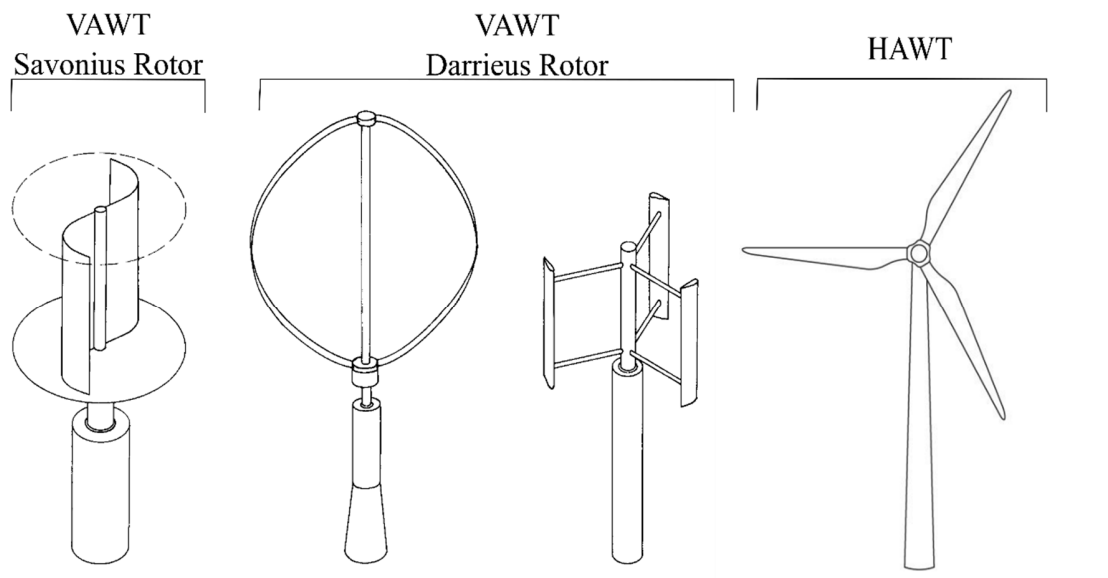


Figure 1.1: Rotor configurations for VAWT and HAWT [16].

1.1. Motivation & Objective

Recently, many countries, developed and developing, have set goals to replace a substantial amount of fossil fuel-based energy sources by renewable alternatives in the near future, and among renewable energy sources the wind energy is a very attractive option. Meanwhile, small-scale energy generation and smart grid applications have gained more significance as wind power potential over large geographic regions reaches saturation point with the increase of large-scale WPPs [18]. On the other hand, although there is an abundant literature regarding HAWTs, studies related to VAWTs are still limited. Thus, research into small-scale VAWTs is important.

This thesis aims to develop a framework to analyze the performance of a small-scale VAWT system that includes a three-straight-bladed rotor with high solidity, electromechanical and power electronics components and controller. For this purpose, first, the aerodynamic performance of the height-normalized rotor of a three-straight-bladed VAWT with high solidity is analyzed through a time-dependent, two-dimensional computational fluid dynamics (CFD) model that is coupled with the dynamics of the rotor subject the moment of inertia of the rotor and generator load. Second, the hardware-in-the-loop (HIL) simulation setup that is presented in [16,19] and consists of an electrical motor to emulate the VAWT rotor based on the aerodynamic performance obtained from CFD simulations, a gearbox, a generator, a rectifier, and a programmable electronic-load is employed to investigate the impact of electromechanical energy conversion on overall power characteristics. Third, two different adaptations of a maximum power point tracking (MPPT) algorithm with fixed and variable step-sizes, a model predictive control (MPC) for maximizing the energy output subject to the limitations of the electromechanical and power electronics components, and a simple nonlinear control (SNC) that mimics the MPC are designed and tested for step wind, wind gust, and real wind profiles.

In addition to the CFD and HIL simulations, a simple dynamic simulation that is the simplified version of the CFD simulation and an electromechanical simulation that is the simplified, software-only version of the HIL simulation are developed in order to design and test the controllers. The controllers are first designed and tested through simulations

assuming that the electromechanical energy conversion is ideal, i.e., the electromechanical and power electronics components are lossless; and then, they are redesigned by taking the effect of non-ideal electromechanical conversion into account and tested through electromechanical simulations. Lastly, the real-time performances of the controllers (excluding the MPC) are evaluated by carrying out HIL experiments.

1.2. Outline

The rest of the thesis is organized as follows:

- Chapter 2 presents a literature survey on modeling for VAWTs and control and HIL simulations of wind turbines as well as the contributions of this thesis.
- In Chapter 3, the rotor dynamics of a VAWT and the CFD model are described in detail.
- In Chapter 4, the simple dynamic model and the step wind, wind gust, and real wind profiles are introduced. Then, the MPPT, MPC and SNC algorithms are designed with a dynamics model under the assumption of an ideal electromechanical energy conversion.
- In Chapter 5, a brief description of the HIL simulation is given, the electromechanical simulation is explained, and the controllers are redesigned considering the influence of non-ideal electromechanical energy conversion.
- Chapter 6 presents CFD simulation results, control performances for simple dynamic, electromechanical, and HIL simulations for step wind, wind gust, and real wind profiles, and electromechanical simulation results regarding the effects of measurement noise, inertia, and power coefficient and wind oscillations on the performance.
- In Chapter 7, concluding remarks and directions for future research are given.

Chapter 2

BACKGROUND & CONTRIBUTIONS

2.1. Background

In 1970s, the researchers at Sandia National Laboratories carried out wind tunnel tests and compared with the field tests for a 2-meter diameter egg-beater-shaped Darrieus VAWT [20,21]. Based on the results from the experiment, a 34-meter diameter Darrieus VAWT test-bed was constructed to investigate aerodynamics, structural dynamics, fatigue life, and control designs in order to assess the feasibility of VAWTs during 1980s [22]. The results obtained in 1990s showed that compared to a two-bladed rotor, a three-bladed rotor has more structural stability, furthermore it eliminates in-plane and out-of-plane vibrational modes, moreover the torque output has less torque ripples as well; the efficiency of a small-scale H-rotor can be increased above 40%, and it is economically advantageous over egg-beater configuration since it requires shorter blades for a certain power level; thus, three-bladed and H-rotor configurations are promising for future designs.

Aerodynamic modeling is a useful approach to analyze and improve the design of VAWTs. [13,17, 23, 24] investigate and review the prevalent modeling methods for Darrieus VAWT which can be categorized as computational aerodynamics methods that involves momentum, vortex, and cascade models, computational fluid dynamics methods, and experimental methods. Obviously, the experimental methods, namely, wind tunnel tests and particle image velocimetry (PIV) methods provide the most accurate results; however, their use may be prohibitive due to high construction costs, and therefore they are usually used for the validation of other methods. Among the computational aerodynamic methods, the cascade model is found to be the most precise and least problematic method. On the other hand, CFD modeling offers the ability of detailed visualization of flow near airfoils in

addition to more accurate prediction of aerodynamic performance. CFD models can be classified based on their dimensions as 2D, 2.5D and 3D models. Despite the fact that higher dimensional models yield more precise results, high computational effort requirement restricts the use of them. Thus, 2D CFD models are currently the most popular approach in literature for modeling Darrieus VAWTs.

In addition to numerical optimization such as in [25] and experimental evaluation of VAWT airfoils, e.g., [26], CFD models have been commonly used for the analysis of the rotor performance. In [27], a 3D unsteady Reynolds-averaged Navier-Stokes (URANS) CFD model of a VAWT is developed, and parametric studies on the design are conducted; however, the computations are limited to single-bladed turbines without the consideration of trailing wakes. Wind tunnel tests and 2D and 3D URANS CFD simulations of a small-scale VAWT are carried out by Howell et al. [28], where two- and three-straight-bladed configurations are compared, and three-bladed configuration is found to be advantageous due to its peak power at lower tip-speed ratios. Authors also reported that the absence of tip vortices in 2D simulations causes an overestimation of the power coefficient if the blades are short [28] consistently with the results reported in [29] as well. In [30], 2D and 2.5D URANS, and 2.5D large eddy simulation (LES) CFD simulations of a three-straight-bladed VAWT are performed, and the results demonstrated that the discrepancy between 2D and 2.5D URANS simulations is not significant despite the fact that the 2.5D LES provides more accurate results; authors use 2.5D for periodic boundary conditions in the out-of-plane direction. Furthermore, [31] employs a 2D URANS model to investigate the effect of trailing edge shape on the performance of a straight-bladed VAWT.

VAWTs can operate and generate energy in turbulent and gusty wind conditions by the virtue of being omnidirectional and having a simple design. Recently, experimental and CFD techniques have been used to investigate the influence of unsteady wind conditions on VAWTs. Vorticity transport method is used to analyze the aerodynamics of three-bladed VAWTs with straight, curved and helically-twisted blades under sinusoidal wind conditions by Scheurich and Brown [32], and authors report that straight- and curved-bladed configurations suffer from greater performance losses than the helically-twisted ones during wind oscillations with large amplitude (e.g., $\Delta U/U_0 = \pm 0.3$), but the range of variations of the power coefficient remains unchanged for steady and sinusoidal winds with amplitude-to-

mean ratio of 0.1 and 0.3 for straight-bladed turbines. Kooiman and Tullis [33] report that transient fluctuations in the amplitude of the wind velocity in an urban environment deteriorates the performance of a high solidity ($\sigma \approx 1$) H-type VAWT, while the fluctuations in the wind direction do not have an effect. Similar observations on the effect of large fluctuations are reported elsewhere. According to [34-37], unsteady wind velocity deteriorates the performance of three-straight-bladed VAWTs especially for large fluctuations in the wind velocity: $\pm 30\%$ fluctuations in the wind speed lead to negative power coefficient values. According to 2D-RANS-CFD-based studies on the effects of the solidity and the thickness and camber of the blades on the aerodynamic performance of three-straight-bladed VAWTs under fluctuating wind conditions, cambered thick blades are desirable within unsteady wind environments [36,38] owing to higher torque generation.

In transient winds, the dynamics of the rotor plays an important role. Hara et al. [39] studied the effect of inertia in the energy efficiency of VAWTs under pulsating wind conditions with experiments and a blade-element momentum model, and concluded that the energy efficiency of the VAWT is not influenced by the oscillations in the wind velocity unless the period of oscillations is large and the moment of inertia is small; only then, the energy output varies depending on the power coefficient curve. In addition to the dynamics of the rotor, several CFD modeling studies for Darrieus VAWT address the effects of the control algorithm on the utilization of gusts and wind fluctuations. McIntosh et al. [40] show that unsteady winds and fluctuations can increase the energy output of the VAWT by demanding a higher tip-speed ratio above the steady optimum through the constant rotational speed controller. Moreover, unsteady analysis can be effective in the development of controller strategies for the extraction of energy in the wind fluctuations. In [41], authors report that a higher energy efficiency is achieved by means of increased torque due to accelerating free stream and blade stall. In other words, wind transients such as gusts and fluctuations can be exploited by a small-scale VAWT, if it is controlled accordingly; thus, the control design is very crucial for such a system.

Although constant-speed wind turbines can be connected directly to the utility grid, i.e., without a power electronics medium, the minority of modern wind turbines operate in constant-speed mode; instead, variable-speed operation is preferred owing to its higher efficiency [42,43]. For large-scale variable-speed wind turbines, there are three main regions

of operation based on the wind velocity. Region 1 is the start-up region, in which the wind velocity is below a cut-in rate; whereas, region 3, in which the wind velocity is above the rated and below a cut-off wind velocity, is a constant-power mode aiming to ensure the safe operation of mechanical and electrical components, and above the cut-off wind speed the turbine does not operate. In region 2, namely between the cut-in and rated wind velocities, the goal is to extract the maximum energy from the wind. Generally, the goal of control for large-scale wind turbines is a combination of multi-objectives such as maximization of energy, reduction of mechanical loads on tower and blades, and smoothing of power gradients, and the control variables are generator torque, blade pitch angle, and yaw angle. For limiting power and rotor velocity in region 3, usually conventional control techniques such as proportional-integral-derivative (PID) control are used for pitch angle control; while generator torque control is usually used for tracking the optimal power in region 2 [43]. On the other hand, small-scale VAWTs may avoid such mechanical limitations such as blade bending and capture the energy from extreme winds; hence, they basically operate solely in region 2 with an objective of energy maximization subject to electrical system limitations through generator torque control.

Maximum power point tracking is a popular control method for varying unsteady effects in the energy supply such as photovoltaic (PV) devices and wind energy conversion systems [6]. In case of WECSs, basically, there is an optimal tip-speed ratio for each turbine that yields the maximum power which is aimed to be tracked by MPPT algorithms. There are numerous studies regarding MPPT in literature such as [44-48]. Abdullah et al. [49] review and discuss MPPT control techniques for HAWTs and classifies them mainly into four categories: tip-speed ratio control, optimal torque control, power signal feedback control, and hill-climb searching (HCS) (or perturbation and observation) control. Among these, HCS method is the only one that requires neither turbine model nor wind speed measurement. Since accurate modeling and wind speed measurement would be challenging and costly for a small-scale system [16], HCS method would be favorable despite the fact that tip-speed ratio control and optimal control are found to perform slightly better under varying wind conditions. Koutroulis and Kalaitzakis [44] propose a generic HCS MPPT technique to maximize the power output of wind energy conversion with 10-50% increase in the power output compared to a generator directly connected to a battery bank via a rectifier. The

adaptive HCS MPPT algorithm proposed by Kazmi et al. [47] detects and updates the speed – power characteristics of the turbine throughout operation and uses this information to adapt the size of control steps; results show that the adaptive method outperforms conventional HCS MPPT.

Model predictive control is an advanced control technique for systems that can be modeled accurately. Moreover, MPC is an optimal control approach since it optimizes the control trajectory over a prediction horizon in a receding horizon procedure. Thus, a model predictive controller that exploits wind speed predictions (e.g., using LIDAR) to maximize the energy generation subject to electrical system constraints could provide the optimal control strategy for arbitrary wind conditions. Furthermore, for large-scale HAWTs, MPC has been proven to perform satisfactorily for maximizing energy efficiency [50] in addition to load reduction [51-53] or improving power quality [54,55] as well as for handling additional constraints [56,57]. However, use of MPC is not common for small-scale VAWTs which have different operating characteristics from HAWTs.

The cost of a prediction system and computational power requirements may be restrictive to use such an advanced technique for small-scale applications. Additionally, inevitable uncertainties in the wind speed should be considered while designing an MPC for WECSs. Nonetheless, the response of MPC to arbitrary wind conditions may provide an insight into optimal control strategies for particular wind patterns which can be used to design a simple MPC-mimicking control.

Aerodynamic modeling is an effective approach to predict power coefficient and evaluate the performance of a VAWT rotor. On the other hand, a VAWT system comprises of not only a rotor but also electromechanical and power electronics components which also affect the power characteristics significantly while converting the mechanical energy into electricity. Hardware-in-the-loop simulations have numerous advantages over numerical-only simulations in testing the performance of actual components and control designs in controlled experiments under realistic conditions [58]. The effects of operating characteristics of hardware components, real-time implementation of control algorithms, measurement noise, thermal effects and other disturbances are directly observed in HIL simulations [59]. For WECSs, HIL simulations are employed to test the performance of

electromechanical and power electronics components and controller under arbitrary wind conditions [16, 60-65]. In order to ensure the fidelity of the simulator, the static and dynamic characteristics of the HIL simulator must be the same as the characteristics of the real system [62].

2.2. Contributions

The major contributions of this thesis can be summarized as follows:

- Development of a time-dependent, two-dimensional CFD model coupled with the dynamics of the rotor for a small-scale, height-normalized, three-straight-bladed VAWT with high solidity to analyze tip-speed ratio – power coefficient relationship for steady and unsteady wind conditions and to observe the transient performance of VAWT systems including the inertial effects of the rotor and the feedback control;
- Investigation of the impact of electromechanical energy conversion, power electronics components, and real-time control on overall performance through HIL experiments;
- Development of an MPC approach to obtain the optimal control strategy for maximization of energy generation subject to electrical limitations;
- Development of a surrogate for MPC design, which is called simple nonlinear control, to eliminate the drawbacks of MPC; and
- Development of model-free and wind speed sensorless fixed-step and variable-step MPPT algorithms.

In CFD modeling studies in literature a fixed rotor velocity is prescribed. In this thesis, however, a coupled rotor dynamics and 2D CFD modeling approach for a three-straight-bladed VAWT that allows variable rotor speed is developed and analyzed from a mechatronics perspective. The model is validated with data from an experimental VAWT that has the same dimensions with the rotor in the model, and only subject to friction torque, which is estimated by coast-down experiments at zero wind conditions. Long-time behavior of the VAWT rotor that is coupled with feedback control and inertia, which corresponds to

hundreds of revolutions of the rotor (*ca* 75 – 100 seconds), are simulated for detailed analysis of quasi-steady and instantaneous power coefficients in steady and unsteady winds with standardized gusts and to understand the relationship between steady and unsteady power coefficient characteristics. Additionally, simulations are performed to obtain the relationship between the power coefficient and the tip-speed ratio, to investigate the flow physics, and to demonstrate the performance of the controller. A detailed analysis of the unsteady angle of attack and power coefficient is carried out. Results show that the proposed coupled modeling approach is an effective tool for system-level design and performance evaluation of VAWT systems under wind transients.

Since CFD simulations require excessive amount of computation times, a simple dynamic simulation is developed using the tip-speed ratio – power coefficient characteristics obtained from CFD simulations. A comparison between the results of the CFD model and the simple model shows that the simple model is sufficiently accurate to evaluate the performance of the VAWT system including the controller from a dynamic performance point of view. Thus, the simple dynamic model is used to design, implement and compare control methods for arbitrary wind conditions. First, model-free, wind speed sensorless fixed- and variable-step HCS MPPT algorithms are developed. Second, a model predictive control is designed for maximization of energy generation subject to electrical limitations of the system. Third, a simple nonlinear MPC-mimicking control is proposed based on the behavior of the MPC for step wind. Lastly, a comparison of these methods for step wind, wind gust and real wind profiles is carried out. It is shown that maximizing the instantaneous power does not mean maximizing the energy generation, and the energy output can be enhanced by allowing deviations from the maximum power instantaneously for future gains in energy generation. Moreover, the SNC demonstrates a successful performance in the sense of mimicking the MPC.

In order to investigate the influence of electromechanical energy conversion on the power characteristics of the VAWT system, we employ the HIL test-bed developed in [16,19], in which an electrical motor emulates the VAWT rotor based on a power coefficient curve obtained from CFD simulations. The power curve from the CFD model is used in a software-only electromechanical simulation environment, which is the simplified DC equivalent of the HIL test-bed. According to simulation results, the generator and power

electronics components have a profound effect on the overall power output and efficiency of the VAWT system and the performance of a controller is influenced by real-time noise and measurement errors. Hence, the electromechanical simulation is used to redesign the fixed- and variable-step MPPT, SNC, and MPC algorithms accordingly. Electromechanical and HIL simulations are carried out to test the performance of the controllers for step wind, wind gust, and real wind inputs. According to results, the controllers perform satisfactorily for all of the step wind, wind gust, and real wind inputs in both simulations, and the experimental results for the MPPT and SNC algorithms are similar to the electromechanical simulation results which means that the electromechanical simulation is a reliable tool to design and evaluate control algorithms for actual VAWT systems.

Chapter 3

MODELING

3.1. Rotor dynamics

Basically, a VAWT consists of a rotor and a generator that are connected through a vertical shaft. The rotor comprises of blades and blade arms to convert wind power into mechanical power, while the generator produces electricity from the mechanical power. Thus, the rate of change of the angular velocity of the rotor, ω , is obtained from the conservation of the angular momentum by dividing the net torque on the shaft by the moment of inertia, J , as follows:

$$\frac{d\omega}{dt} = \frac{T_{wind} - T_{gen} - T_f}{J} \quad (3.1)$$

where T_{wind} is the wind torque that is generated by the blades, T_{gen} is the generator torque, T_f is the friction torque which is proportional to the rotor velocity with a friction coefficient.

The mechanical power of the rotor of a Darrieus VAWT, P_{wind} , is defined as:

$$P_{wind} = C_p(\lambda, t)\rho LRU^3 \quad (3.2)$$

where U is the wind velocity, ρ is the air density, R is the rotor radius, L is the rotor height, $C_p(\lambda, t)$ is the power coefficient, and λ is the tip-speed ratio given by:

$$\lambda = \frac{\omega R}{U} \quad (3.3)$$

Thus, if the tip-speed ratio – power coefficient relation of the rotor is known, T_{wind} can be obtained by dividing the mechanical power of the rotor by the rotor velocity, as below:

$$T_{wind} = \frac{P_{wind}}{\omega} = \frac{C_p(\lambda, t)\rho LRU^3}{\omega} \quad (3.4)$$

Alternatively, T_{wind} can be calculated from the total fluid stress at the surface of the blade in the CFD model:

$$T_{wind} = \sum_{k=1}^3 \int_{S_k} [(x-x_0)\sigma_{yj} - (y-y_0)\sigma_{xj}] n_j(x, y) dS \quad (3.5)$$

where σ_{ij} are the components of the stress tensor, j indicates x or y direction, $n_j(x, y)$ is the j^{th} component of the surface normal at a given position, (x, y) , on the blade, x_0 and y_0 are the position of the shaft, and S_k is the surface of the k^{th} blade.

The generator torque, T_{gen} , is adjusted by a control algorithm in terms of either a load coefficient (e.g., for CFD and simple dynamic simulations) or the load current (e.g., for HIL simulations). Hence, T_{gen} is defined in terms of both the load coefficient and the load current here.

Within the VAWT system, a direct-drive permanent magnet synchronous generator (PMSG) is used for mechanical to electrical energy conversion, which is usually preferred for such systems owing to its advantages such as high efficiency, reliability, gearless construction, lightweight, and self-excitation [49,66]. Since the electrical dynamics is much faster than the mechanical dynamics, its effect on the transient response can be omitted.

For an ideal PMSG, the load voltage, V_L , is given by the product of the back electromotive force (EMF) constant, K_b , and the rotor velocity:

$$V_L = K_b \omega \quad (3.6)$$

Similarly, the generator torque is the product of the load current, I_L , and a factor, K_t , which is the torque constant, as follows:

$$T_{gen} = K_t I_L \quad (3.7)$$

In this case, it is assumed that the generator is connected to a pure-resistive load by means of a controller which manipulates the resistance of the load. Thus, Ohm's law prevails between the load voltage and the load current, I_L , in terms of the load resistance, R_L :

$$I_L = V_L / R_L \quad (3.8)$$

Hence, the generator power, P_{gen} , namely the power output can be written as:

$$P_{gen} = \eta_{gen} \frac{V_L^2}{R_L} = \eta_{gen} \frac{K_b^2}{R_L} \omega^2 \quad (3.9)$$

where η_{gen} is the efficiency of the generator and although it depends on the operating voltage and current and affects the power output significantly, here the efficiency of the generator is assumed 100% for the sake of simplicity. As a result, T_{gen} and P_{gen} can be rewritten in terms of a load coefficient, i.e., $K_L = K_b^2/R_L$, as follows:

$$T_{gen} = K_L \omega \quad (3.10)$$

$$P_{gen} = K_L \omega^2 \quad (3.11)$$

3.2. Computational Fluid Dynamics Model

In order to calculate the wind torque given by (3.5), instantaneous stresses over the surfaces of the blades must be known. Here, a time-dependent, 2D CFD model of a height-normalized, three-straight-bladed, small-scale VAWT is developed using COMSOL Multiphysics software [67] to obtain the flow around the rotor and the stresses on the blades. Since the k- ϵ turbulence model is very common, sufficiently accurate, stable and relatively cost-effective compared to other turbulence models, it is adopted here for the CFD model coupled with the dynamics of the rotor to obtain a long time behavior of the rotor coupled with feedback control and inertia.

3.2.1. Geometry and Computational Domain

The VAWT modeled here has three straight blades with a height, L , of 1 m, and the rotor radius, R , is 0.5 m. The blade profile is a cambered NACA0020 airfoil with a chord length, c , of 0.35 m corresponding to a solidity (i.e., $\sigma = N_b c/R$) of 2.1. The chord of the modified blade is arched with a camber radius, r_c , slightly larger than the rotor radius, which is set to 0.6 m here, as shown in Figure 3.1; the thickness, δ , is kept the same as the reference symmetric blade. The properties of the rotor and the blades used in simulations are summarized in Table 3.1.

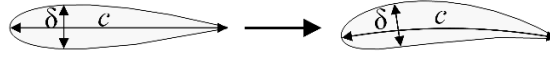


Figure 3.1: Morphing process of a cambered NACA0020 airfoil profile.

Table 3.1: Properties of the rotor and the blades used in simulations.

Parameter	Symbol	Value	Unit
Air density	ρ	1.205	kg/m ³
Dynamic viscosity	μ	1.82×10^{-5}	Pa-s
Number of blades	N_b	3	-
Rotor radius	R	0.5	m
Rotor height	L	1	m
Rotor moment of inertia	J	1.5	kg-m ²
Blade airfoil chord length	c	0.35	m
Blade airfoil camber radius	r_c	0.6	m
Solidity	σ	2.1	-
Fixed pitch angle of blades	β	5	°
Torque constant	K_t	1.4877	N-m/A
Back EMF constant	K_b	1.4877	V-s/rad

The computational domain consists of a stationary rectangle and a circular region that rotates with the rotor, as shown in Figure 3.2. No-slip boundary condition is imposed at the surfaces of the blades that rotate with the domain. The angular velocity of the rotor, which is an unknown and calculated from the equation of motion for the rotor given in (3.1). The top and bottom boundaries are walls with slip boundary conditions, for which there is no flow normal to the surface and the shear parallel to the surface is set to zero. The left boundary is a uniform velocity inlet, and the right boundary is a normal-stress-free outlet.

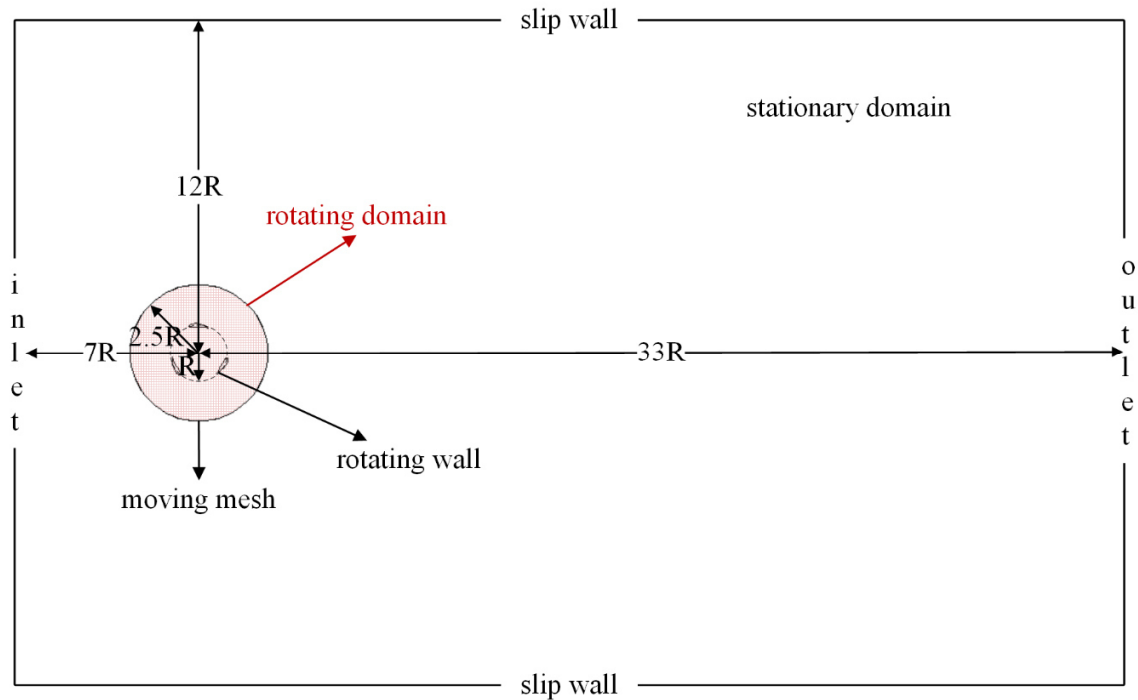


Figure 3.2: Geometry of the domain and boundary conditions in the CFD model.

3.2.2. k - ϵ Turbulence Model

In order to obtain the flow around the rotor and the stresses on the blades, the k - ϵ turbulence model is used in this study since it is sufficiently accurate, stable and relatively cost-effective compared to other turbulence models. For this purpose, the Turbulent Flow, k - ϵ interface of COMSOL Multiphysics is employed which solves the unsteady Reynolds-averaged Navier-Stokes equations for conservation of momentum and the continuity equation for conservation of mass [68].

The k - ϵ model uses the standard k - ϵ equations, the turbulent kinetic energy, k , and the turbulent dissipation rate, ϵ , [69] subject to realizability constraints, and wall functions are used to model the flow near walls.

The turbulent viscosity, μ_T , is defined as:

$$\mu_T = \rho C_\mu \frac{k^2}{\varepsilon} \quad (3.12)$$

where $C_\mu = 0.09$.

The transport equation for the scalar field k is given by:

$$\rho \frac{\partial k}{\partial t} + \rho \mathbf{u} \cdot \nabla k = \nabla \cdot \left[\left(\mu + \frac{\mu_T}{\sigma_k} \right) \nabla k \right] + P_k - \rho \varepsilon \quad (3.13)$$

where \mathbf{u} is the velocity field, μ is the dynamic viscosity, $\sigma_k = 1.3$, and P_k is the production term given by:

$$P_k = \mu_T \left[\nabla \mathbf{u} : (\nabla \mathbf{u} + (\nabla \mathbf{u})^T) - \frac{2}{3} (\nabla \cdot \mathbf{u})^2 \right] - \frac{2}{3} \rho k \nabla \cdot \mathbf{u} \quad (3.14)$$

The transport equation for the turbulent dissipation, ε , is expressed as:

$$\rho \frac{\partial \varepsilon}{\partial t} + \rho \mathbf{u} \cdot \nabla \varepsilon = \nabla \cdot \left[\left(\mu + \frac{\mu_T}{\sigma_\varepsilon} \right) \nabla \varepsilon \right] + C_{\varepsilon 1} \frac{\varepsilon}{k} P_k - C_{\varepsilon 2} \rho \frac{\varepsilon^2}{k} \quad (3.15)$$

where $\sigma_\varepsilon = 1.3$, $C_{\varepsilon 1} = 1.44$, and $C_{\varepsilon 2} = 1.92$.

3.2.3. Time-dependent solver

The time-dependent solver employs a variable-step backward differentiation formula (BDF) method with a maximum order of 5 for integrating the URANS, k- ε equations and the constraint equation for the rotor dynamics given by (3.1) to compute the rotor velocity for the specified load coefficient, from which the generator torque is calculated. A detailed description of this method can be found in [70].

3.2.4. Domain Size

The size of the computational domain that includes a rotating domain around the rotor and the surrounding fluid (Figure 3.2) is varied to obtain the torque-free angular velocity of the rotor in a number of simulations when the wind velocity, U , is 6 m/s. The most economic size of the computational domain and the radius of the rotating domain are found as $40R \times 24R$ and $2.5R$ respectively, as shown in Figure 3.2. This structure is consistent with the others in literature, e.g., [29] and [31]. According to simulations presence of the shaft at the rotor center does not have a significant impact on the flow distribution and on the rotor velocity.

3.2.5. Mesh

The flow field is obtained from the solution of the URANS equations with the finite-element method that contains first-order triangular elements except the boundary layers enclosing the blades where quadrilateral elements are used. Since the external boundaries of the blades in this model are rotating walls for which the corresponding conditions regarding the rotation of the wall are prescribed, the blades are enclosed with boundary layers with a dimensionless wall distance y^+ of 10, namely starting from outside of the viscous layer, where the inner layers are approximated by wall functions [68]. The quality of the finite-element mesh is adjusted by conducting a mesh convergence study in which the mesh quality is varied gradually. As a result, the mesh configuration that is shown in Figure 3.3 is found satisfactory. The complete mesh consists of 58104 triangular and 3180 quadrilateral domain elements, 1044 boundary elements, and 21 vertex elements, and the model is solved for 163762 degrees of freedom. If the element quality is defined as the ratio of the inscribed and circumscribed circles' radii for the simplex corresponding to each corner of the element, the minimum element quality is 2.08% while the average element quality is 92.29% for this mesh.

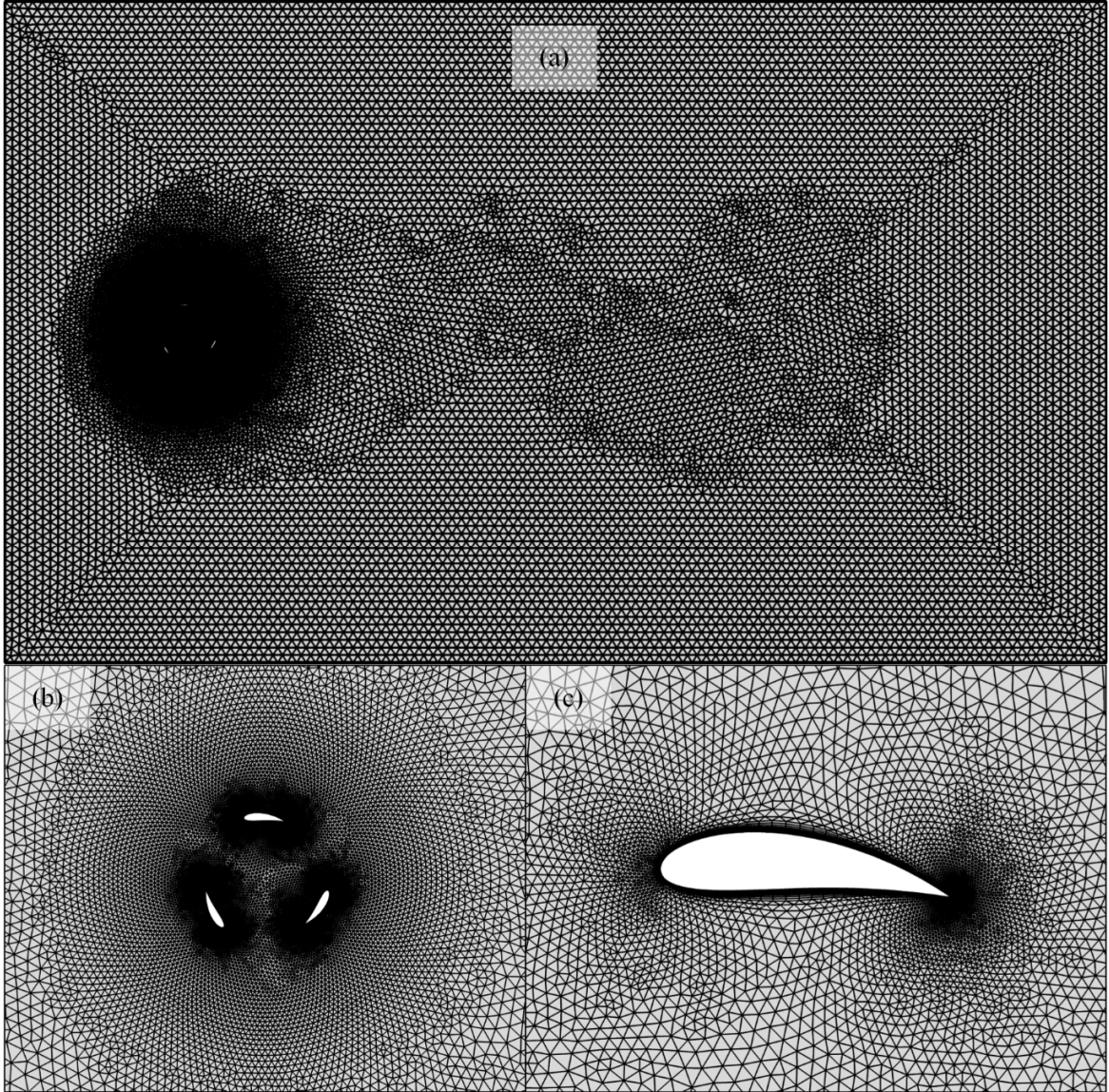


Figure 3.3: Mesh configurations for (a) whole domain, (b) rotor, and (c) the blade.

3.2.6. Convergence Studies

Figure 3.4 shows the angular velocity of the torque-free rotor (i.e., $T_{gen} = 0$ N-m and $T_f = 0$ N-m) as a function of time for a wind velocity of 6 m/s for various mesh and domain sizes and with and without the shaft at the center of the rotor. In the legend, the domain size is expressed in terms of the relative area of the domain with respect to the optimal size (i.e., $40R \times 24R$); only one simulation is performed with the shaft at the center; for three simulations, the mesh involved boundary layers around the blades with $y^+ \approx 10$, which is close to the limit for the wall functions, 11.06 [68]. Lastly, for all of the cases, the number of degrees of freedom representing the mesh size is denoted in parenthesis. Table 3.2 summarizes the degrees of freedom that the model is solved for, the resultant computational times for 75-second simulations and the final quasi-steady-state rotor velocities for the simulations compared in Figure 3.4 which also yield the following observations.

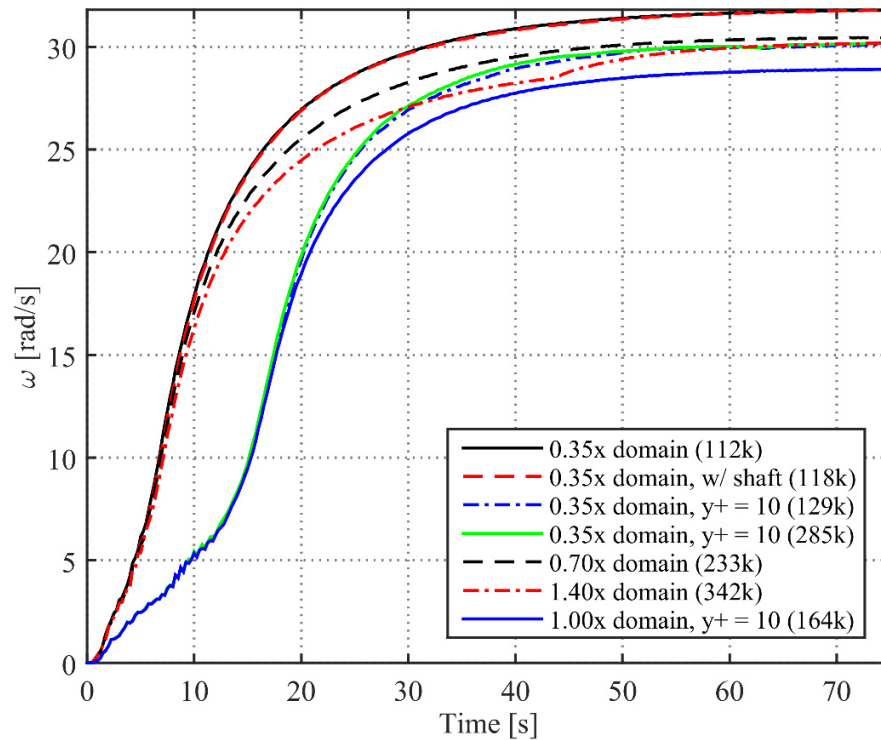


Figure 3.4: Angular velocity transients of the torque-free rotor for different finite-element mesh and domain sizes for $U = 6$ m/s.

Table 3.2: CFD model convergence

Model	Degrees of freedom	Computational time [s]	Final quasi-steady-state rotor velocity [rad/s]
0.35x domain	112k	185611	31.8
0.35x domain, w/ shaft	118k	197877	31.8
0.35x domain, $y^+ = 10$	129k	1036594	30.1
0.35x domain, $y^+ = 10$	285k	1931754	30.2
0.70x domain	233k	348058	30.4
1.40x domain	342k	868295	30.2
1.00x domain, $y^+ = 10$	164k	1357220	28.9

First, in all cases, the rotor self-starts successfully from rest, due to the large solidity of the rotor, i.e., $\sigma = 2.1$, and the angular velocity seemingly reaches to a quasi-steady-state. Even though neither the turbulent flow in the domain nor the rotor velocity is actually in steady-state, the variation of the angular velocity with respect to time is very small; thus, we call this final state quasi-steady-state, as commonly called in literature as well. Convergence to the quasi-steady-state depends on the time constant of the rotor, τ , which can be expressed as the ratio of the moment of inertia to the slope of the wind torque with respect to the angular velocity from (3.1), as follows:

$$\tau \approx \frac{J}{|\partial T_{wind} / \partial \omega|} \quad (3.16)$$

As the rotor accelerates from rest, time constant varies due to the dependence of the wind torque on the angular velocity. At the maximum power, this time constant is estimated to be around 11 seconds, and at the maximum angular velocity, where the wind torque is zero, the time constant is about 16 seconds. On the other hand, the unsteady behavior of the power coefficient is truly interesting and discussed in Chapter 6.

Second, the quasi-steady-state rotor velocities are within 10% for all mesh configurations and domains studied here. Highest velocity, about 31.8 rad/s, is obtained for the reduced domain with and without the shaft, which has no effect on the final state. As the domain size increases or a fine boundary layer mesh is used around the blades, the final velocity decreases to 30.2 rad/s. For the standard domain size and the fine mesh around the blades, as indicated by “1.00x domain, $y^+ = 10$ (164k)” the final velocity is about 28.9 rad/s. Increasing quality of the mesh and larger computational domain increase the computation

time for the simulation of one-minute up to 15 days on an Intel-based Linux server with 48 cores of Intel Xeon E5-2697 operating at 2.70 GHz; whereas, the same run takes about 2 days for the coarsest mesh and the smallest domain size. Hence, the low resolution configuration, indicated by “0.35x domain, w/o shaft (112k)”, is used to obtain the power-coefficient curves for different steady wind velocities, and the high resolution configuration, indicated by “1.00x domain, $y^+ = 10$ (164k)”, is used for the transient performance analysis for wind gusts.

3.2.7. Validation

3.2.7.1. Validation of the k- ϵ Turbulence Model

The k- ϵ turbulence model is preferred in this study because it is sufficiently accurate, stable and relatively cost-effective compared to other models. Nonetheless, its accuracy needs to be assessed to assure that the CFD model provides reliable results. For this purpose, the computational domain is resized preserving the mesh quality, and the rotor is replaced by a symmetric NACA0021 airfoil with a chord length of 0.35 m, as shown in Figure 3.5; in this model, the angle of attack is changed by rotating the rotating domain. Then, four-second simulations are run to obtain the drag and lift coefficients (C_D and C_L) for a range of angle of attack (α) values for $U = 15.54$ m/s, which corresponds to a Reynolds number (Re) of 360000, and the results are compared to the experimental data that is obtained from wind tunnel tests for a NACA0021 airfoil and $Re = 360000$ and presented in [20]. For simulations, C_L and C_D values are calculated from:

$$C_D = \frac{\oint \sigma_{xj} n_j dS}{\frac{1}{2} \rho U^2 c} \quad (3.17)$$

$$C_L = \frac{\oint \sigma_{yj} n_j dS}{\frac{1}{2} \rho U^2 c} \quad (3.18)$$

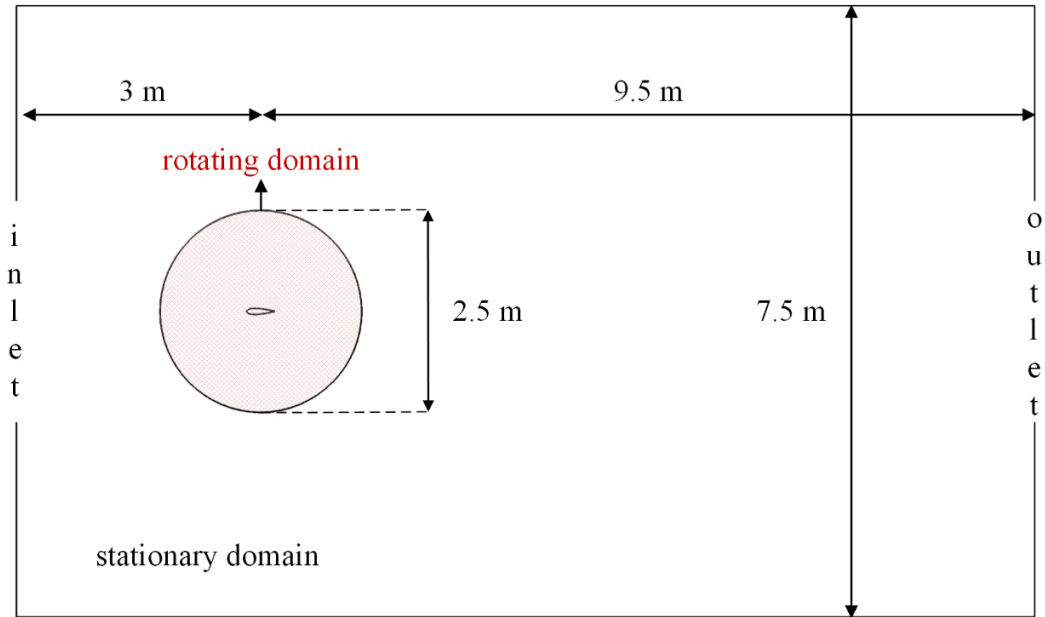


Figure 3.5: CFD model for validation of the $k-\epsilon$ turbulence model.

The resulting C_L and C_D values vs the angle of attack are depicted in Figure 3.6. According to Figure 3.6a, the $k-\epsilon$ model estimates the C_D with an acceptable accuracy for angle of attack values less than 55° , for greater angle of attack values, however, it overestimates the drag with a relative error of about 45%. On the other hand, Figure 3.6b shows that the lift coefficient predicted by the $k-\epsilon$ model overshoots around $\alpha = 15^\circ$, diverges from the experimental results for $30^\circ < \alpha < 60^\circ$, and converges to the experimental results for $\alpha > 60^\circ$. Nonetheless, the $k-\epsilon$ turbulence model predicts the drag and lift coefficients with average absolute errors of 30.8% and 25.7%, respectively. Thus, the $k-\epsilon$ turbulence model can be deemed satisfactory for analysis of the dynamic performance of the VAWT rotor.

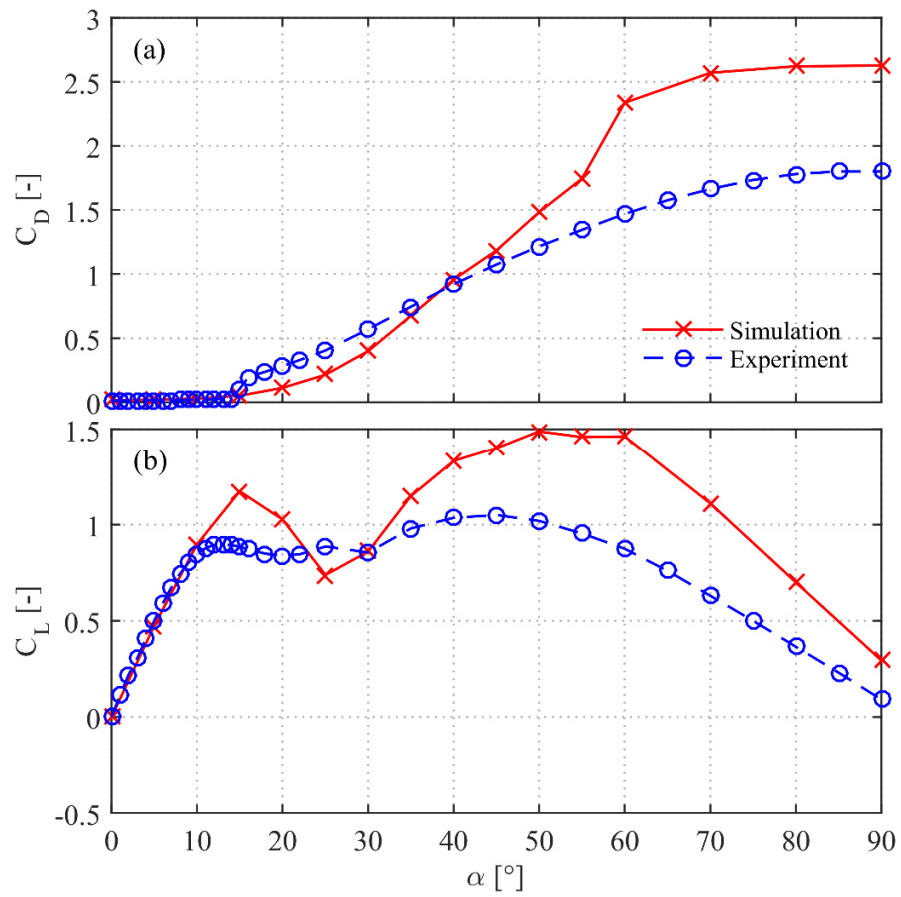


Figure 3.6: C_L and C_D values with respect to the angle of attack, α , obtained from simulations and experiments.

3.2.7.2. Validation of the CFD Model

The CFD model is validated using the field data obtained from the operation of a small VAWT, which was designed and built for experiments and is shown in Figure 3.7. The experimental VAWT is not connected to a load (i.e., $T_{gen} = 0$ N-m), but subject to friction and drag that need to be estimated. Coast-down tests were carried out when the blades and blade arms were on the rotor in the absence of wind, i.e., $T_{wind} = 0$ N-m. Admittedly, the additional drag from the blades in stationary fluid should be counted, but since streamlined NACA airfoils have very small drag when the angle of attack is zero, which is the case when there is no wind, this additional drag is neglected compared to the drag on the arms. Moreover, the flow developed due to the rotation of the blades, cross-blade interactions, and added-mass effects are neglected as well. Furthermore, the drag on the blade arms in the actual wind conditions could be larger than the drag during the coast-down experiment; these higher-order effects are neglected. Consequently, an assumed-constant friction coefficient (C_f), i.e., $T_f = C_f \omega$, is estimated from the solution of the equation of motion for the rotor given in (3.1), as follows:

$$J\dot{\omega} = -T_f \Rightarrow \omega(t) = \omega_0 e^{-C_f t/J} \Rightarrow C_f = \frac{J}{t_k} \ln \left(\frac{\omega_0}{\omega_k} \right) \quad (3.19)$$

where ω_0 is the initial rotor velocity, and ω_k is the velocity after t_k seconds.

Since the goal of the validation is the estimation of the turbine performance at relatively high angular velocities of the rotor, C_f values are estimated from the first two data points of each coast-down test which are 10 seconds apart. Average friction coefficient value is obtained as 0.0376 from total of four experiments.

Figure 3.8 shows the rotor velocity with respect to the wind velocity averaged and sampled with 10-second periods from field experiments, the linear fit to the experimental data, and the steady-state rotor angular velocities obtained from friction-corrected low resolution simulations for wind velocities between 3 and 6 m/s and a friction-corrected high resolution simulation for the wind velocity of 6 m/s. The simulation results after the correction for the friction demonstrate a good agreement with measurements as shown in Figure 3.8.



Figure 3.7: Experimental VAWT with the same dimensions used in the CFD model.

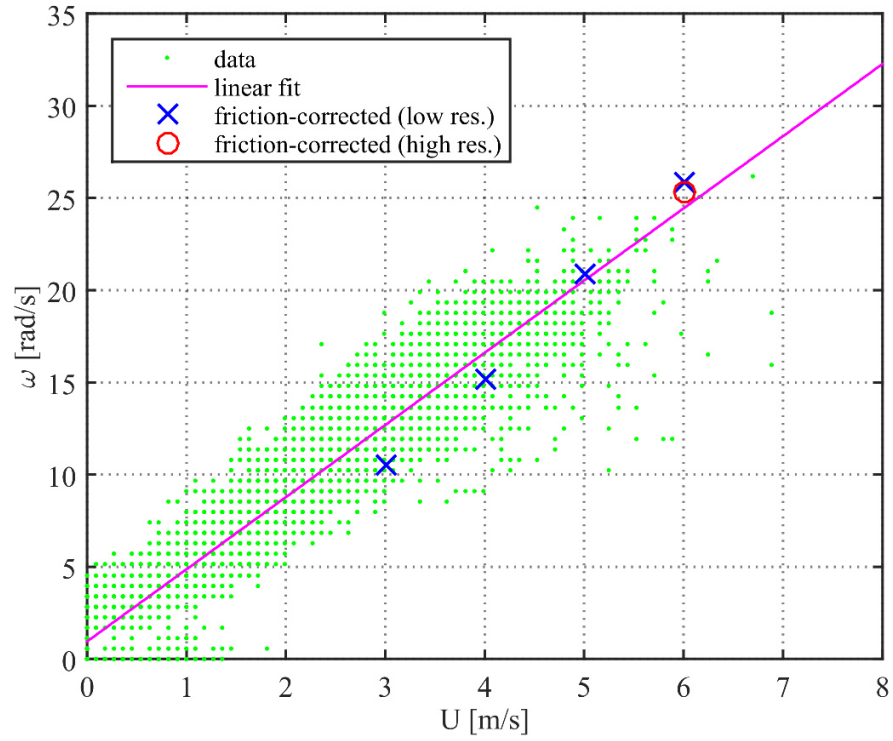


Figure 3.8: Measured and simulated angular velocities as a function of the wind velocity.

Figure 3.9 illustrates the variation of the rotor velocity throughout a coast-down test with the rotor velocity estimated from (3.19) for $C_f = 0.0376$. It is clear that the most drastic decay of the rotor velocity occurs at the first thirty seconds. Furthermore, the rotor velocity decreases to about 3 rad/s after 20 s, and the low (about 1.13 rad/s) precision of the velocity measurement, which is made through an Inspeed Vortex Wind Sensor attached to the shaft via a coupling, becomes a momentous factor. Thus, in order to avoid such inaccuracies as much as possible, only the first 10-second period is used while estimating the friction coefficient. Nevertheless, the resulting estimation for the rotor velocity seems to be consistent with the experimental data.

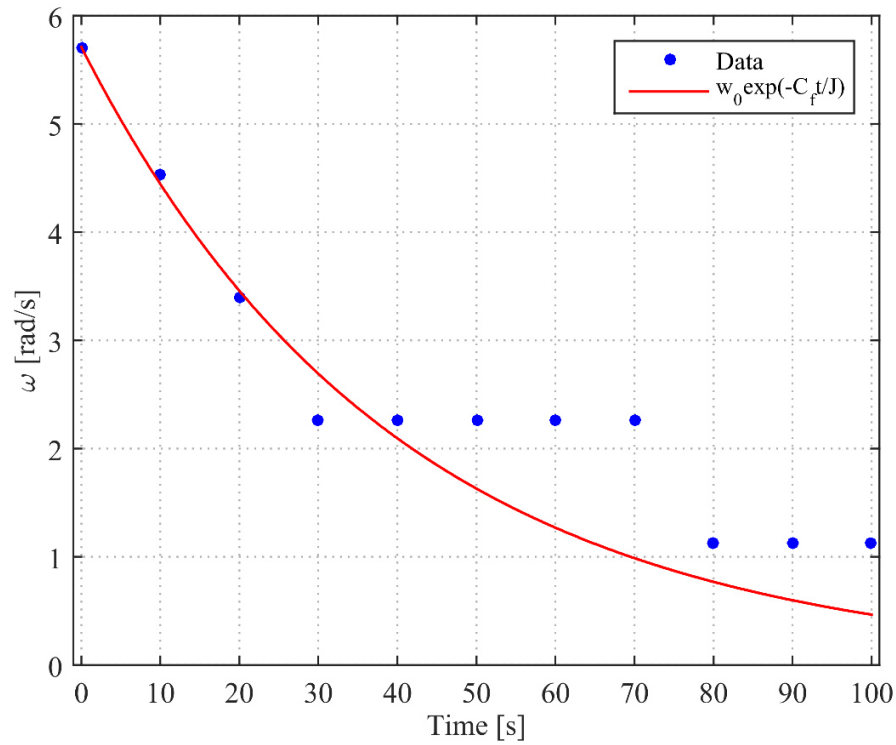


Figure 3.9: Variation of rotor velocity throughout a coast-down test along with the estimated rotor velocity for $C_f = 0.0376$.

Chapter 4

CONTROL

4.1. Simple Dynamic Simulation

Since CFD simulations require an excessive amount of time, a simple dynamic simulation based on a tip-speed ratio – power coefficient curve obtained from CFD simulations is used to design and test control algorithms. In this simulation, the wind torque is estimated as in (3.4), and the rotor dynamics in (3.1) is numerically solved by the forward Euler method with time steps $\Delta t = 1$ ms, as following:

$$\omega_{k+1} = \omega_k + \frac{T_{wind,k} - T_{gen,k}}{J} \Delta t \quad (3.20)$$

A tip-speed ratio – power coefficient curve obtained from high resolution CFD simulations for a wind velocity of 6 m/s (see Figure 4.1) is used to obtain the wind torque from (3.4). For this power coefficient curve, the peak value of the power coefficient, $C_{P,ref}$, is 0.3494 and the corresponding tip-speed ratio value, λ_{ref} , is 1.275. The process for power coefficient curve generation from CFD simulations is explained in detail in Chapter 6.

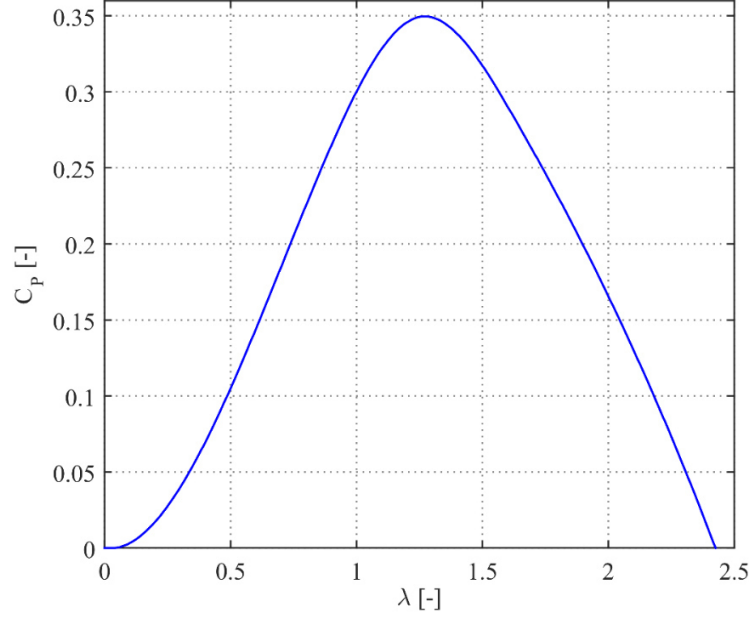


Figure 4.1: Tip-speed ratio – power coefficient curve obtained from CFD simulations for $U = 6$ m/s.

Control algorithms in this thesis are based on adjusting the generator torque. The control variable is the load coefficient or the generator torque itself (i.e., only for MPC) for CFD and simple dynamic simulations and the load current for HIL simulations. Thus, the control methods are defined and tuned in terms of the load coefficient or the generator torque here, and then they are modified and tuned separately for HIL simulations.

The discretized rotor dynamics in (3.20) can be rewritten in terms of the load coefficient as follows:

$$\omega_{k+1} = \omega_k + \frac{C_{P,k} \rho L R U_k^3 / \omega_k - K_{L,k} \omega_k}{J} \Delta t \quad (3.21)$$

Consequently, in both CFD and simple dynamic simulations, the load coefficient is manipulated as the control variable, and the generator torque and the power output are obtained from (3.10) and (3.11) with the rotor velocity calculated from (3.1) subject to wind torque from (3.5) for CFD simulations and with the rotor velocity calculated from (3.20) subject to wind torque from (3.4) for simple dynamic simulations.

In this case, it is assumed that the electrical system is ideal, i.e., no losses, and the generator is connected to a perfect power sink so that there is no constraint for energy production. On the other hand, the control variable and the power output are bounded below by zero and bounded above by the maximum limits of the generator voltage and current, $V_{L,\max}$ and $I_{L,\max}$:

$$0 \leq V_L \leq V_{L,\max} \quad (3.22)$$

$$0 \leq I_L \leq I_{L,\max} \quad (3.23)$$

Typically, small-scale VAWTs do not have practical mechanical limitations as HAWTs owing to their structural advantages. Nonetheless, the voltage and current constraints from the power electronic components also imply speed and torque constraints because of the electromagnetic characteristics of PMSGs that are shown in equations (3.6) and (3.7), e.g., the maximum voltage limit prevents over-speeding as well. Thus, it can be said that these limitations ensure the safe operation of the turbine. The control algorithms are enforced to respect these constraints by saturating the corresponding variables for MPPT and SNC algorithms and by solving the optimization problem subject to these constraints for MPC algorithm.

Since control aims to maximize the energy output of the turbine, the performance of control scenarios are compared on the basis of an energy metric, η_E , which is derived from the ratio of the actual energy output, E_{gen} , and the reference energy generation capacity, E_{ref} , during a period of time, $t_0 < t < t_f$, as follows:

$$\eta_E = \frac{E_{gen}}{E_{ref}} \quad (3.24)$$

The energy generated is calculated from:

$$E_{gen} = \int_{t=t_0}^{t_f} P_{gen} dt \quad (3.25)$$

Similarly, the reference maximum energy output is obtained from the integration of the reference aerodynamic power, $P_{wind,ref}$, which is the power that can be generated by the rotor when the power coefficient is kept at its maximum value, $C_{P,ref}$, continuously:

$$E_{ref} = \int_{t=t_0}^{t_f} P_{wind,ref} dt = \int_{t=t_0}^{t_f} C_{P,ref} \rho L R U^3 dt \quad (3.26)$$

For periodic wind cases such as sinusoidal wind, they are computed in the same manner yet only over the last period of the fluctuating wind so that the comparisons are consistent.

4.2. Wind Profiles

In order to test the performance of the control algorithms, a variety of wind profiles are used. A step wind profile is used to observe the step response of the system; a wind gust profile is used to study the transient performance; and a real wind data is used to test the performance under more realistic conditions.

The step wind profile used here consists of three intervals. In the first and last intervals, the wind velocity is 6 m/s, and in the second interval, the wind velocity is 10 m/s. A 60-second step wind is shown in Figure 4.2. As anticipated, the steady-state performance has more weight on the energy efficiency for this wind profile.

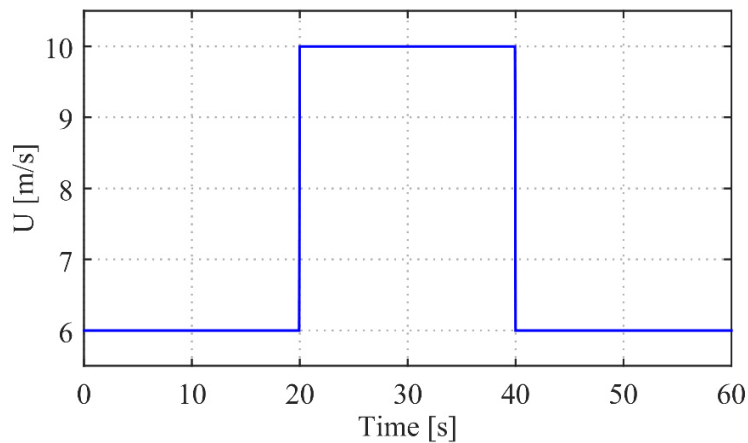


Figure 4.2: Step wind profile.

A standard gust shape that is used in related studies (e.g., [56] and [71]) is used to observe the extreme wind performance of the system. The shape of the gust is defined by the International Electrotechnical Commission (IEC) standards [72] and parameterized by the free-stream velocity, U_0 , the gust starting time, t_0 , the gust amplitude, u_e , and the gust period, T_g , as follows:

$$U = \begin{cases} U_0 - 0.37u_e \sin\left(\frac{3\pi(t-t_0)}{T_g}\right) \left[1 - \cos\left(\frac{2\pi(t-t_0)}{T_g}\right)\right], & \text{if } 0 \leq t-t_0 \leq T_g; \\ U_0, & \text{otherwise} \end{cases} \quad (3.27)$$

A 30-second wind gust is illustrated for $t_0 = 10$ s, $U_0 = 6$ m/s, $u_e = 5$ m/s, and $T_g = 10$ s in Figure 4.3. Clearly, the wind gust profile includes a substantial wind transient; hence, the transient performance has a greater impact for the wind gust profile.

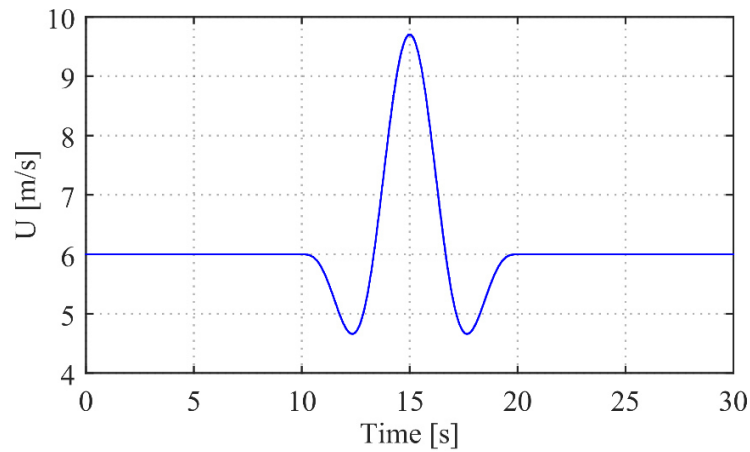


Figure 4.3: Wind gust profile.

A test with real wind data would yield significant observations for the system performance. The real wind data that is presented in [33] and was acquired while testing of a small-scale VAWT in urban wind conditions is used in this study. This wind profile includes fast dynamics as well as has a wide range, as shown in Figure 4.4.

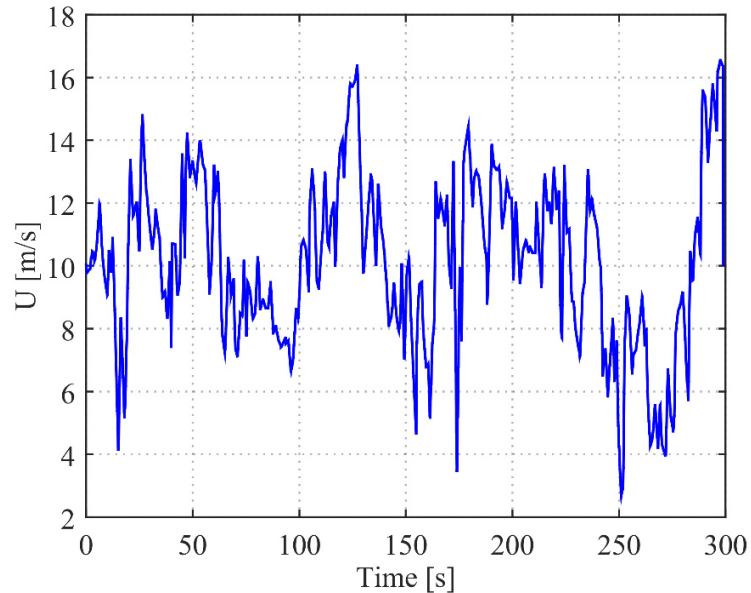


Figure 4.4: Real wind data.

4.3. Maximum Power Point Tracking

Maximum power point tracking is one of the most popular control techniques in literature for renewable energy systems. Here, we develop a model-free, ω -feedback, hill-climb searching MPPT algorithm which requires neither knowledge regarding the turbine nor wind speed measurement and determine the change of the load coefficient depending on only the rotor velocity measurements. Figure 4.5 shows the rotor velocity – power output characteristics for a WECS and the conditions for convergence to the maximum power point (MPP) which can be summarized as following. In order for an MPPT technique to converge the MPP for any wind velocity, it is sufficient to show that the power function relating the power output to the control variable has a single extremum that corresponds to the MPP [44].

Alternatively, the convergence to the MPP can be satisfied by designing an MPPT algorithm accordingly. For convergence to the MPP, the derivative of the power output with respect to the rotor velocity must be equal to zero at the MPP and greater than zero at the both sides of the MPP. Since our design is a ω -feedback control, it alters the control variable, K_L , depending on the rotor velocity. Thus, the conditions for the derivative of the load coefficient with respect to the rotor velocity that satisfy the conditions for the convergence to the MPP need to be derived.

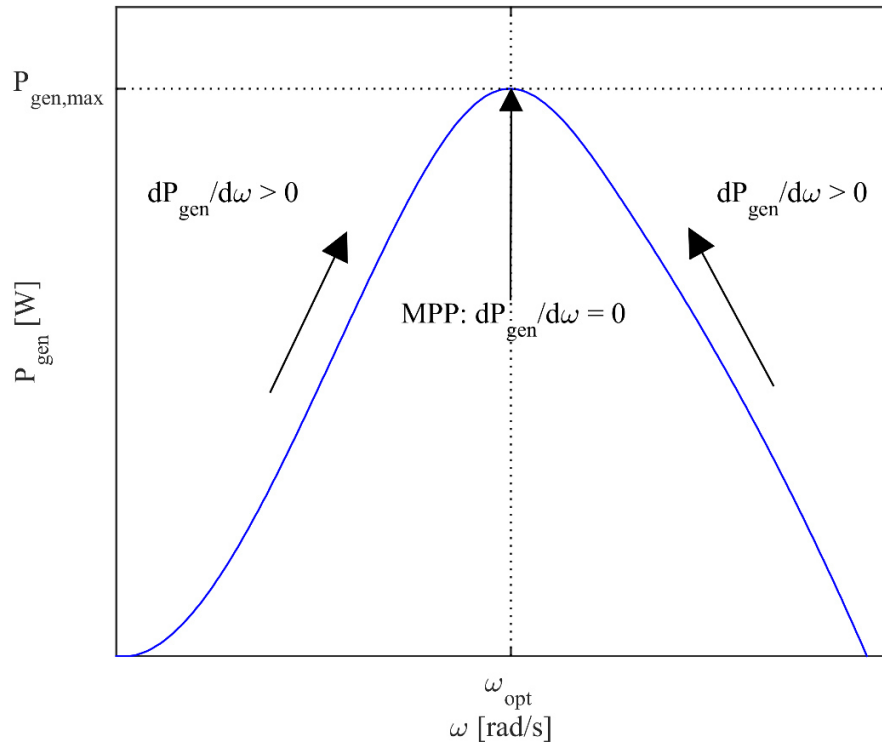


Figure 4.5: Rotor velocity – power output relation for a fixed wind velocity with the conditions for power maximization.

At the MPP, the following equation must hold:

$$\frac{dP_{gen}}{d\omega} = 0 \quad (3.28)$$

Taking the derivative of the generator power in (3.11) with respect to the rotor velocity yields:

$$\frac{dP_{gen}}{d\omega} = \frac{d(K_L\omega^2)}{d\omega} = \frac{dK_L}{d\omega}\omega^2 + 2K_L\omega \quad (3.29)$$

Since K_L is typically between 0 and 1 (e.g., its optimum value is about 0.2 for $U = 6$ m/s), and ω is a positive number that is two orders of magnitude greater than K_L , the second term in this expression can be neglected:

$$\frac{dP_{gen}}{d\omega} \cong \frac{dK_L}{d\omega} \omega^2 \quad (3.30)$$

Furthermore, usually, control is not applied when the rotor velocity is less than a certain limit, which is 5 rad/s in this thesis, therefore ω is always positive and the following condition must be satisfied at the MPP:

$$\frac{dK_L}{d\omega} = 0 \quad (3.31)$$

On the other hand, at the both sides of the MPP, the derivative of the power output with respect to the rotor velocity must be greater than zero so that the power output converges to the maximum point:

$$\frac{dP_{gen}}{d\omega} > 0 \quad (3.32)$$

Then, the following condition must be satisfied at the both sides of the MPP:

$$\frac{dK_L}{d\omega} > 0 \quad (3.33)$$

According to the conditions in (3.31) and (3.33), the variation of the control coefficient with respect to the rotor velocity must be zero at the MPP and must be positive otherwise. In other words, the change of the load coefficient must be in the same direction with the change of the rotor velocity except for the MPP. Thus, we propose a ω -feedback MPPT algorithm that varies the load coefficient in the same direction with the rotor velocity. The flowchart in Figure 4.6 illustrates the operation of this algorithm. Basically, it computes the change of the rotor velocity and sets the load coefficient based on this information. The change of the load coefficient, $\Delta K_{L,k}$, is determined differently for fixed-step and variable-step algorithms as described in the following subsections. For both methods, the control sampling period $T_S = 0.1$ s.

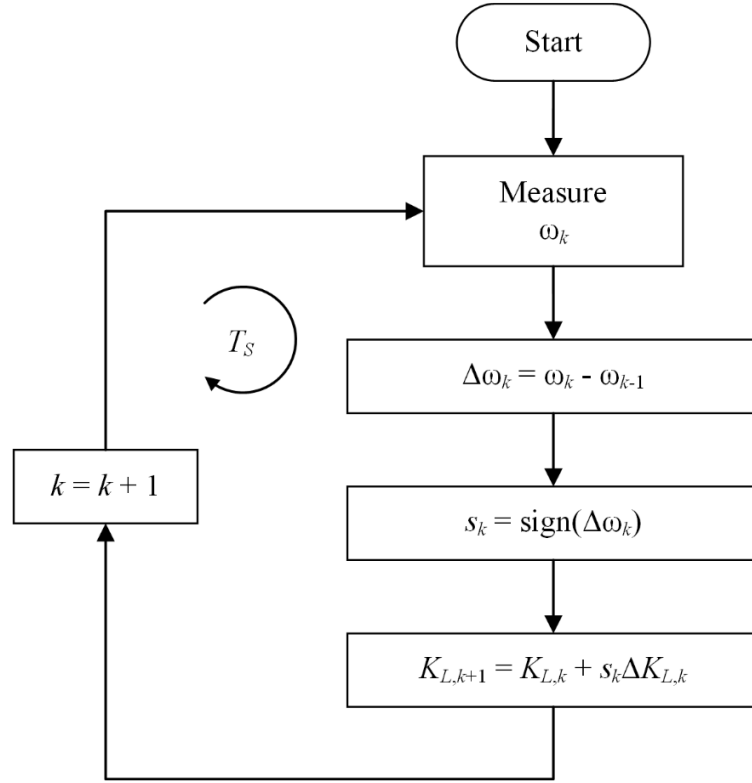


Figure 4.6: Flowchart of the ω -feedback MPPT algorithm

4.3.1. Fixed-step Maximum Power Point Tracking Algorithm

For the fixed-step MPPT algorithm, the change of the load coefficient is given by:

$$\Delta K_{L,k} = K_f \quad (3.34)$$

where K_f is the fixed step-size.

The value of K_f is determined through a parametric study on the simple dynamic simulation. 60-second step wind simulations, in which the initial rotor velocity is 5 rad/s, are run to find the value of K_f that provides the best performance in the sense of the energy efficiency. Table 4.1 tabularizes the results of the parametric study. As a result, the value of K_f is selected as 2.25×10^{-3} .

Table 4.1: Results of the parametric study for the tuning of fixed step-size.

$K_f [10^{-3}]$	0.75	1.00	1.25	1.50	1.75	2.00	2.25	2.50	2.75	3.00
$\eta_E [\%]$	73.15	80.23	85.37	88.99	91.36	92.89	93.20	92.63	90.92	88.89

4.3.2. Variable-step Maximum Power Point Tracking Algorithm

Even though the fixed-step method is easy to use and provides acceptable results in practice, it has certain drawbacks such as slow convergence to the MPP and oscillatory performance at steady-state which can be overcome by using variable control steps. Thus, we design a variable-step method for which the change of the load coefficient is proportional to the change of the rotor velocity through a gain, K_v :

$$\Delta K_{L,k} = K_v \Delta \omega_k \quad (3.35)$$

The tuning of the gain K_v is done likewise the tuning of K_f , and the results are given in Table 4.2. Consequently, the value of K_v is selected as 1.75×10^{-2} .

Table 4.2: Results of the parametric study for the tuning of variable-step gain.

$K_v [10^{-2}]$	0.75	1.00	1.25	1.50	1.75	2.00	2.25	2.50	2.75	3.00
$\eta_E [\%]$	81.45	87.67	91.23	92.84	92.94	91.90	90.10	87.82	85.26	82.58

4.4. Model Predictive Control

Model predictive control uses reliable models and anticipated events to optimize the control trajectory over a prediction horizon. In this thesis, we employ MPC approach to obtain the optimal control strategy for arbitrary wind conditions. For this purpose, an MPC that exploits wind speed predictions to maximize the energy generation subject to the electrical limitations is designed. A perfect prediction of the wind velocity over the prediction horizon is assumed. As distinct from the other control algorithms, the generator torque is manipulated in MPC so that the problem is similar to the related studies (e.g., [54-56]) and can be solved by convex optimization.

The goal is to find the generator torque trajectory that maximizes the energy generation subject to the voltage and current constraints. Thus, the cost function to be minimized is composed of three terms. The first term, Φ_E , is associated with the objective of energy maximization. Although the energy output of the generator is usually considered in related studies (e.g., [54-56]), here the mechanical energy of the rotor is taken into account since it also includes the kinetic energy of the rotor (i.e., the energy stored in the rotor) that can be exploited by MPC. Hence, Φ_E is the negative of the mechanical energy of the rotor:

$$\Phi_E = - \sum_{i=k}^{k+N-1} P_{wind,i} T_S \quad (3.36)$$

where k is the current step, N is the length of the prediction horizon, and T_S is the control sampling period. The second term, Φ_V , is a penalty for the violation of the voltage limits:

$$\Phi_V = \sum_{i=k}^{k+N-1} \left[(V_{L,i} > V_{L,max})(V_{L,i} - V_{L,max}) - (V_{L,i} < 0)V_{L,i} \right] T_S \quad (3.37)$$

where $V_{L,max}$ is the maximum load voltage limit which is 60 V in this case. Similarly, the third term, Φ_I , is a penalty for the violation of the current limits:

$$\Phi_I = \sum_{i=k}^{k+N-1} \left[(I_{L,i} > I_{L,max})(I_{L,i} - I_{L,max}) - (I_{L,i} < 0)I_{L,i} \right] T_S \quad (3.38)$$

where $I_{L,max}$ is the maximum load current limit which is 15 A in this case.

Thus, the cost function, Φ , is given by the weighted sum of the terms introduced above:

$$\Phi = w_1 \Phi_E + w_2 (\Phi_V + \Phi_I) \quad (3.39)$$

where w_1 and w_2 are the weights on the objectives of maximizing energy output and penalizing constraint violations, respectively, that need to be determined carefully for a satisfactory performance. For this particular VAWT system, the expected energy output for a minute is in the order of kJ and the violations of the electrical limits cannot be allowed; so the value of the weight associated with the energy cost $w_1 = 1$, while the value of the weight associated with the constraint violation cost $w_2 = 10^6$.

Consequently, the optimization problem is defined as:

$$\begin{aligned}
& \min_{T_{gen,k,\dots,k+M-1} \geq 0} w_1 \Phi_E + w_2 (\Phi_V + \Phi_I) \\
& \text{subject to} \\
& 0 \leq V_L \leq V_{L,\max} \\
& 0 \leq I_L \leq I_{L,\max}
\end{aligned} \tag{3.40}$$

where M is the length of the control horizon which is always less than or equal to N . In other words, there are M elements to be optimized, which are $T_{gen,k,\dots,k+M-1}$, and the remaining elements in the prediction horizon are equal to the M^{th} element, i.e.:

$$T_{gen,k+M,\dots,k+N-1} = T_{gen,k+M-1} \tag{3.41}$$

According to [54] and [55], the optimization problem in (3.40) can be approximated with convex terms and can be solved by a sequential quadratic programming (SQP) optimization method; similarly, [56] employs a trust-region-based SQP method. Thus, the SQP algorithm of the constrained nonlinear programming solver of Matlab (i.e., `fmincon`) is used for the dynamic optimization of the control trajectory by bounding the control variable below by zero. The termination tolerances on function value and the step-size are both 10^{-3} while the constraint tolerance is 10^{-6} .

Additionally, the control sampling period, the length of the prediction horizon, and the length of the control horizon need to be determined considering the trade-off between the performance and the computational cost. Since the time constant of the rotor is estimated to be in the order of 10 s, the prediction horizon should be at least 10 seconds. Using a control sampling period of 0.1 s would be preferable for this system but that corresponds to a control trajectory comprising of at least 100 elements which would make the optimization process compelling. Hence, the control sampling period is selected as 1 s and the lengths of the prediction and control horizons are selected as 10 so that a satisfactory performance can be obtained with a reasonable computation time.

At the beginning of the simulation, the optimization procedure is initialized for a control trajectory that is set to the reference value of the generator torque for the initial wind velocity, which is derived by dividing the maximum power output by the corresponding rotor

velocity. Then, the resulting optimal control trajectory is shifted and used to initialize the optimization for the next step.

4.5. Simple Nonlinear Control

MPC operates in a receding horizon procedure, namely it computes the optimal control trajectory by taking into account disturbance predictions (i.e., the wind velocity in this case), applies the first element to the plant and shifts the prediction horizon one step forward and repeats the same process; therefore, it requires high computational power as well as a prediction system which may restrict its use for small-scale systems. Thus, we observe the behavior of the MPC that manipulates the generator torque for energy maximization and design a simple, ω -feedback MPC-mimicking control for practical use, which is called simple nonlinear control. As distinct from the MPC, the SNC operates at a sampling period of 0.1 s which would be a challenging sampling rate for MPC due to computational burden. Moreover, SNC manipulates the load coefficient, K_L , to vary the generator torque, which is indeed not an advantage yet changing the control variable may deteriorate the performance of the MPC since the optimization problem may not be well-defined.

Figure 4.7 depicts the step response of the MPC including the rotor velocity and generator torque and power variations. Here, the references represent the optimal values for which the power output is maximum for the given wind velocity. The observations regarding the behavior of the MPC based on the generator torque and the rotor velocity states can be summarized as follows:

- when the rotor is too slow with respect to the optimal velocity (e.g., $0 < t < 5$ s in Figure 4.7), it does not load the generator;
- when the rotor is too fast with respect to the optimal velocity (e.g., $50 < t < 60$ s in Figure 4.7), it generates high amount of torques;
- when the rotor velocity is around the optimal value, it adjusts the generator torque such that the rotor velocity converges to the optimal value (e.g., $5 < t < 10$ s in Figure 4.7); and

- when the rotor velocity is at the optimal value, it sets the generator torque to the optimal value.

As a result, the turbine operates at the MPP for the most of the time and is observed to generate more energy than the case in which the MPP is tried to be tracked continuously, i.e., MPPT.

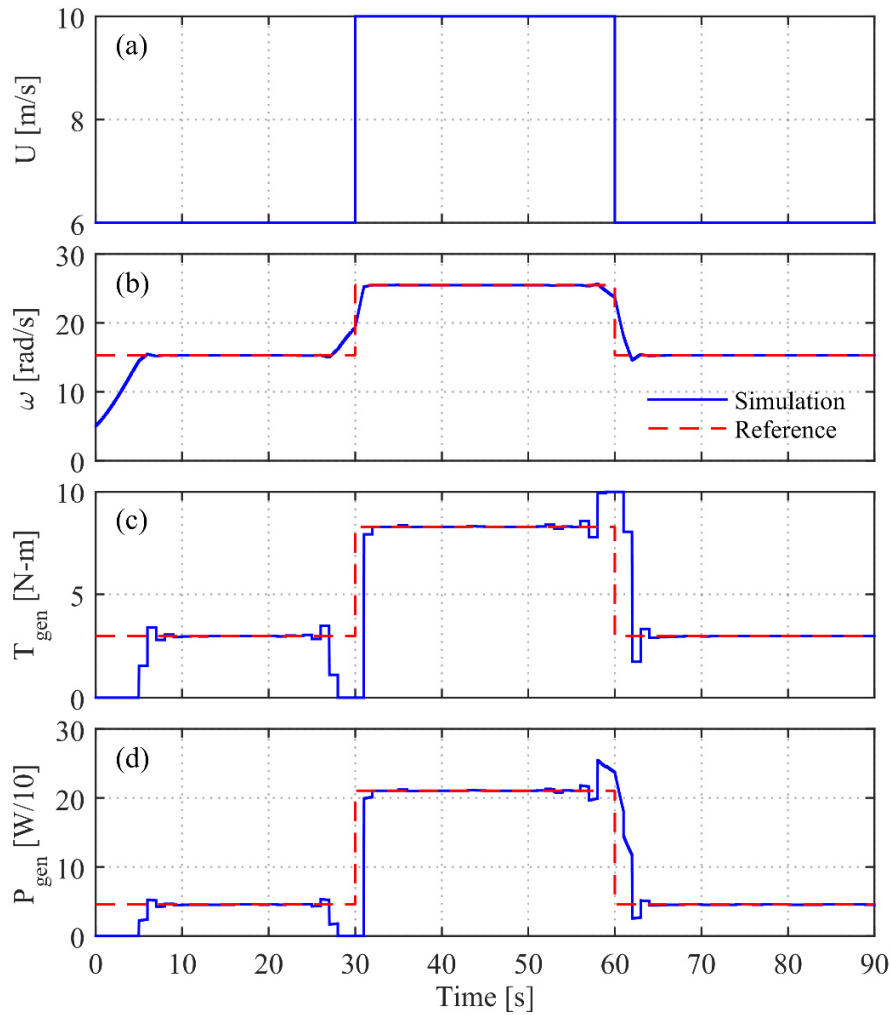


Figure 4.7: Rotor velocity (b), generator torque (c), and generator power (d) responses of the MPC for step wind (a).

In order to mimic the MPC characteristics, the SNC is defined as a piecewise function of the rotor velocity. When ω is lower than a lower limit, ω_L , the load coefficient equals to zero; and when ω is higher than an upper limit, ω_U , the load coefficient equals to the maximum value, $K_{L,max}$. Between the lower and upper rotor velocity limits, a proportional

(P) control is employed to drive the rotor velocity to its reference value, ω_{ref} , which corresponds to the reference value of the load coefficient, $K_{L,ref}$. The formulation of the load coefficient for SNC reads:

$$K_{L,k} = \begin{cases} 0 & , \text{ if } \omega_k \leq \omega_{L,k} \\ K_{L,ref,k} - \frac{K_{L,ref,k}}{\omega_{ref,k} - \omega_{L,k}} K_P e_k & , \text{ if } \omega_{L,k} < \omega_k \leq \omega_{ref,k} \\ K_{L,ref,k} + \frac{K_{L,ref,k}}{\omega_{ref,k} - \omega_{U,k}} K_P e_k & , \text{ if } \omega_{ref,k} < \omega_k < \omega_{U,k} \\ K_{L,max,k} & , \text{ if } \omega_k \geq \omega_{U,k} \end{cases} \quad (3.42)$$

where e is the deviation of the rotor velocity from the reference velocity (i.e., $e = \omega_{ref} - \omega$) and K_P is the proportional gain.

The reference value of the rotor velocity is derived from the reference value of the tip-speed ratio, λ_{ref} , that corresponds to the peak of the power coefficient curve, $C_{P,ref}$, and the wind velocity:

$$\omega_{ref} = \frac{\lambda_{ref} U}{R} \quad (3.43)$$

and the reference value for the load coefficient is derived from the maximum power, $P_{wind,ref}$, or the corresponding power coefficient, $C_{P,ref}$, and the wind velocity:

$$K_{L,ref} = \frac{P_{wind,ref}}{\omega_{ref}^2} = \frac{C_{P,ref} \rho L R U^3}{\omega_{ref}^2} \quad (3.44)$$

Therefore, the reference values are functions the wind velocity and updated continuously during the operation. The maximum value of the load coefficient is selected as the twice of the reference value.

Similarly, the lower and upper limits of ω are derived from the lower and upper tip-speed ratio limits, λ_L and λ_U , that are obtained from the power coefficient curve as follows. For a given level of the power coefficient, γC_P , lower and upper limits of the tip-speed ratio are defined as the lower and upper bounds of the tip-speed ratio for which the power coefficient, $C_P(\lambda)$, is greater than $\gamma C_{P,ref}$ as shown in Figure 4.8.

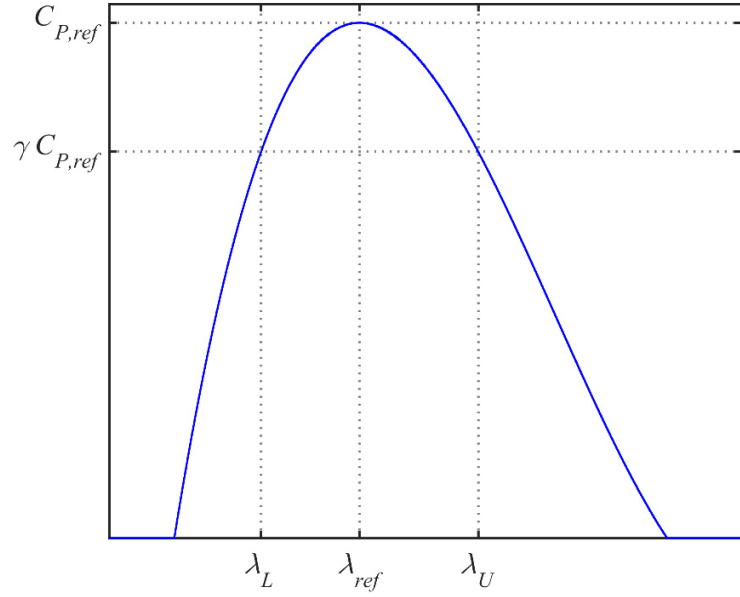


Figure 4.8: Estimation of the lower and upper tip-speed ratio limits.

Thus, the SNC parameters that need to be tuned are the proportional gain, K_P , and the level of the power coefficient curve that provides the lower and upper tip-speed ratio limits, γ . The same procedure that is used for the tuning of the MPPT algorithms is carried out to tune these parameters. Search for K_P and γ shows that the energy efficiency, η_E , enhances as K_P and γ increase, see Table 4.3 for the energy efficiency results; however, $K_P > 1$ causes negative K_L values and $\gamma > 99\%$ causes undesired high frequency oscillations. Thus, the values of K_P and γ are selected as 1 and 99%, respectively.

Table 4.3: Energy efficiency results of the parametric study for the tuning of SNC.

γ [-] \backslash K_P [-]	0.25	0.50	0.75	1.00
25%	90.502%	91.681%	92.493%	93.091%
50%	91.727%	92.656%	93.259%	93.685%
75%	93.365%	93.756%	93.988%	94.142%
99%	94.326%	94.331%	94.333%	94.334%

Chapter 5

HARDWARE-IN-THE-LOOP SIMULATION

The generator efficiency, η_{gen} varies substantially depending on the operating conditions, and this should be considered in order to obtain a more realistic simulation of the actual VAWT system. On the other hand, detailed wind tunnel tests for the control of an actual VAWT are difficult and expensive. Thus, the HIL simulation developed for a small-scale VAWT in [16,19] is employed here to study the impact of the electromechanical components on power characteristics, to modify the control designs accordingly, and to test the performance of the control and the mechanical to electrical power conversion under arbitrary wind conditions. In this thesis, the HIL simulation is explained briefly, however a detailed description can be found in [16].

The schematics of the VAWT system and the HIL test-bed are illustrated in Figure 5.1. The VAWT system shown in Figure 5.1a consists of the rotor that is composed of the blades and the arms, a vertical shaft that connects the rotor to the generator, and a power electronics & control medium that interconnects the generator and the load. The HIL test-bed shown in Figure 5.1b comprises of a PC, an electrical motor and a gearbox to emulate the VAWT rotor, and the electromechanical and power electronics hardware that are intended to be used in the actual system. Here, T_m is the torque induced by the motor, ω_m is the angular velocity of the motor, J_m is the equivalent moment of inertia at the motor shaft, and T_{load} is the total torque on the motor shaft including the generator, friction and cogging torques. The hardware and the PC, which operates the software for the emulation and the control, are interconnected through a dSPACE interface.

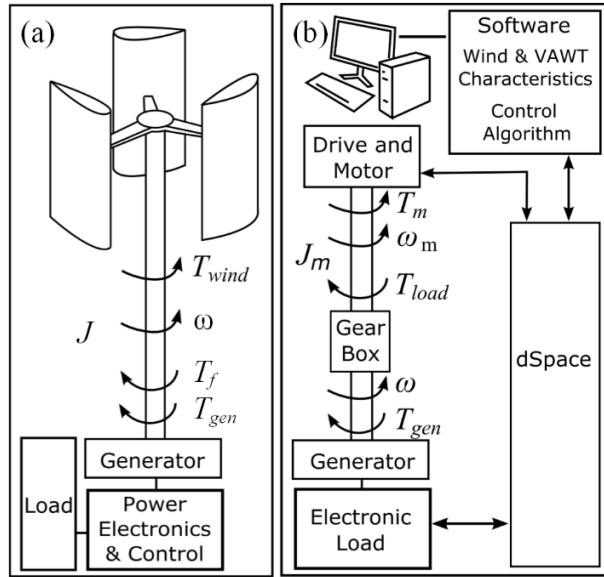


Figure 5.1: Schematics of the VAWT system (a) and the HIL test-bed (b) [16].

Figure 5.2 shows an image of the HIL test-bed consisting of a PC, a dSPACE toolkit (DS1104), a permanent magnet synchronous motor (FEMSAN 5F100810001), a motor driver (TDE MACNO MOPDE B-6.8A), a gearbox (YILMAZ REDUKTOR MN002- B07), a custom PMSG produced for the actual VAWT system by FEMSAN, a full-bridge rectifier, and a programmable electronic-load (Agilent N3306A) as the power sink.

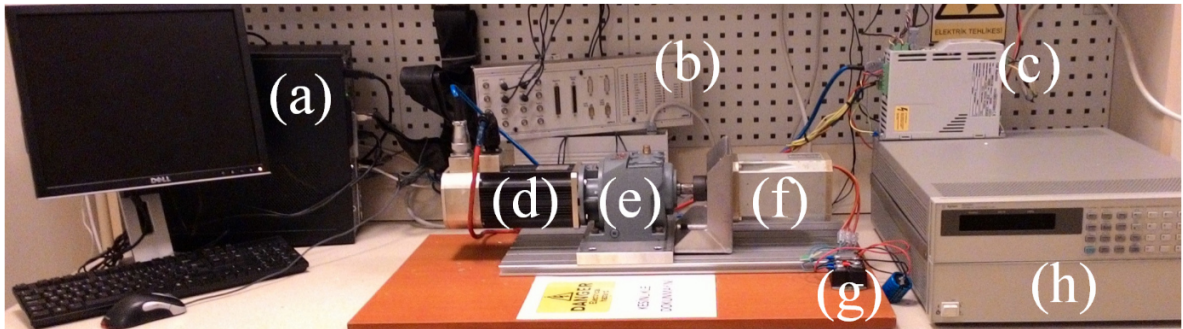


Figure 5.2: An image of the HIL test-bed consisting of a PC (a), a dSPACE toolkit (b), a motor driver (c), an electrical motor (d), a gearbox (e), a generator (f), a rectifier (g), and a programmable electronic-load (h).

In the HIL simulation, the dynamics of the VAWT rotor that converts the wind power into mechanical power is emulated by the electrical motor and the gearbox. For this purpose, the motor torque is calculated by taking into account the wind torque and the generator torque; moreover, disturbance torques caused by the friction in the drivetrain and the cogging

torque of the generator are overcome by using a disturbance torque compensator comprising of a virtual plant and a proportional-integral (PI) controller. The last factor needs to be considered for the motor torque calculation is the gear ratio of the gearbox that converts the high velocity – low torque output of the motor to a low velocity – high torque input for the generator. The generator output is connected to the programmable electronic load through the full-bridge rectifier. The motor torque and the load current values are determined in a MATLAB/Simulink simulation and sent to the motor driver and the electronic load, respectively, via the dSPACE toolkit.

For HIL simulations, the $\lambda - C_P$ curve shown in Figure 5.3 is used to estimate the wind torque from (3.4) for a given wind velocity, and the rotor dynamics is numerically solved by the forward Euler method as given in (3.20) with time steps $\Delta t = 1$ ms. Additionally, the moment of inertia of the rotor, J , is $2 \text{ kg}\cdot\text{m}^2$, and the friction torque, T_f , is estimated as a function of the angular velocity of the motor, ω_m , from HIL experiments:

$$T_f(\omega_m) = -1.417 \times 10^{-6} \omega_m^2 + 1.327 \times 10^{-3} \omega_m + 0.175 \quad (4.1)$$

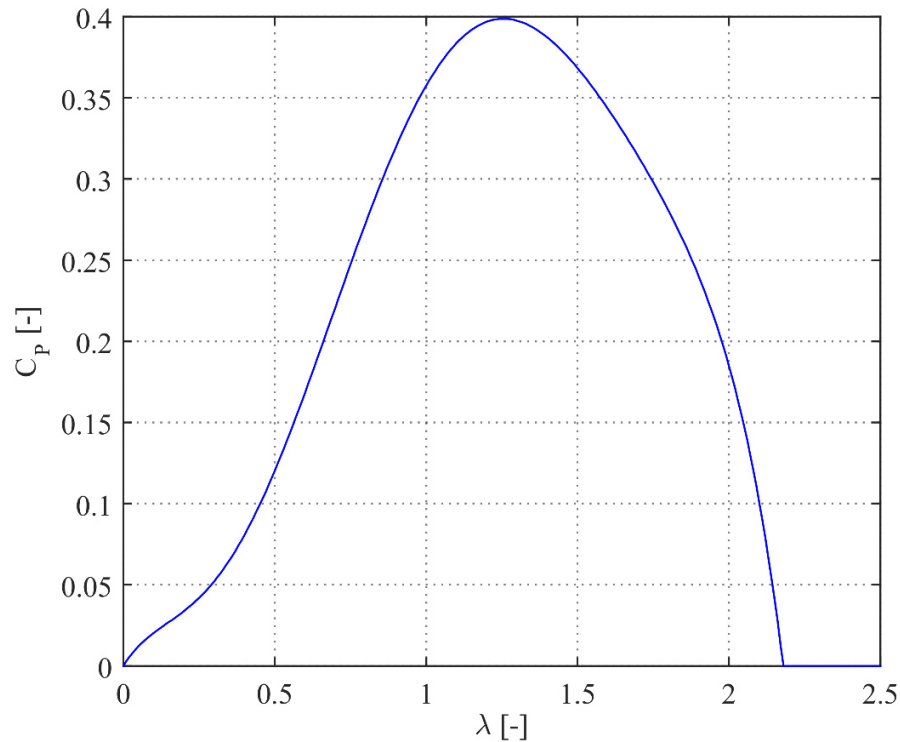


Figure 5.3: $\lambda - C_P$ curve used for HIL simulations.

5.1. Electromechanical Simulation

Since the HIL simulation operates in real-time, it may not allow computationally expensive control techniques such as MPC. On the other hand, the HIL simulation can be reduced into an electromechanical simulation, i.e., a software-only simulation, by modeling the hardware components on the HIL test-bed and validating the model through the experimental data. In other words, the simple dynamic simulation described in Chapter 4 can be improved by replacing the ideal electrical model by a non-ideal electrical model which is validated through the experimental data of the actual components.

In the HIL test-bed, a PMSG, a passive full-bridge rectifier, and a programmable electronic-load, which is operated in constant-current mode, are used for mechanical to DC electrical power conversion. For this electromechanical system, the load voltage is correlated with the rotor velocity; however, the load voltage is at the maximum value when the load current is zero and decreases as the load current increases, namely a voltage drop occurs when the load current is non-zero due to the losses of the non-ideal components. Thus, a power loss model is required to estimate the power output and the load voltage for given rotor velocity and load current.

The three-phase PMSG – rectifier – load model shown in Figure 5.4a can be simplified into the equivalent DC model shown in Figure 5.4b. In Figure 5.4a, E_{LN} is the line-to-neutral voltage due to the back EMF, L_S and R_S are the phase inductance and resistance, and I_L and V_L are the load current and voltage, respectively. Since the electronic-load is operated in constant-current mode, it is modeled as a current sink. Whereas, E_{dc} , L_{dc} , and R_{dc} in Figure 5.4b represent the DC equivalents of the three-phase back EMF voltage, phase inductance, and phase resistance, respectively, and calculated as below:

$$E_{dc} = 3\sqrt{6}E_{LN} / \pi \quad (4.2)$$

$$L_{dc} = 18L_S / \pi^2 \quad (4.3)$$

$$R_{dc} = 18R_S / \pi^2 \quad (4.4)$$

The back EMF voltage of the PMSG is calculated from:

$$E_{LN} = \varphi_S p \omega \quad (4.5)$$

where φ_S is the flux due to the permanent magnets and p is the number of pole pairs, which are specific to the PMSG as L_S and R_S . On the other hand, in order take into account the armature reaction in the PMSG and the overlapping currents in the rectifier, an additional resistance term, R_{over} , is included in the DC model that is calculated by:

$$R_{over} = 3L_S p \omega / \pi \quad (4.6)$$

Lastly, the full-bridge rectifier that consists of 6 diodes introduces a voltage drop that is equal to two times the diode threshold voltage, V_{th} , since two diodes commute for each phase.

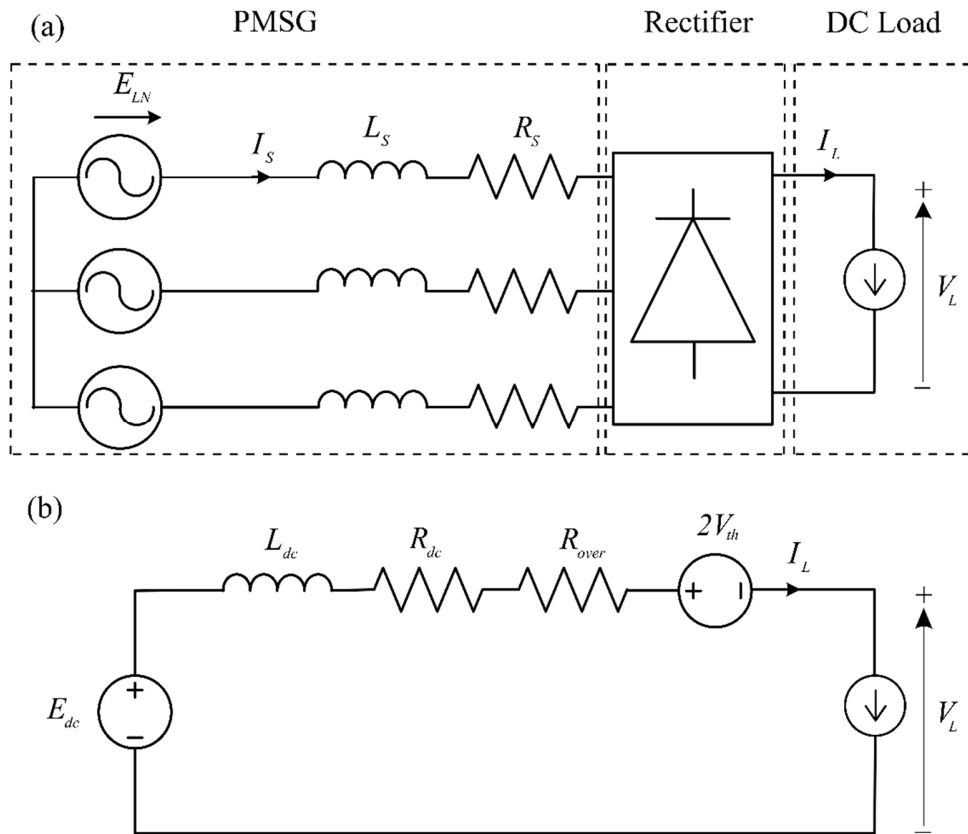


Figure 5.4: Three-phase PMSG – rectifier – load model (a) and the equivalent DC model (b) [16].

Although the electronic-load provides a pure-resistive power sink, the real power and the apparent power are not equal for this system due to the phase inductances. The apparent power, S , is given by:

$$S = E_{dc} I_L \quad (4.7)$$

while the reactive power, Q , that is consumed by the inductance is:

$$Q = L_{dc} p \omega I_L^2 \quad (4.8)$$

As a result, the following real power, P_R , is produced:

$$P_R = \sqrt{S^2 - Q^2} \quad (4.9)$$

Moreover, the phase resistances in the PMSG and the resistance and the voltage drop associated with the rectifier cause power losses, $P_{L,phases}$ and $P_{L,rectifier}$ respectively, as well:

$$P_{L,phases} = R_{dc} I_L^2 \quad (4.10)$$

$$P_{L,rectifier} = R_{over} I_L^2 + 2V_{th} I_L \quad (4.11)$$

Consequently, the power output, P_{gen} , is obtained as below for given load current I_L , and rotor velocity, ω :

$$\begin{aligned} P_{gen} &= P_R - P_{L,phases} - P_{L,rectifier} \\ &= \sqrt{(E_{dc} I_L)^2 - (L_{dc} p \omega I_L^2)^2} - R_{dc} I_L^2 - R_{over} I_L^2 - 2V_{th} I_L \end{aligned} \quad (4.12)$$

Alternatively, the power output can be calculated from the load voltage and the load current:

$$P_{gen} = V_L I_L \quad (4.13)$$

Hence, the load voltage can be calculated by dividing the power output by the load current:

$$V_L = \sqrt{E_{dc}^2 - (p \omega L_{dc} I_L)^2} - (R_{dc} + R_{over}) I_L - 2V_{th} \quad (4.14)$$

The torque constant K_t that relates the generator torque to the load current (i.e., $T_{gen} = K_t I_L$) is calculated by:

$$K_t = 3\sqrt{6} p \phi_s / \pi \quad (4.15)$$

The flux, phase resistance, and phase inductance of the PMSG and the threshold voltage of the diodes are estimated through the least squares regression method for the experimental data from HIL simulations for a range of load current and rotor velocity values. The resulting values of the parameters regarding the electrical model are tabularized in Table 5.1.

Table 5.1: Electromechanical model parameters

Parameter	Symbol	Value	Unit
Number of pole pairs	p	6	-
Flux	φ_S	0.1060	V-s/rad
Phase inductance	L_S	3.3000	mH
Equivalent DC inductance	L_{dc}	6.0184	mH
Phase resistance	R_S	1.5500	Ω
Equivalent DC resistance	R_{dc}	2.8269	Ω
Diode threshold voltage	V_{th}	0.770	V
Torque constant	K_t	1.4877	N-m/A

5.1.1. Validation of Electromechanical Model

The electromechanical model provides the load voltage and the power output as a function of the rotor velocity and the load current likewise the HIL simulation. In order to show that the model provides realistic results, HIL simulations are performed by fixing the rotor velocity and increasing the load current gradually. Then, the experimental data is compared to the estimations obtained from electromechanical simulations under the same conditions. According to Figure 5.5a, the load voltage values estimated from the electromechanical model with respect to the load current and the rotor velocity agree with the experimental data. Furthermore, the power output estimations are also consistent with the experimental data, as shown in Figure 5.5b. It is seen that the electromechanical model slightly underestimates the load voltage and the resulting power output as the rotor velocity decreases and the load current increases (about 3%) thus one can say that the electromechanical model is a valid tool to estimate the power output of the complete VAWT system.

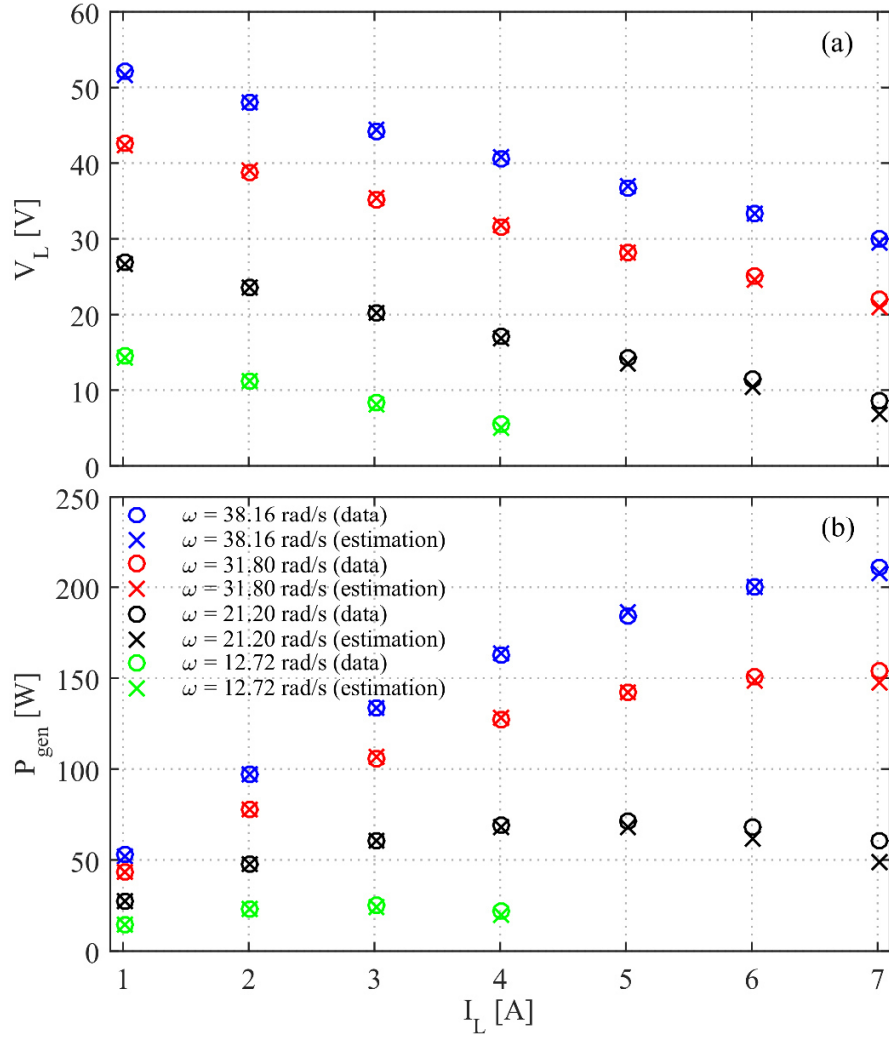


Figure 5.5: Voltage drop (a) and power output (b) values for fixed rotor velocity and load current conditions obtained from HIL simulations and electromechanical simulations.

5.2. Control

In HIL simulations, the power characteristics is affected dramatically by the hardware components. Moreover, the control variable is the load current differently than the CFD and the simple dynamic models and V_L -feedback control algorithms are favorable since the electronic-load provides real-time data for the load voltage. Hence, the control designs need to be modified and tuned accordingly.

5.2.1. Maximum Power Point Tracking

The MPPT algorithm defined in Chapter 4 needs to be modified for HIL simulations so that it changes the load current based on the load voltage measurements. The load current at next time step can be expressed in terms of the change of the load current, $\Delta I_{L,k}$:

$$I_{L,k+1} = I_{L,k} + \Delta I_{L,k} \quad (4.16)$$

Similarly, the load voltage at next time step can be expressed in terms of the change of the load voltage, $\Delta V_{L,k}$:

$$V_{L,k+1} = V_{L,k} + \Delta V_{L,k} \quad (4.17)$$

On the other hand, the change of the load voltage can be defined as the rate of change of the load voltage with respect to the load current multiplied by the change of the load current, as follows:

$$\Delta V_{L,k} = \left. \frac{\partial V_L}{\partial I_L} \right|_{k, \omega_k} \Delta I_{L,k} \quad (4.18)$$

The partial derivative of the load voltage at time step k , when the rotor velocity ω_k does not vary significantly, is negative with respect to the load current due to Ohm's law, i.e.:

$$\left. \frac{\partial V_L}{\partial I_L} \right|_{k, \omega_k} = -\kappa \quad (4.19)$$

where κ is a positive constant. Therefore, the load voltage at next time step can be rewritten as:

$$V_{L,k+1} = V_{L,k} - \kappa \Delta I_{L,k} \quad (4.20)$$

The change of the power output between two consecutive time steps reads:

$$\Delta P_{gen,k} = P_{gen,k+1} - P_{gen,k} = (V_{L,k+1} I_{L,k+1}) - (V_{L,k} I_{L,k}) \quad (4.21)$$

Substituting (4.16) and (4.20) in (4.21) yields:

$$\begin{aligned} \Delta P_{gen,k} &= (V_{L,k} - \kappa \Delta I_{L,k})(I_{L,k} + \Delta I_{L,k}) - (V_{L,k} I_{L,k}) \\ &= V_{L,k} I_{L,k} + V_{L,k} \Delta I_{L,k} - \kappa I_{L,k} \Delta I_{L,k} - \kappa (\Delta I_{L,k})^2 - V_{L,k} I_{L,k} \\ &= V_{L,k} \Delta I_{L,k} - \kappa I_{L,k} \Delta I_{L,k} - \kappa (\Delta I_{L,k})^2 \end{aligned} \quad (4.22)$$

The variation of the power output with respect to the load current must be zero at the MPP, then:

$$\left. \frac{\partial P_{gen}}{\partial I_L} \right|_k \approx \frac{\Delta P_{gen,k}}{\Delta I_{L,k}} = 0 \Rightarrow V_{L,k} - \kappa I_{L,k} - \kappa \Delta I_{L,k} = 0 \Rightarrow \kappa I_{L,k+1} = V_{L,k} \quad (4.23)$$

By subtracting $\kappa I_{L,k} = V_{L,k-1}$ (according to (4.23)) from both sides, we obtain:

$$\kappa (I_{L,k+1} - I_{L,k}) = V_{L,k} - V_{L,k-1} \quad (4.24)$$

Using (4.16) and (4.20), this expression can be rewritten as:

$$\Delta I_{L,k+1} = \frac{1}{\kappa} \Delta V_{L,k} \quad (4.25)$$

Thus, for power maximization, the change of the load current must be in the same direction with the change of the load voltage, furthermore, should be proportional to the change of the load voltage if the step-size is variable. Thus, a V_L -feedback MPPT algorithm that varies the load coefficient in the same direction with the load voltage is proposed. The flowchart in Figure 5.6 illustrates the operation of this algorithm. Basically, it computes the change of the load voltage based on load voltage measurements and changes the load current accordingly. The change of the load current, $\Delta I_{L,k}$, is determined differently for fixed-step and variable-step algorithms as described in the following subsections. For both methods, the control sampling period $T_S = 0.1$ s.

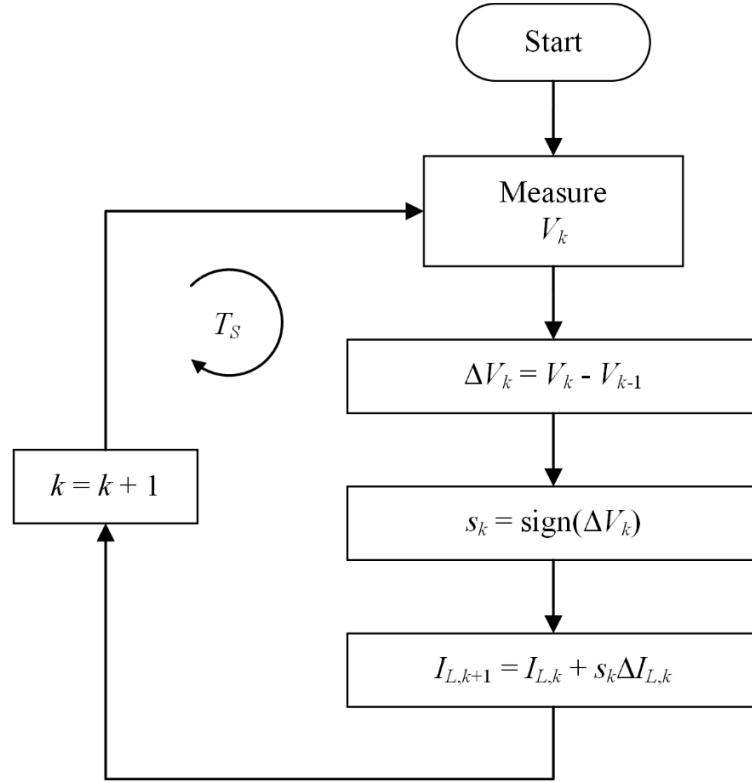


Figure 5.6: Flowchart of the V_L -feedback MPPT algorithm.

5.2.1.1. Fixed-step Maximum Power Point Tracking

For the fixed-step MPPT, the load current step-size is given by:

$$\Delta I_{L,k} = K_f \quad (4.26)$$

where K_f is the fixed step-size that is determined through a parametric study on the HIL test-bed. It is observed that larger values for K_f not only reduce the convergence time to the MPP but also increase the jitter; hence, the value of K_f is selected considering the trade-off as 0.06.

5.2.1.2. Variable-step Maximum Power Point Tracking

In addition to the sign of the change of the load current, (4.25) also suggests that the magnitude of the change of the load current should be proportional to the change of the load voltage. Hence, the step-size for the variable-step MPPT is proportional to the change of the load voltage through a gain, K_v :

$$\Delta I_{L,k} = K_v |\Delta V_{L,k}| \quad (4.27)$$

The variable step-size reduces the impact of the trade-off between the convergence time and the jitter significantly, however the selection of K_v is still crucial for the performance. The value of K_v is selected as 0.2 through a parametric study through HIL simulations.

5.2.2. Model Predictive Control

In real-time applications, MPC is not applicable due to its computational cost; nevertheless, it can be implemented within the simulation environment to observe its behavior and develop a simpler control strategy that eliminates the drawbacks of MPC.

Slightly different than the MPC described in Chapter 4, the MPC for HIL simulation manipulates the load current, which is proportional to the generator torque with a constant. Thus, the goal is find the load current trajectory that maximizes the energy output subject to the voltage and current constraints. Although the cost function associated with the objective of energy maximization, Φ_E , is the negative of the mechanical energy output of the rotor for the MPC developed for the simple dynamic simulation, it is observed that the non-ideal electrical model in the electromechanical simulation affects the power characteristics substantially and that using C_{Pgen} instead of C_P deteriorates the performance; hence, here, Φ_E is replaced by the negative of the energy output of the system:

$$\Phi_E = - \sum_{i=k}^{k+N-1} P_{gen,i} T_S \quad (4.28)$$

The remaining part of the composite cost function and the values of the weights are not changed, i.e., $w_1 = 1$ and $w_2 = 10^6$. Hence, the optimization problem becomes:

$$\begin{aligned}
 & \min_{I_L, k, \dots, k+M-1 \geq 0} w_1 \Phi_E + w_2 (\Phi_V + \Phi_I) \\
 & \text{subject to} \\
 & \quad 0 \leq V_L \leq V_{L,\max} \\
 & \quad 0 \leq I_L \leq I_{L,\max}
 \end{aligned} \tag{4.29}$$

Since the lower current limit bounds the control variable below by zero as well, it is not necessary to solve the problem by a constrained solver. The maximum voltage and current limits ($V_{L,\max}$ and $I_{L,\max}$) are hard constraints and 60 V and 15 A, respectively. Moreover, the quasi-newton algorithm of the unconstrained nonlinear programming solver of Matlab (i.e., `fminunc`) is found to perform more efficient than the SQP algorithm; therefore, the quasi-newton algorithm is employed in the solution of the optimization problem here. The termination tolerances on the value of the function and the step-size are both 10^{-2} . The control sampling period, the length of the prediction horizon, and the length of the control horizon are kept unchanged (i.e., $T_S = 1$ s, $N = 10$, $M = 10$) so that a satisfactory performance can be obtained with a reasonable computation time.

5.2.3. Simple Nonlinear Control

The SNC needs to be modified from the original form in Chapter 4 so that it manipulates the load current based on the load voltage feedback. Thus, the relation between the load voltage and the load current responses of the MPC needs to be observed; nevertheless, the velocity and the voltage as well as the torque and the current are correlated for a PMSG. Consequently, the formulation of the SNC for HIL and electromechanical simulations reads:

$$I_{L,k} = \begin{cases} 0 & , \text{ if } V_{L,k} \leq V_{L,L,k} \\ I_{L,ref,k} - \frac{I_{L,ref,k}}{V_{L,ref,k} - V_{L,L,k}} K_P e_k, & \text{ if } V_{L,L,k} < V_{L,k} \leq V_{L,ref,k} \\ I_{L,ref,k} + \frac{I_{L,ref,k}}{V_{L,ref,k} - V_{L,U,k}} K_P e_k, & \text{ if } V_{L,ref,k} < V_{L,k} < V_{L,U,k} \\ I_{L,max,k} & , \text{ if } V_{L,k} \geq V_{L,U,k} \end{cases} \quad (4.30)$$

where $V_{L,ref}$ and $I_{L,ref}$ are the reference load voltage and load current, $V_{L,L}$ and $V_{L,U}$ are the lower and upper limits of the load voltage, $I_{L,max}$ is the maximum load current that is the twice of the reference load current (i.e., $I_{L,max} = 2I_{L,ref}$), e is the deviation of the load voltage from the reference (i.e., $e = V_{L,ref} - V_L$), and K_P is the proportional gain.

In order to estimate the reference voltage and its lower and upper limits, a relationship between the voltage and the power output needs to be established. For this purpose, a generator power coefficient (C_{Pgen}) is used to normalize the power output with respect to the wind velocity as follows:

$$C_{Pgen} = \frac{P_{gen}}{\rho L R U^3} \quad (4.31)$$

Then, a map of the generator power coefficient with respect to the wind velocity, U , and the load voltage normalized by the wind velocity, V_L/U , is interpolated from data obtained from electromechanical simulations for a range of steady wind velocities (i.e., between 3 and 18 m/s). For visual convenience, the map is shown only for wind velocities up to 12 m/s in Figure 5.7.

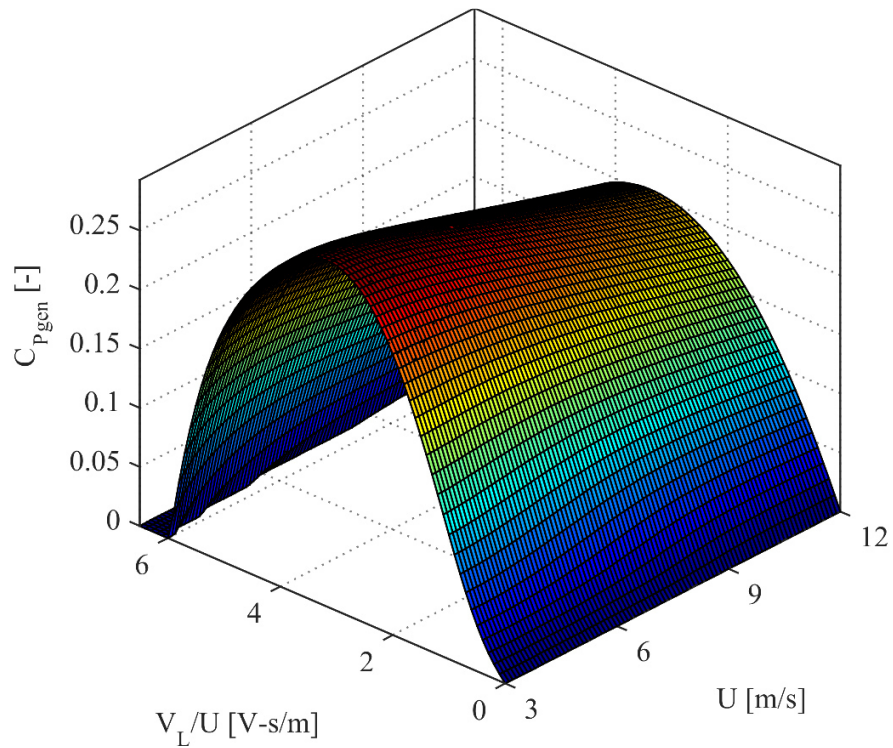


Figure 5.7: Generator power coefficient map interpolated from electromechanical simulation data.

The reference values of the power output, the load voltage, and the rotor velocity ($P_{gen,ref}$, $V_{L,ref}$, and ω_{ref} , respectively) for a given wind velocity are estimated from 6th order polynomial fits to the maximum power and the corresponding load voltage and rotor velocity data points, respectively (see Figure 5.8). The reference current value is calculated by dividing the reference power output by the reference load voltage, i.e., $I_{L,ref} = P_{gen,ref} / V_{L,ref}$.

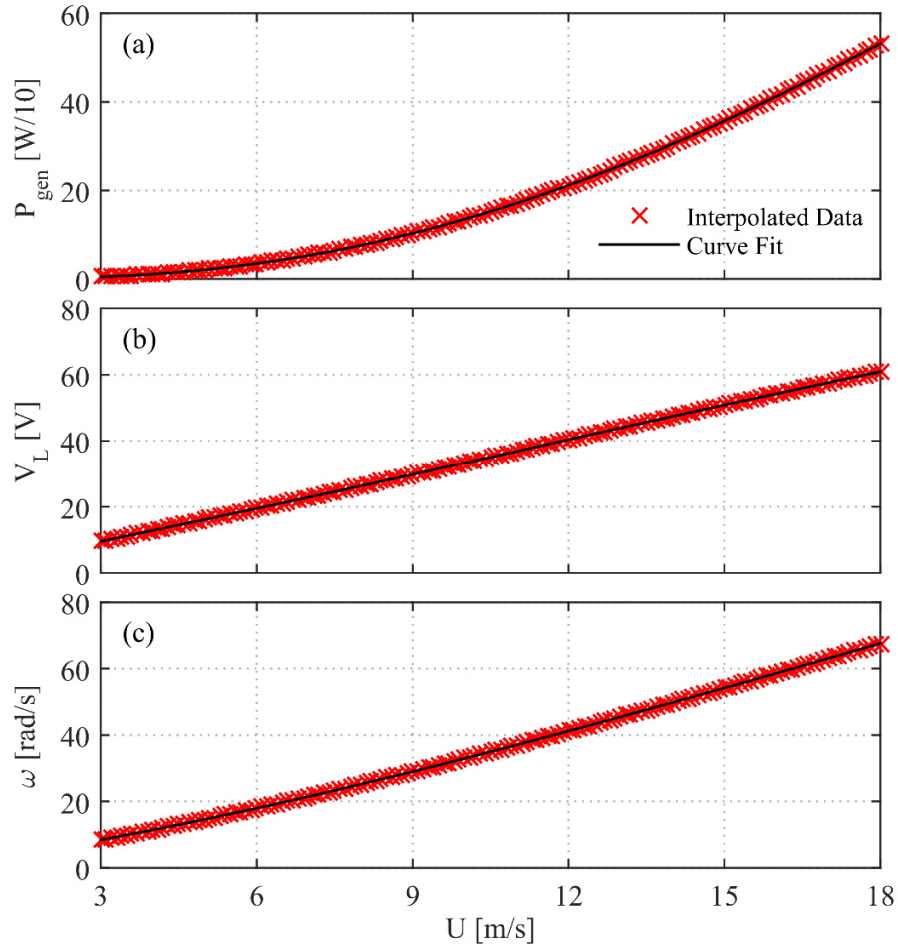


Figure 5.8: Reference power output (a), load voltage (b), and rotor velocity (c) data points and corresponding polynomial fits.

The lower and upper limits of the load voltage are obtained from the load voltage – generator power coefficient curve that is the 2D $V_L - C_{Pgen}$ section of the generator power coefficient map for a given wind velocity as follows. For a given level of the generator power coefficient, $\gamma C_{Pgen,ref}$, lower and upper limits of the load voltage are defined as the lower and upper bounds of the load voltage for which the generator power coefficient is greater than $\gamma C_{Pgen,ref}$, as shown in Figure 5.9.

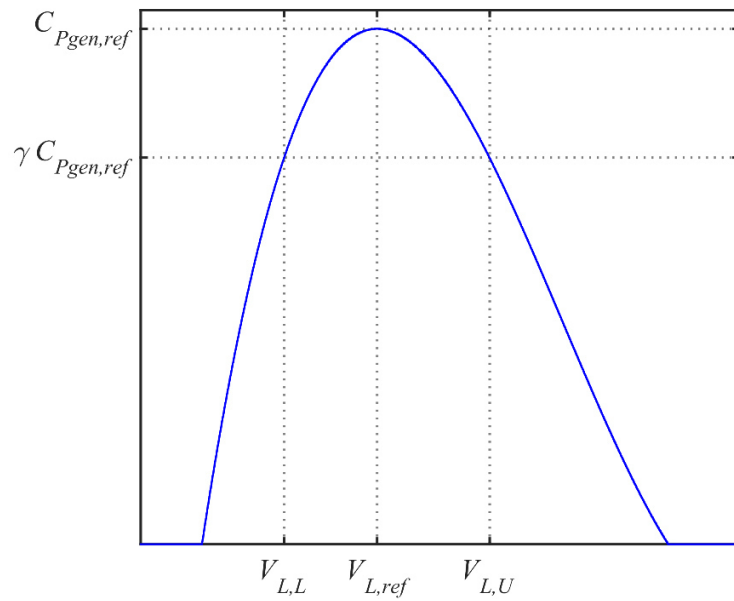


Figure 5.9: Estimation of the lower and upper load voltage limits.

The response of the MPC for a 60-second step wind is depicted in Figure 5.10. It is seen that the MPC for the electromechanical system is similar to the MPC for the simple dynamic system. However, Figure 5.10c shows that the current curve is not as sharp as the generator torque in Figure 4.7c. In other words, the ideal value for the level of the generator power coefficient, γ , seems to be lower for this case. Most likely, this is caused by the fact that the load voltage is dependent on the load current and sudden changes in the load current leads to adverse effects on the performance such as jitters.

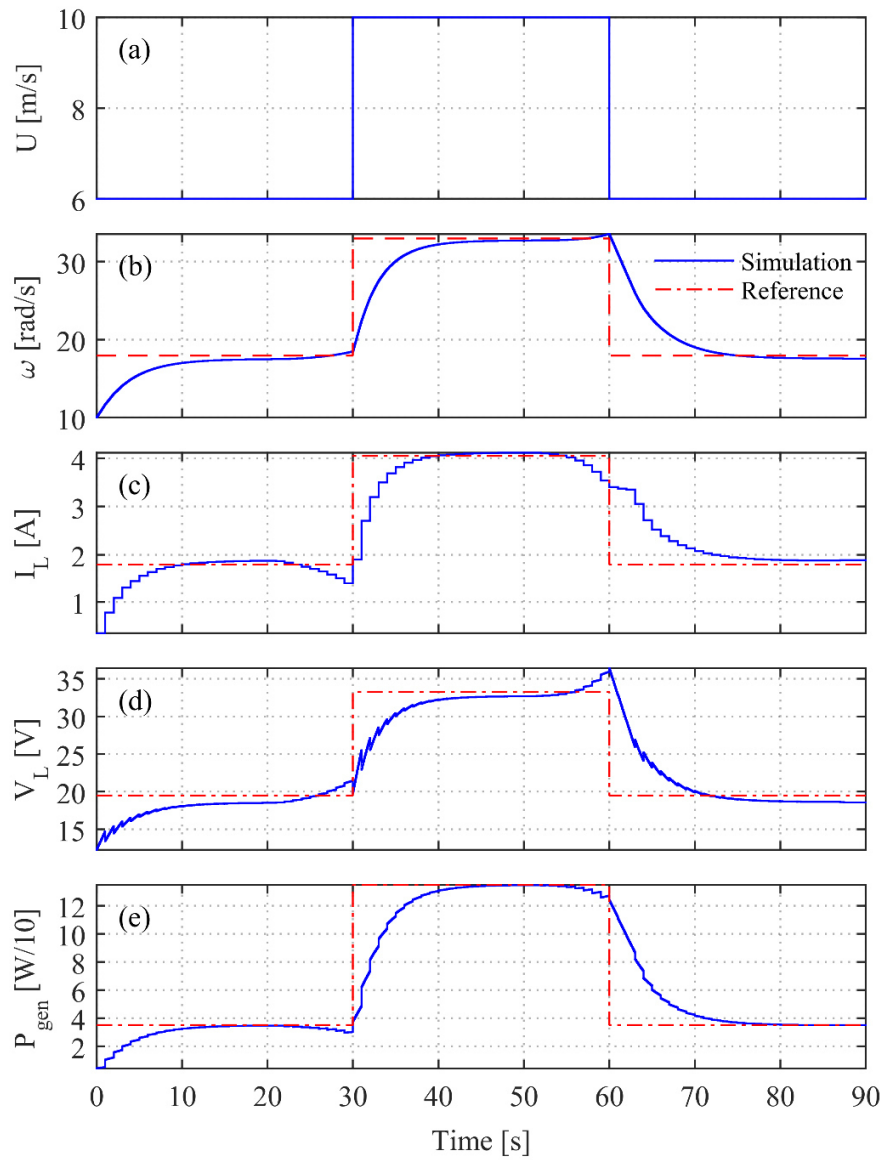


Figure 5.10: Rotor velocity (b), load current (c), load voltage (d), and power output (e) responses of the MPC for step wind (a).

For the selection of K_P and γ , a parametric study is conducted through 60-second electromechanical simulations for step wind. The energy efficiency, η_E , results are given in Table 5.2. It is observed that the efficiency enhances as the K_P increases, however $K_P > 1$ causes negative load current values, as in the SNC designed for the simple dynamic simulation; therefore, K_P is selected as 1. On the other hand, the optimal value for γ is obtained as 70%, which is lower than the other case as suggested by the MPC response. Still, the SNC algorithm operates at a sampling period of 0.1 s.

Table 5.2: Energy efficiency results of the parametric study for the tuning of SNC for HIL and electromechanical simulations.

γ [-] \ K_P [-]	0.25	0.50	0.75	1.00
25%	94.76%	95.75%	96.26%	96.51%
50%	95.07%	96.00%	96.43%	96.60%
60%	95.25%	96.12%	96.49%	96.63%
70%	95.55%	96.26%	96.56%	96.65%
75%	95.68%	96.35%	96.60%	96.65%
80%	95.75%	96.43%	96.62%	96.63%
90%	95.49%	94.92%	71.72%	71.27%

Chapter 6

RESULTS & DISCUSSION

6.1. Computational Fluid Dynamics Simulation Results

The coupled CFD/rotor dynamics model provides an environment to analyze the realistic transient behavior of the VAWT subject to the generator load manipulated by the control algorithm and the inertia of the rotor. Here, this environment is used to attain a relationship between the power coefficient, C_P , and the tip-speed ratio, λ , for different wind velocities, to understand the effects of the flow distribution around the rotor and the unsteady behavior of the power coefficient, and to observe the control performance for specified conditions.

6.1.1. Quasi-Steady Power Coefficient Curves

The coupled solution of the equation of motion of the rotor and the URANS equations allows to vary the generator load in simulations to obtain power coefficient values and the resulting $\lambda - C_P$ curves. In this procedure, K_L is set to zero at the beginning of the simulation to allow the rotor to start up from rest and to converge to a quasi-steady-state, as shown in Figure 3.4. Then, K_L is increased in steps for a sufficient duration during which the rotor velocity again converges to a quasi-steady-state. The values of the time-periods at the beginning and between each K_L increase and the step-size of K_L are prescribed depending on the wind velocity. For each K_L value, the final full revolution of quasi-steady-state is observed to estimate the mid-range values of the rotor velocity and the power output from which the tip-speed ratio and power coefficient values are obtained, respectively. The power coefficient

can be calculated from the power output, which equals to the mechanical power of the rotor, i.e., $P_{wind} = T_{wind} \omega$, owing to the ideal electromechanical conversion assumption:

$$C_P = \frac{P_{gen}}{\rho L R U^3} = \frac{K_L \omega^2}{\rho L R U^3} \quad (5.1)$$

Lastly, a $\lambda - C_P$ curve is composed by fitting cubic splines to the resulting data points.

Since only quasi-steady-state performance is considered in this analysis and computation time is substantially (e.g., 325 hours for $U = 6$ m/s) lower for low resolution simulations at the cost of slight (e.g., 6.5% for $U = 6$ m/s) accuracy loss in prediction of quasi-steady-state performance, low resolution simulations are performed to obtain C_P curves for different wind velocities and understand the relation between them. Figure 6.1 illustrates the C_P curve generation process through a low resolution simulation for $U = 10$ m/s. At the beginning of the simulation, K_L is set to zero for 50 seconds and then increased with a step-size of 0.1 up to 0.5, as shown in Figure 6.1a. At each increase of K_L , the kinetic energy of the rotor increases the power generation momentarily resulting in peaks in both the power output and the torque (see Figs. 6.1b and c). Afterwards, the rotor velocity and the power output converge rapidly to quasi-steady-state values from which the mid-range $\omega - P_{gen}$ values are obtained. Oscillations in the rotor velocity are observed for low rotation rates (i.e., for $\omega < 20$ rad/s), as shown in Figure 6.1b, and lead to torque ripples (Figure 6.1c) and power oscillations (Figure 6.1d).

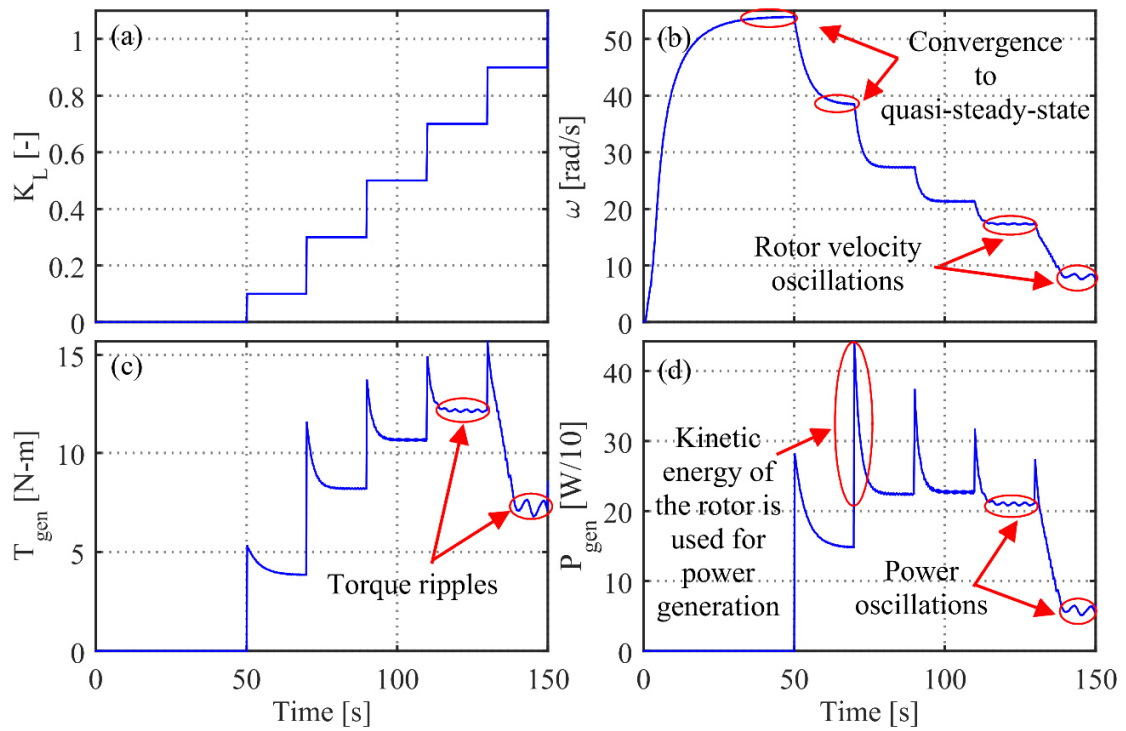


Figure 6.1: Variations of the load coefficient (a), rotor velocity (b), generator torque (c), and power output (d) for C_P curve generation process in a low resolution simulation for $U = 10$ m/s.

Carrying out the C_P curve generation procedure for steady wind velocities varying between 5 and 10 m/s leads to the $\lambda - C_P$ curves shown in Figure 6.2. It is clear that the $\lambda - C_P$ curves are almost invariant for a wide range of wind velocities, and one can suggest that they can be represented by a single curve. Hence, high resolution simulations are performed to produce a C_P curve for the wind velocity of 6 m/s which is a realistic value for small-scale applications.

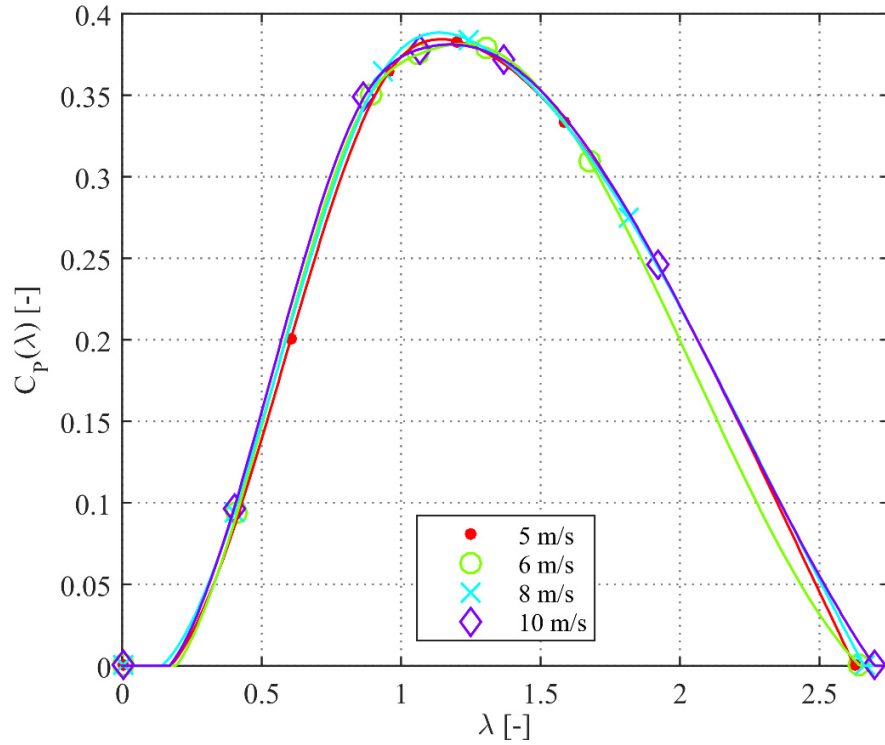


Figure 6.2: $\lambda - C_P$ curves obtained from low resolution simulations for steady wind velocities varying between 5 and 10 m/s.

A high resolution simulation requires more computational resources than low resolution simulations, therefore the C_P curve is generated for $U = 6$ m/s. First, a generator load-free simulation is run to start-up the rotor from rest until the rotor reaches the quasi-steady-state, and then simulations for different values of the load coefficient are initialized from quasi-steady-state of the load-torque-free simulation. The variation of the rotor velocity for load-torque-free simulation is shown in Figure 3.4; apparently, the rotor velocity converges to quasi-steady-state about the 60th second, so the simulations are initialized from the 61.5th second of this simulation.

Figure 6.3 demonstrates the rotor velocity, the generator torque and the power output responses for load coefficient values varying between 0.05 and 0.4 for a steady wind velocity of 6 m/s. Since the rotor velocity decays to almost zero for $K_L = 0.4$ (see Figure 6.3a), the load coefficient is not increased further. It is again noticed that there are visible oscillations in the rotor velocity for the last 10-second period of the simulation for $K_L = 0.4$ (Figure 6.3a), namely for low rates of the rotor velocity, which induce torque ripples (Figure 6.3b) and power oscillations (Figure 6.3c). As in the previous case, the high power output values at the beginning are because of the kinetic energy stored in the rotor.

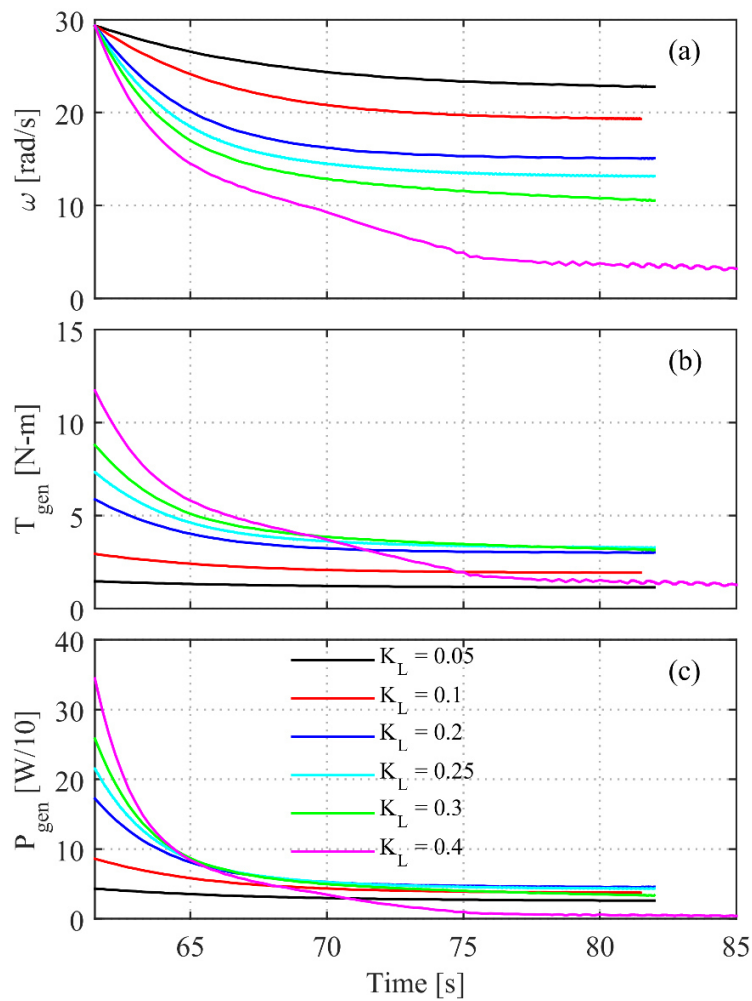


Figure 6.3: Variation of the rotor velocity (a), generator torque (b) and power output (c) throughout high resolution simulations for different values of the load coefficient for $U = 6$ m/s.

The mid-range values of the tip-speed ratio and the power coefficient for the final full revolution at quasi-steady-state of each simulation are given in Table 6.1. The maximum value of the power coefficient is obtained for $\lambda = 1.26$ for $K_L = 0.2$.

Table 6.1: Mid-range values of the tip-speed ratio and the power coefficient for different values of the load coefficient for $U = 6$ m/s.

K_L [-]	λ [-]	C_P [-]
0	2.41	0.000
0.05	1.90	0.1875
0.1	1.61	0.2777
0.2	1.26	0.3494
0.25	1.10	0.3280
0.3	0.88	0.2493
0.4	0.29	0.0344

Figure 6.4 depicts the resulting $\lambda - C_P$ curve obtained from high resolution simulations with the $\lambda - C_P$ curve obtained from a low resolution simulation. It is seen that the peak value of the power coefficient reduces to 0.349 from 0.382. On the other hand, the tip-speed ratio value corresponding to the peak point does not change considerably.

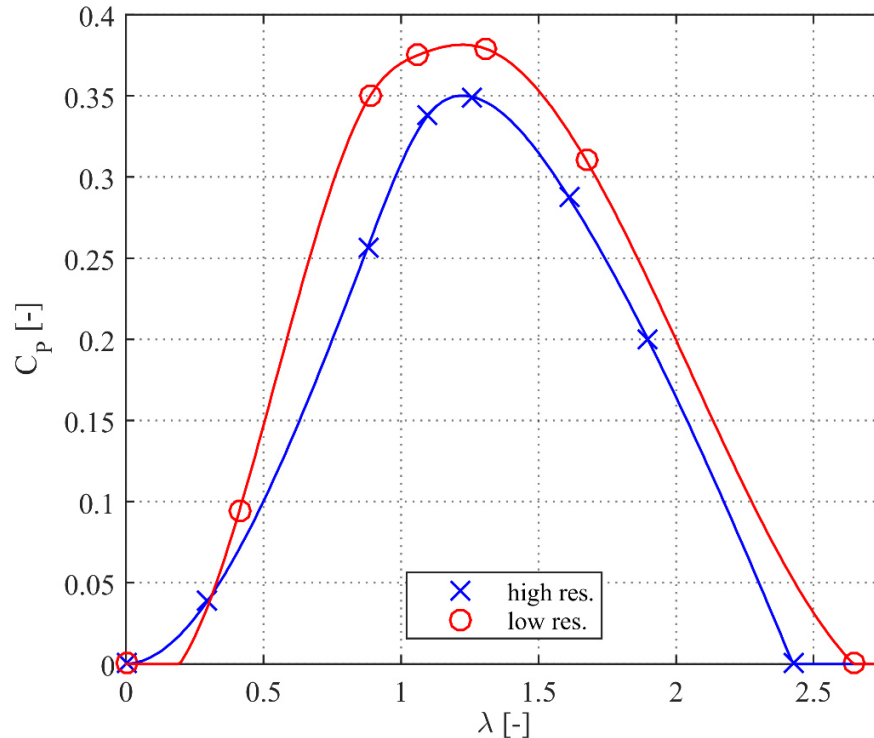


Figure 6.4: $\lambda - C_P$ curves obtained from low and high resolution simulations for $U = 6$ m/s.

6.1.2. Flow Fields & Shaft Effect

The most important difference between the flow fields at low and high rotation rates of the rotor is the penetration of vortices inside the rotor area. Figure 6.5 shows the turbulence kinetic energy, k , distributions in the flow as an evidence of the presence of vortex structures; turbulence kinetic energy is convected by the main flow as a scalar field, such as temperature and concentration species, and allows flow structures to be detected visually. Figure 6.5a shows the turbulence kinetic energy distribution at $t = 61.5$ s, when the tip-speed ratio is high (about 2.41), and Figure 6.5b at $t = 82.52$ s, when the tip-speed ratio is low (about 0.29), for a high resolution simulation for $U = 6$ m/s and $K_L = 0.4$. The quiescent region inside the rotor is free from vortices when the turbine rotates fast (Figure 6.5c), for $\lambda > 1.3$; whereas, when the turbine rotates slowly, for $\lambda < 1$, the vortex shed by the blade in the upwind region (due to the large angle of attack) impinges the blade in the downwind region and causes large oscillations in the wind torque (Figure 6.5d). Thus, it can be said that the presence of the shaft at the center of the rotor does not have a significant impact on the flow distribution for high rotor velocity rates of interest; in addition, it does not influence the variation of the rotor velocity either, as shown in Figure 3.4.

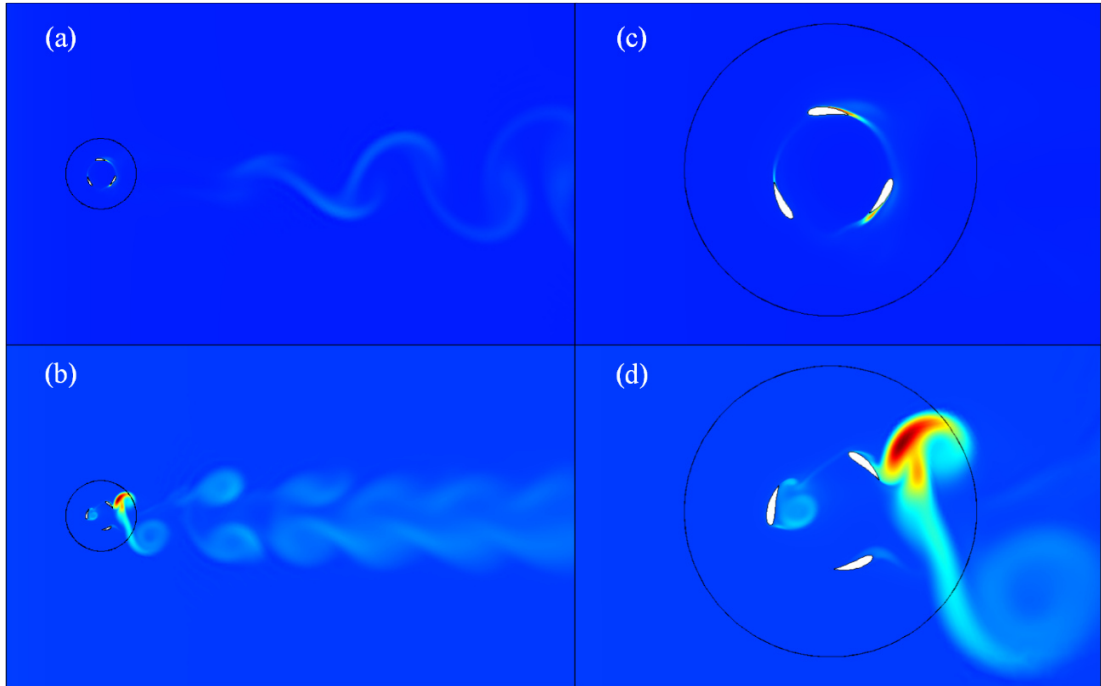


Figure 6.5: Turbulence kinetic energy surface plots at high (a) and low (b) tip-speed ratios along with the zoomed in rotor views in (c) and (d), respectively, from a high resolution simulation for $U = 6$ m/s.

6.1.3. Angle of Attack

The top view of the rotor with the net incident velocity vector acting on the blade 1 is illustrated in Figure 6.6, where θ is the azimuth angle, α_{local} is the angle of attack (i.e., the angle between the net incident flow velocity vector and the blade's orientation), and $U_{r,local}$ is the net incident velocity vector (induced by the wind flow and the motion of the blade) composing of the x - and y -components of the velocity, u and v . In this study, $U_{r,local}$ is obtained from the local velocity field effective at the tip of the blade rather than the geometric approach that assumes that incident velocity is the vector addition of the wind velocity and the linear velocity of the blade.

Consequently, the magnitude of the local incident velocity, $\|U_{r,local}\|$, and the angle of attack are calculated as follows:

$$\|U_{r,local}\| = \sqrt{u^2 + v^2} \quad (5.2)$$

$$\alpha_{local} = \tan^{-1} \left(\frac{v \cos(\theta - \beta) - u \sin(\theta - \beta)}{u \cos(\theta - \beta) + v \sin(\theta - \beta)} \right) \quad (5.3)$$

where β is the fixed pitch angle of the blades which is 5° (in clockwise direction) in this case. On the other hand, the geometrical approximations of the magnitude of the net incident velocity and the angle of attack ($\|U_{r,geometric}\|$ and $\alpha_{geometric}$) are calculated as follows [73]:

$$\|U_{r,geometric}\| = U \sqrt{\lambda^2 + 2\lambda \cos \theta + 1} \quad (5.4)$$

$$\alpha_{geometric} = \tan^{-1} \left(\frac{\sin(\theta - \beta)}{\lambda + \cos(\theta - \beta)} \right) \quad (5.5)$$

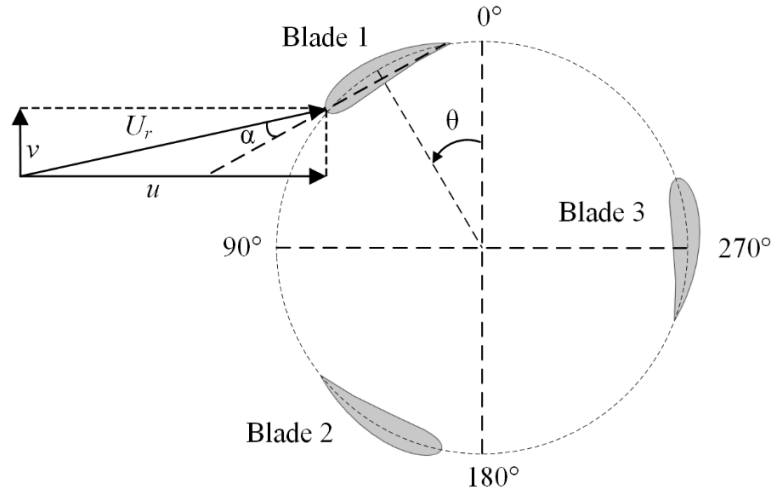


Figure 6.6: Top view of the rotor.

Figure 6.7 shows the variation of local and geometric incident velocities and angles of attack with respect to the angular position of the blade for a full revolution of the blade 1 for $U = 6$ m/s, i.e., $\lambda = 2.41$, in quasi-steady regime. Foremost, the net incident velocity and the angle of attack values calculated from the velocity field and the geometric approaches are significantly different from each other. $\|U_{r,geometric}\|$ has an ideal one-period sinusoidal pattern with the maximum at $\theta = 5^\circ$ and the minimum at $\theta = 185^\circ$ (5° shift is due to β), while $\|U_{r,local}\|$ fluctuates within a narrower range with the maximum at $\theta = 330^\circ$ and the minima at $\theta = 45^\circ$ and $\theta = 135^\circ$. On the other hand, $\alpha_{geometric}$ has a skewed one-period sinusoidal pattern with the maximum of 24.5° at $\theta = 120^\circ$ and the minimum of -24.5° at $\theta = 250^\circ$; whereas, α_{local} is sinusoidal only in the upwind region and reaches the peak of 39° at $\theta = 90^\circ$, the variation in the downwind region is relatively lower and reaches the bottom of -19.4° at $\theta = 330^\circ$.

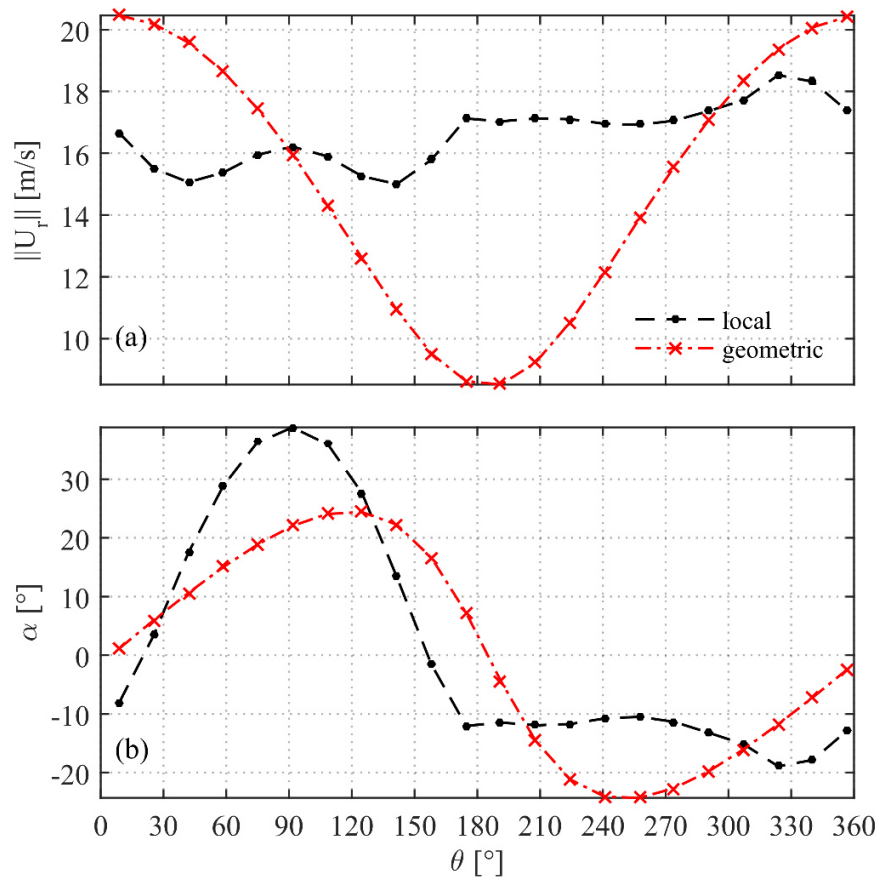


Figure 6.7: Net incident velocity magnitude (a) and the angle of attack (b) with respect to the angular position for the blade 1 for $U = 6$ m/s.

6.1.4. Blade Forces

The forces in \mathbf{x} - and \mathbf{y} - directions on the k^{th} blade ($F_{x,blade k}$ and $F_{y,blade k}$) induced by the flow field can be calculated by integrating the fluid stress over the surface of the blade:

$$F_{x,blade k} = \int_{S_k} \sigma_{xj} n_j dS \quad (5.6)$$

$$F_{y,blade k} = \int_{S_k} \sigma_{yj} n_j dS \quad (5.7)$$

Then, the forces acting on the whole rotor (F_x and F_y) are the total of the forces on each blade:

$$F_x = \sum_{k=1}^3 \int_{S_k} \sigma_{xj} n_j dS \quad (5.8)$$

$$F_y = \sum_{k=1}^3 \int_{S_k} \sigma_{yj} n_j dS \quad (5.9)$$

The total force in the \mathbf{x} -direction, F_x , can be deemed the thrust force on the rotor; hereby, a non-dimensional thrust coefficient, C_{thrust} , for the cross-sectional area of $A = 2RL$ can be derived, as follows:

$$C_{thrust} = \frac{F_x}{\frac{1}{2} \rho A U^2} \quad (5.10)$$

Figure 6.8 shows the thrust coefficient for a two-second period at quasi-steady-state of the load-torque-free simulation for $U = 6$ m/s. In order to understand the oscillatory behavior of the thrust coefficient, the surface plots of the \mathbf{x} -velocity are depicted with the arrows representing the velocity field at two azimuthal positions, where the minimum and the maximum of C_{thrust} occur, in Figure 6.9. According to Figs. 6.8 and 6.9b, when the angular position of a blade is close to 270° , the reduced intensity of \mathbf{x} -direction flow inside the rotor area leads to a very small thrust force. On the other hand, when a blade is positioned near 90° (Figure 6.9a) and faces the wind directly, the thrust force is maximum.

Since these configurations repeat three times in a full revolution for a three-bladed turbine, the frequency of C_{thrust} fluctuations triples in one revolution of the rotor, as seen in Figure 6.8. Moreover, Figs. 6.9a and b show that the flow is very weak inside the rotor area even in the absence of a blocking blade confirming that the shaft inside the rotor does not have a significant effect on simulation results.

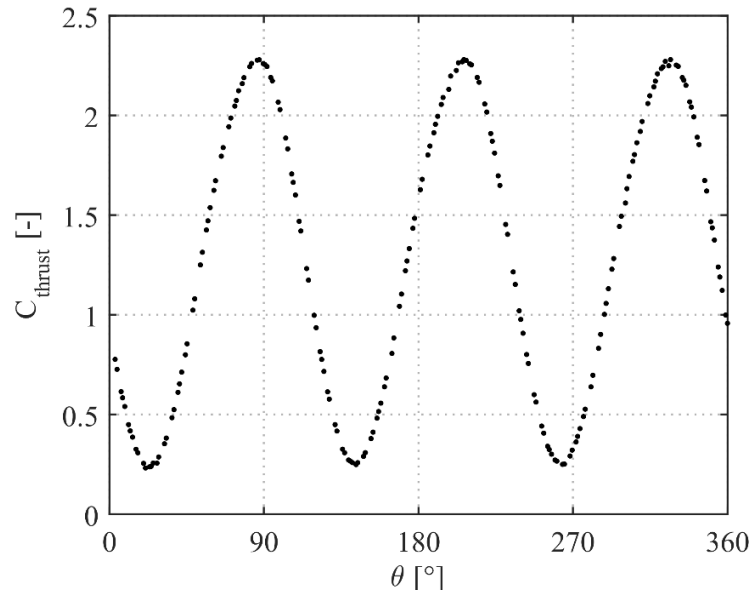


Figure 6.8: Thrust coefficient for a two-second period at quasi-steady-state of the load-torque-free simulation for $U = 6$ m/s with respect to azimuth angle.

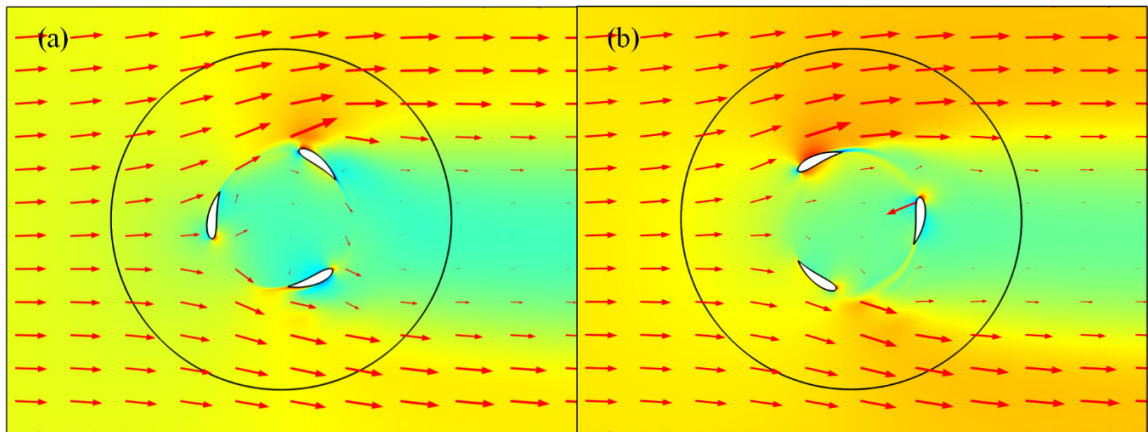


Figure 6.9: Surfaces of the x -velocity with arrows representing the velocity field at the minimum (a) and the maximum (b) values of the thrust coefficient.

The forces can be represented in polar coordinates as the tangential force, F_θ , which generates the torque, and the radial force, F_R , which is directed towards outside of the rotor along the radius. The forces in polar coordinates are obtained from the forces in Cartesian coordinates through the following transformation based on the azimuth angle, θ :

$$\begin{bmatrix} F_\theta \\ F_R \end{bmatrix} = \begin{bmatrix} -\cos \theta & -\sin \theta \\ -\sin \theta & \cos \theta \end{bmatrix} \begin{bmatrix} F_x \\ F_y \end{bmatrix} \quad (5.11)$$

Figure 6.10 shows the forces in Cartesian and polar coordinates for the blade 1 for a full revolution in quasi-steady regime of a simulation for $U = 6$ m/s and $K_L = 0.2$, i.e., $\lambda = 1.26$. It is seen that the magnitude of the radial force is much larger than the magnitude of the tangential force. The tangential force that generates the torque peaks around the azimuthal positions of 100° and 315° .

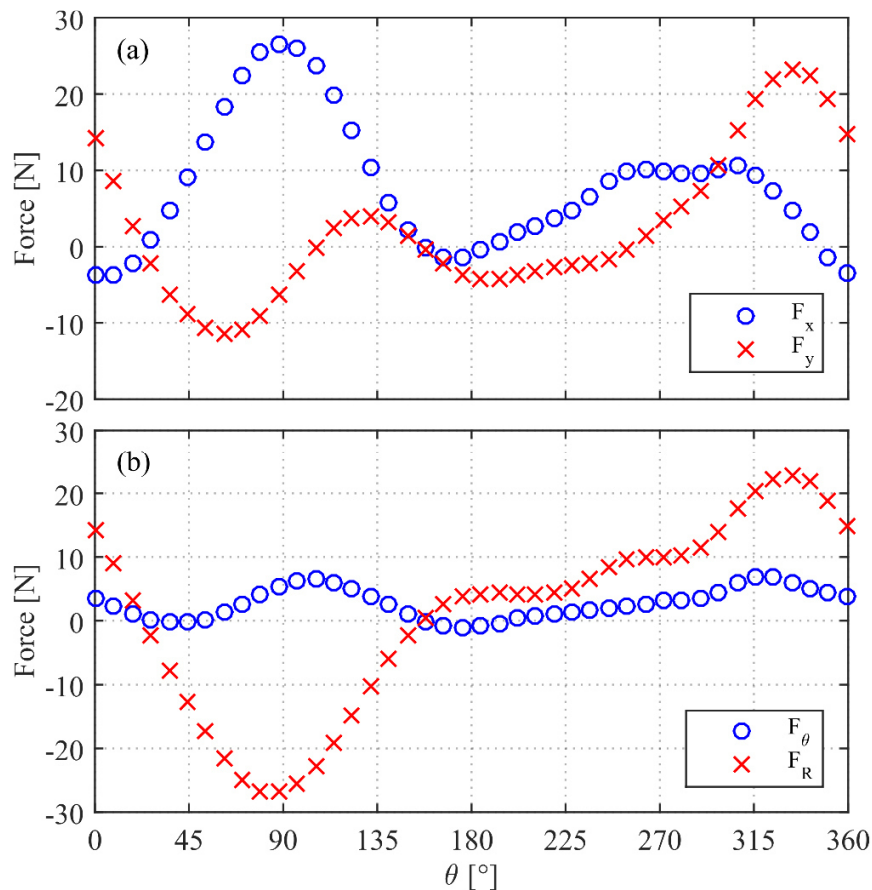


Figure 6.10: Forces in Cartesian (a) and polar coordinates (b) acting on the blade 1 throughout a full revolution in quasi-steady regime for $\lambda = 1.26$ with respect to azimuth angle.

6.1.5. Transient Response to Gusts

Coupled CFD model with rotor dynamics provides an environment to implement control designs manipulating the generator load so that the transient behavior of the system can be evaluated realistically including the inertial effects. Here, a proportional rotor velocity feedback power control law that manipulates the load coefficient is employed for variable-speed control:

$$K_L = K_{L,ref} - \frac{K_{L,ref}}{\omega_{ref}} K_P e \quad (5.12)$$

where e is the deviation of the rotor velocity from the reference, i.e., $e = \omega_{ref} - \omega$, and K_P is the proportional gain that is selected as 2.5. The reference values of the rotor velocity and the load coefficient (ω_{ref} and $K_{L,ref}$) are determined as given in (3.43) and (3.44) from the quasi-steady $\lambda - C_P$ curve that is obtained from high resolution simulations and shown in Figure 6.4, i.e., $C_{P,ref} = 0.3494$ and $\lambda_{ref} = 1.275$.

The control algorithm is implemented directly in the CFD model and tested for two different adaptations of the standard gust defined in (3.27), which are a small gust with $u_e = 2$ m/s and $T_g = 3$ s and a large gust with $u_e = 4$ m/s and $T_g = 10$ s; for both wind configurations, $U_0 = 6$ m/s and $t_0 = 21$ s. In order to reduce the computational effort, the simulations are initialized from the 18th second of the load-torque-free simulation for $U = 6$ m/s when the instantaneous rotor velocity (15.7 rad/s) is close to the reference rotor velocity (15.3 rad/s) that generates the maximum power.

For the small gust, the dynamic responses of the control variable, rotor velocity and the generator power are demonstrated in Figure 6.11. Figure 6.11a shows the transient wind velocity during the gust, and that the average velocity at the centerline of the rotor follows the gust profile at the inlet without a lag. The controller varies the load coefficient, K_L , inversely with the variation in the wind velocity (Figure 6.11b), as the wind velocity decreases (increases) the K_L increases (decreases) to decrease (increase) the angular velocity of the rotor. As a result, the angular velocity of the rotor tracks the reference ω_{ref} with a delay due to the inertial response of the rotor as shown in Figure 6.11c. During the gust (i.e., $21 \leq$

$t \leq 24$ s), 94.86% of the available energy is harvested according to the instantaneous power generation, P_{gen} , as shown in Figure 6.11d.

In Figure 6.11e, oscillations in the wind and generator torques are shown with respect to the small gust. First, the frequency of oscillations in the wind torque and the power coefficient is exactly 3ω consistently with the three-bladed structure of the rotor. Second, oscillations in the generator torque has a very small amplitude, about .02 N-m, compared to the amplitude of the oscillations in the wind torque, about 2 N-m, in the quasi-steady-state at the end of the gust due to the rotor's inertia. Largest amplitude of the torque oscillations is observed at the peak wind velocity, about 2.8 N-m in the wind torque but not detectable in the generator torque as the variation in the average value of the T_{gen} is more significant. Rotor's inertia filters the unwanted torque ripples by the virtue of the first-order dynamics of the rotor. Further studies would be useful to investigate the role of rotor's inertia and the controller design in the suppression of torque ripples and the maximization of the energy output. Typical CFD studies in literature are based on constant angular velocity of the rotor, and the power that is obtained from the wind torque is assumed to be same as the generator power. Here, the angular velocity is calculated from the rotor's equation of motion. Thus, the dynamic response of the rotor velocity is taken into account more realistically. Moreover, the generator and wind torques differ especially during wind transients subject to the conservation of angular momentum of the rotor. The power coefficient oscillates in-sync with the T_{wind} during the gust as shown in Figure 6.11c. In the quasi-steady part of the gust, C_P oscillates between -0.03 and 0.64 exceeding the Betz limit (i.e., 0.593) temporarily due to the energy storage in the rotor, which acts as a temporary buffer that stores the kinetic energy like a flywheel in short durations. The amplitude of the oscillations becomes larger (smaller) as the tip-speed ratio increases (decreases) respectively, as anticipated from (3.4). When the wind velocity reaches its peak value, 7.5 m/s, the power coefficient varies between 0.15 and 0.5, with an amplitude almost the half as much as the one during the quasi-steady-state for $U = 6$ m/s, exactly proportional to the cubic ratio of the velocities, i.e., $6^3/7.5^3 \approx 0.5$. The average value of the C_P per revolution does not vary significantly and alters between 0.29 and 0.36 with an average value of 0.35, and it reaches the minimum after the peak of the gust during the second bottom of the wind velocity.

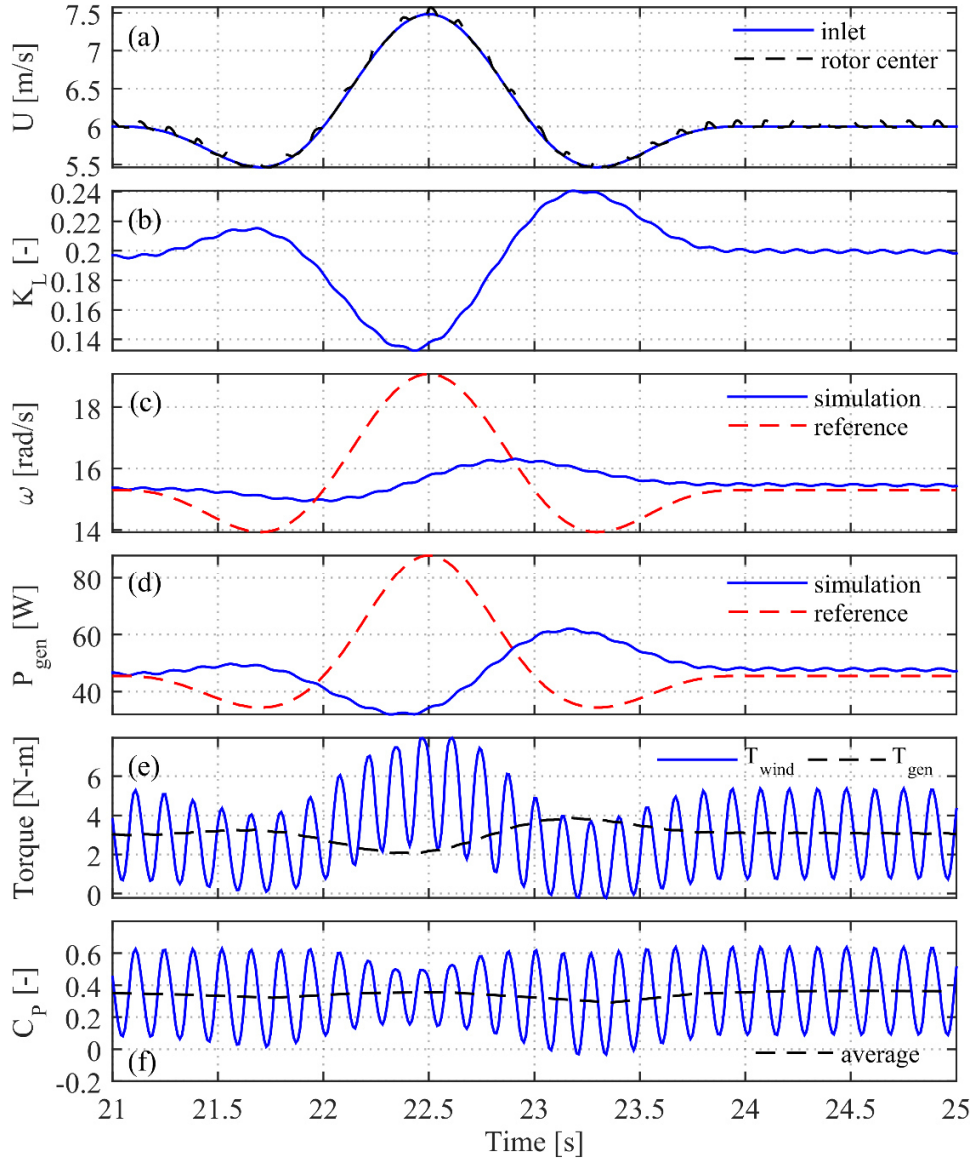


Figure 6.11: Small wind gust profile (a); dynamic responses of the load coefficient (b), rotor velocity (c), generator power (d), wind and generator torques (e), and the power coefficient (f).

Figure 6.12 shows the variation of the local and geometric values of $\|U_r\|$ and α , which are given by (5.2)-(5.5), with respect to the angular position of the blade 1 for $22 \leq t \leq 25$ s in the small gust simulation (see Figure 6.11a). For each revolution, $\|U_{r,local}\|$ and α_{local} fluctuate dramatically even for a gust with a small amplitude, whereas $\|U_{r,geometric}\|$ and $\alpha_{geometric}$ appears to remain almost unaltered. This is due to that the actual velocity field on the blade varies substantially with the wind transients. Especially, the peaks of the net

incident velocity in the upwind and downwind regions are significantly underestimated by the geometric approach. Additionally, the local extrema of $\|U_{r,local}\|$ and α_{local} occur at slightly lower ($\sim 15^\circ$) angular positions as the wind velocity increases, or the tip-speed ratio decreases, and they are correlated in contrast to $\|U_{r,geometric}\|$ and $\alpha_{geometric}$. This result also demonstrates that the interaction between the wind and the local flow due to blades motion is extremely strong in VAWTs unlike in HAWTs.

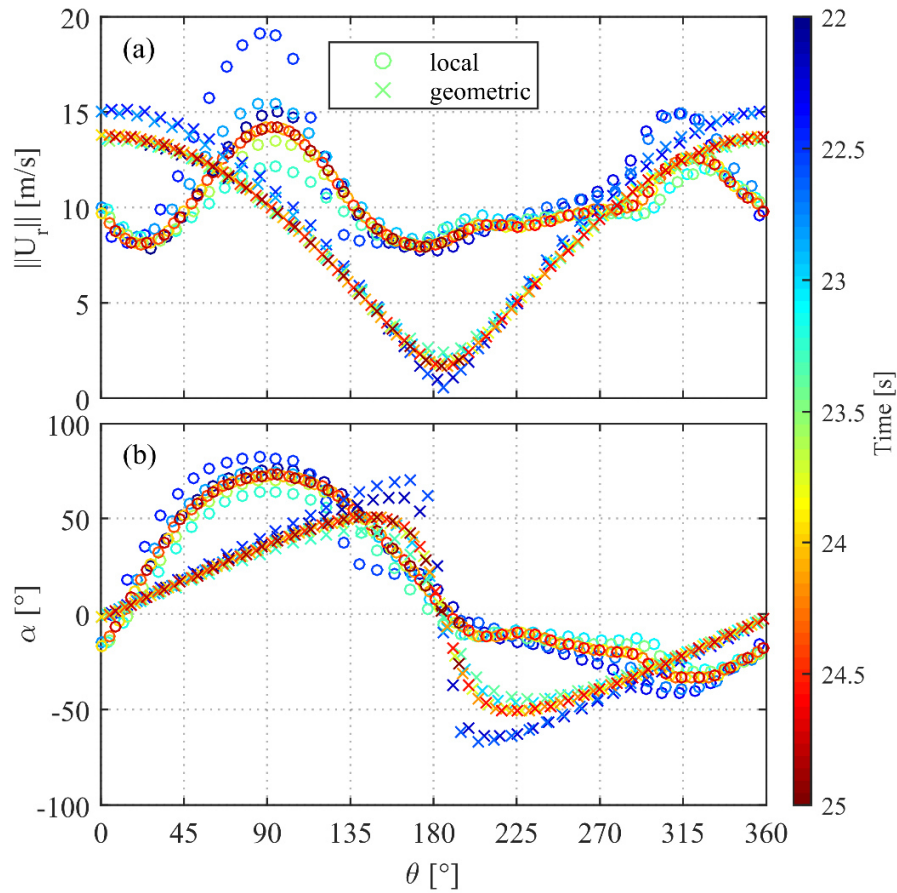


Figure 6.12: Local and geometric estimations of the net incident velocity (a) and the angle of attack (b) vs the angular position for the blade 1 during the small gust.

The dynamic responses of the load coefficient, rotor velocity and generator power are illustrated in Figure 6.13 for a large gust (i.e., $u_e = 4$ m/s and $T_g = 10$ s, see Figure 6.13a). The controller adjusts the load coefficient in Figure 6.13b such that rotor velocity tracks the reference optimal value with negligible error (about 2×10^{-3} rad/s) when the wind velocity is constant before and sufficiently after the gust, but with delay during the gust due to the inertia. Time difference between the peaks of the angular velocity of the rotor and its

reference value, which is caused by the combined effect of the inertia and the control algorithm, is about 1 second. As a result, the VAWT harvests 94.95% of the available energy throughout the gust, i.e., for $21 \leq t \leq 31$ s.

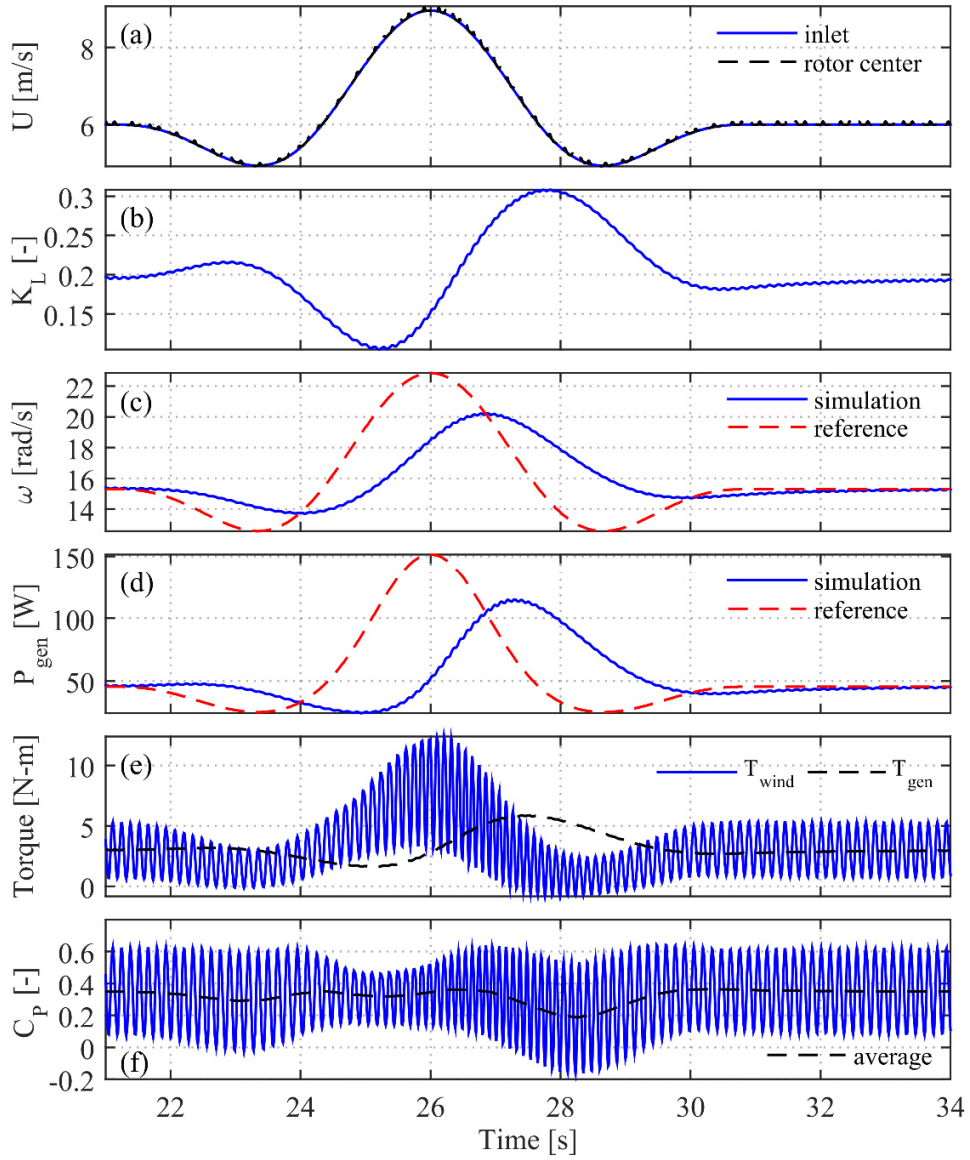


Figure 6.13: Large wind gust profile (a); dynamic responses of the load coefficient (b), rotor velocity (c), generator power (d), wind and generator torques (e), and the power coefficient (f).

Amplitude of the oscillations in the wind torque becomes the largest during the peak of the gust, and the smallest during the troughs as shown in Figure 6.13e. Especially during the second trough after the gust peak, transient values of the wind torque becomes negative as the rotation rate of the turbine becomes larger than the reference optimal value corresponding to the instantaneous wind velocity, although the average value of the wind torque is still positive. Moreover, similar to the small gust case, the amplitude of the oscillations in the generator torque is about the 1/100th of the amplitude of the oscillations in the wind torque. The power coefficient oscillates between 0.15 and 0.47 during the peak of the transient and between -0.14 and 0.53 during the trough after the peak of the gust as shown in Figure 6.13f. Average values of the C_P vary between 0.19 and 0.36 which take place in the second bottom of the wind velocity and immediately after the peak.

Figure 6.14 shows the radial and tangential forces acting on the blade 1 and the torque generated by the blade 1 vs the azimuth angle during the large gust. The forces and the torque for the rotor is the superposition of the forces and the torque for the blade 1 with 120° shifts due to the periodicity of the three-straight-bladed structure. The radial force, which does not do any work, has a wide range, and its magnitude reaches above 50 N (Figure 6.14a). The tangential force that generates the torque of the blade, F_θ , has a narrower range but still very sensitive to transients, see Figure 6.14b. The torque generated by the blade, $T_{blade\ k}$, is used to calculate the power coefficient of the blade, $C_{P,blade\ k}$, as below:

$$C_{P,blade\ k} = \frac{T_{blade\ k} \omega}{\rho L R U^3} \quad (5.13)$$

The correlation between the tangential force and the torque of the blade is obvious, as shown in Figs. 6.14b and c; however, the magnitude of the torque is not equal to $|F_\theta R|$, as one can expect, because the point on the blade where the resulting force is acting on is not at the same distance to the rotor center throughout a revolution. As a result, there are observable differences between the characteristics of the tangential force and the torque generated by the blade. Nevertheless, both have maxima around $\theta = 90^\circ$, minima around $\theta = 180^\circ$ and local maxima around $\theta = 315^\circ$, and the displacements of these extrema points throughout transients are consistent with each other.

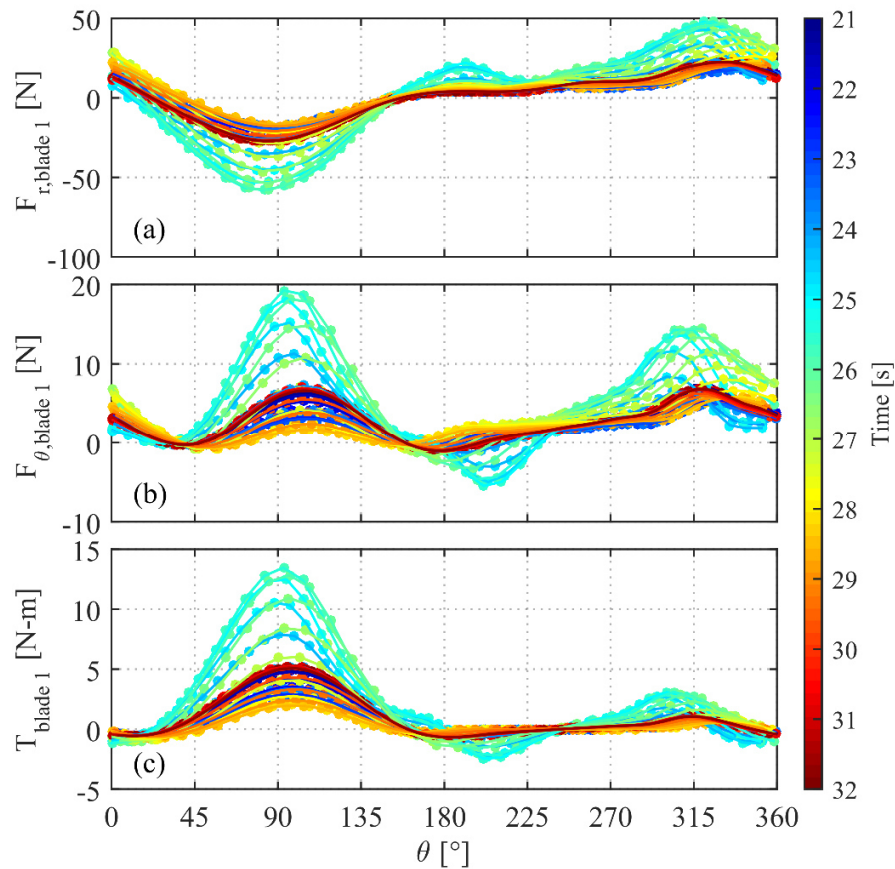


Figure 6.14: Radial (a) and tangential (b) forces acting on the blade 1 and the torque generated by the blade 1 during the large gust.

6.1.6. Unsteady Power Coefficient

In order to gain further insight into the unsteady behavior of the C_P , the characteristics of the C_P is investigated in more detail. The variation of the power coefficient with respect to the azimuth angle is demonstrated in Figure 6.15 for $21 \leq t \leq 32$ s of the large gust simulation, which spans a larger tip-speed ratio range than the small gust simulation. The three-period sinusoidal pattern in a revolution is due to the periodicity of the three-straight-bladed structure. However, the average, amplitude and phase of the oscillations vary dramatically for each revolution.

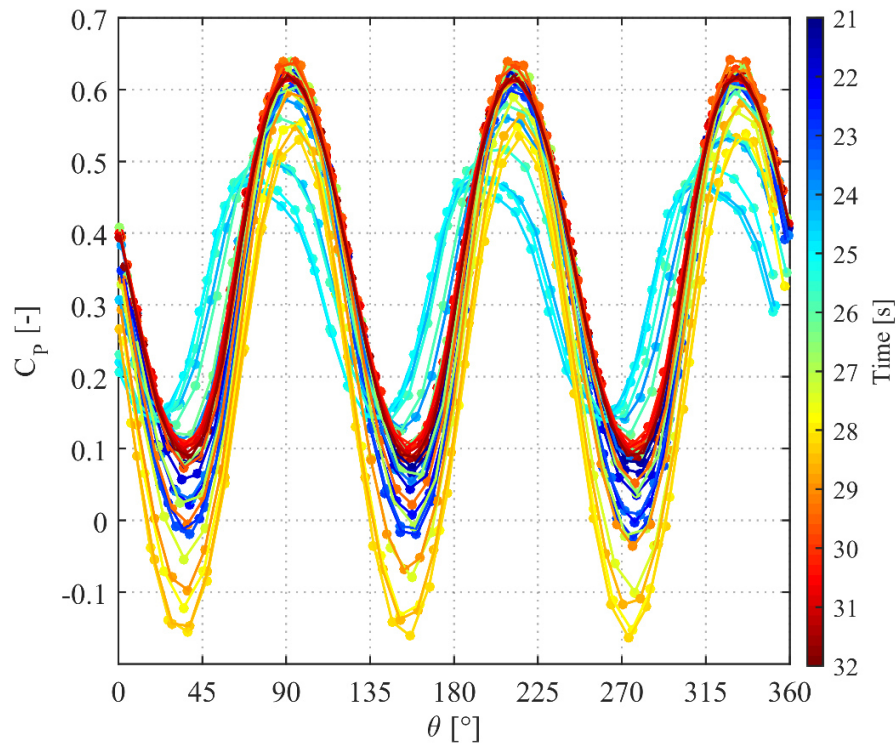


Figure 6.15: Unsteady C_P vs θ during the large gust.

Figure 6.16 shows the oscillations of the C_P , $C_{P,oscillation}$, which is obtained by subtracting the average value of the C_P per revolution from the instantaneous C_P , and the amplitude of the C_P oscillations, $C_{P,amplitude}$, with respect to the λ . Figure 6.16a shows that the amplitude of the C_P oscillations increases with the tip-speed ratio as reported in literature for similar turbines. Furthermore, Figure 6.16b shows that hysteresis loops form as the tip-speed ratio varies along with the variation of the wind velocity and the rotor velocity; in other words, the relationship between the C_P amplitude and the tip-speed ratio is dependent not only on the tip-speed ratio but also on the dynamics of the rotor and the wind.

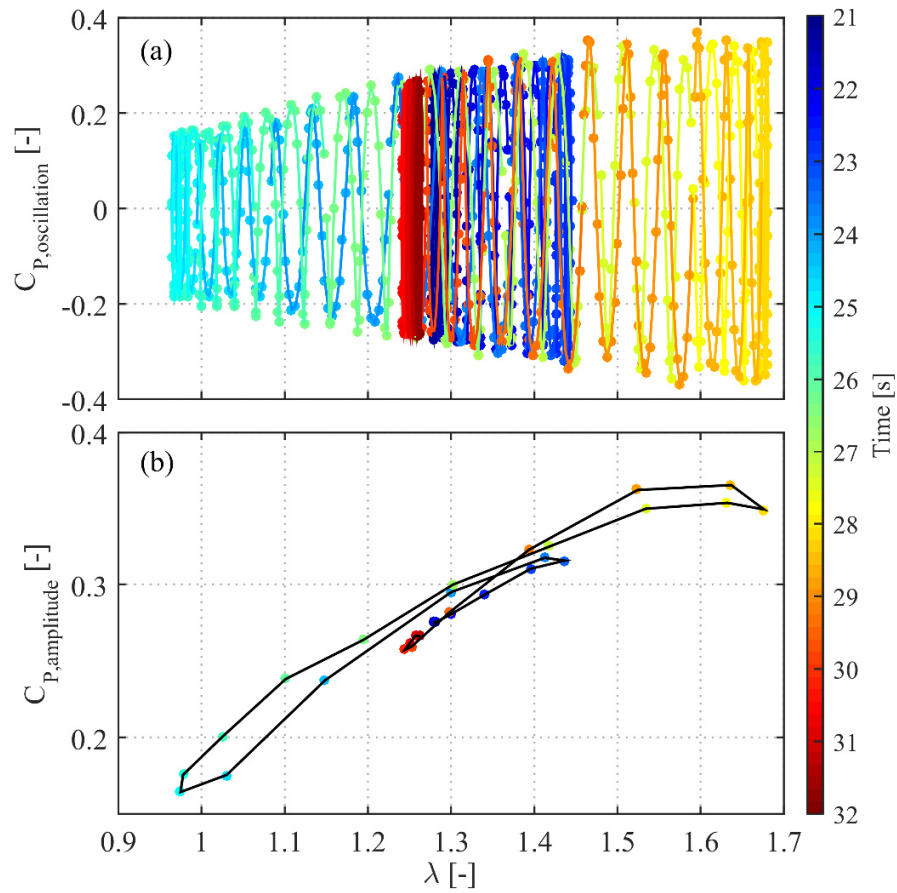


Figure 6.16: Variation of the C_P oscillations and the amplitude of the oscillations with respect to the tip-speed ratio for the large gust.

In Figure 6.17, instantaneous and average values of the C_P for unsteady and steady winds are shown. First, the average values of C_P during the transient wind (represented by cross symbols in Figure 6.17) are slightly shifted from the steady-state values of the C_P (represented by squares). Second, extreme values of the unsteady C_P for the transient wind follow the trend for the average values. As the tip-speed ratio increases, the extreme values of the instantaneous C_P for the transient wind fall below the extreme values of the C_P for the steady wind, and vice versa.

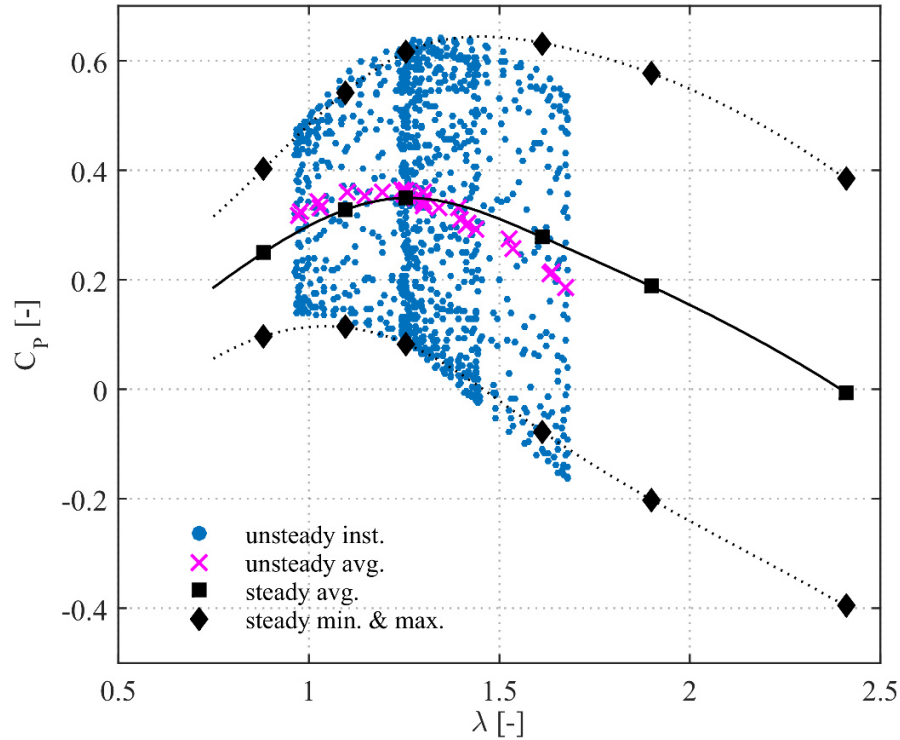


Figure 6.17: Unsteady instantaneous and unsteady average per revolution $\lambda - C_P$ values during the large gust, and steady average, minimum and maximum per revolution $\lambda - C_P$ values.

Figure 6.18 shows the plots of average values of the C_P for steady and unsteady winds. A polynomial curve-fit is applied to the C_P values from the transient wind conditions and shown in the figure. First, $\lambda - C_P$ pairs from the small and large gusts are very close to each other. Second, there is a discernible difference between the C_P curves as the peaks occur at different tip-speed ratio values, 1.17 vs 1.27, and the peak C_P value for the transient wind is slightly higher than the steady wind, 0.362 vs 0.349. It is also important to emphasize that the peak value of the average C_P during the gust coincides with the instant when the rotor angular velocity is smaller than its reference value. Instantaneous C_P for one blade and for the whole rotor are plotted with respect to the angular position of the rotor for three quasi-steady revolutions for different λ values, which are the minimum and maximum tip-speed ratios during the gust and the tip-speed ratio at steady-state (see Figure 6.19a), in Figure 6.19. The C_P for the rotor is the superposition of the $C_{P,blade\ 1}$ with 120° shifts due to the periodicity of the three-straight-bladed structure. The mean and amplitude values of the rotor's C_P vary dramatically for each revolution. Variation of the $C_{P,blade\ 1}$ with respect to the azimuth angle

shows that $C_{P,blade\ 1}$ becomes negative for small angles $\theta < \{18^\circ, 28^\circ, 47^\circ\}$ for $\lambda = \{0.96, 1.27, 1.68\}$ and is close to zero for about $\theta > 150^\circ$ for all λ values. Only at $\theta \approx 90^\circ$, the power coefficient reaches about 0.6. Wekesa et al. [37] obtained a similar distribution for the blade torque, which is expressed in terms of the power coefficient of the blade based on the relationship given by (3.4). For $\lambda = 1.27$, the angular velocity of the rotor is close to its reference value that maximizes the rotor's power, hence, the C_P for that λ is higher than the others for most θ values. For $\lambda = 1.68$, the angular velocity of the rotor is higher than the reference value, which takes place at $t = 28.5$ s (see Figs. 6.13c and 6.19a), and the average C_P values for the rotor and the single blade are lower than the ones for the other tip-speed ratios. Moreover, the cumulative C_P becomes negative for $\{15^\circ, 135^\circ, 255^\circ\} < \theta < \{53^\circ, 173^\circ, 293^\circ\}$, with an average value of 0.18, which is 30% lower than the steady-state value of 0.25 for the same λ .

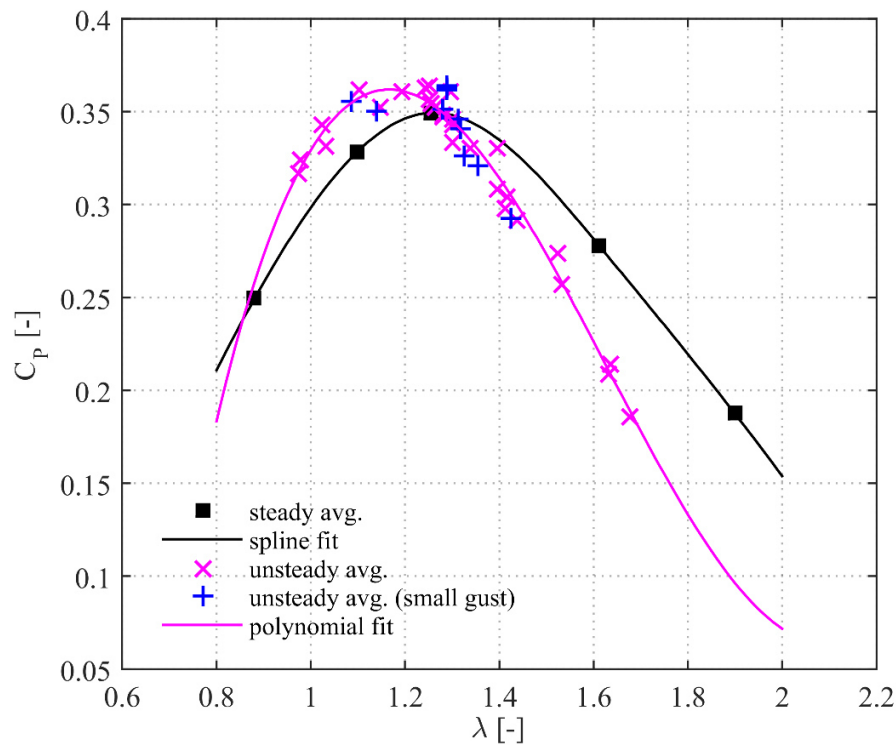


Figure 6.18: Steady and unsteady average per revolution $\lambda - C_P$ values and resulting $\lambda - C_P$ curves.

As shown in Figure 6.18, the average unsteady C_P values are lower than the average steady values for $\lambda > \lambda_{ref} = 1.275$. On the other hand, there is a slight improvement in the average C_P for the transient wind compared to one for the steady wind for the same λ for $\lambda < \lambda_{ref} = 1.275$; for instance, for $\lambda = 0.96$, the average value of the unsteady C_P is 0.32, which is higher than the steady one, i.e., 0.29. In this case, the angular velocity of the rotor is smaller than the reference value, or the wind velocity is larger than the value that corresponds to the angular velocity in steady condition. For this case, the oscillations of the rotor C_P have a smaller amplitude than for the other tip-speed ratios. In fact, from Figure 6.17, it is clear that the magnitude of the C_P oscillations decreases as the tip-speed ratio decreases. Furthermore, the minimum of the transient wind C_P is slightly above the minimum of the steady wind C_P .

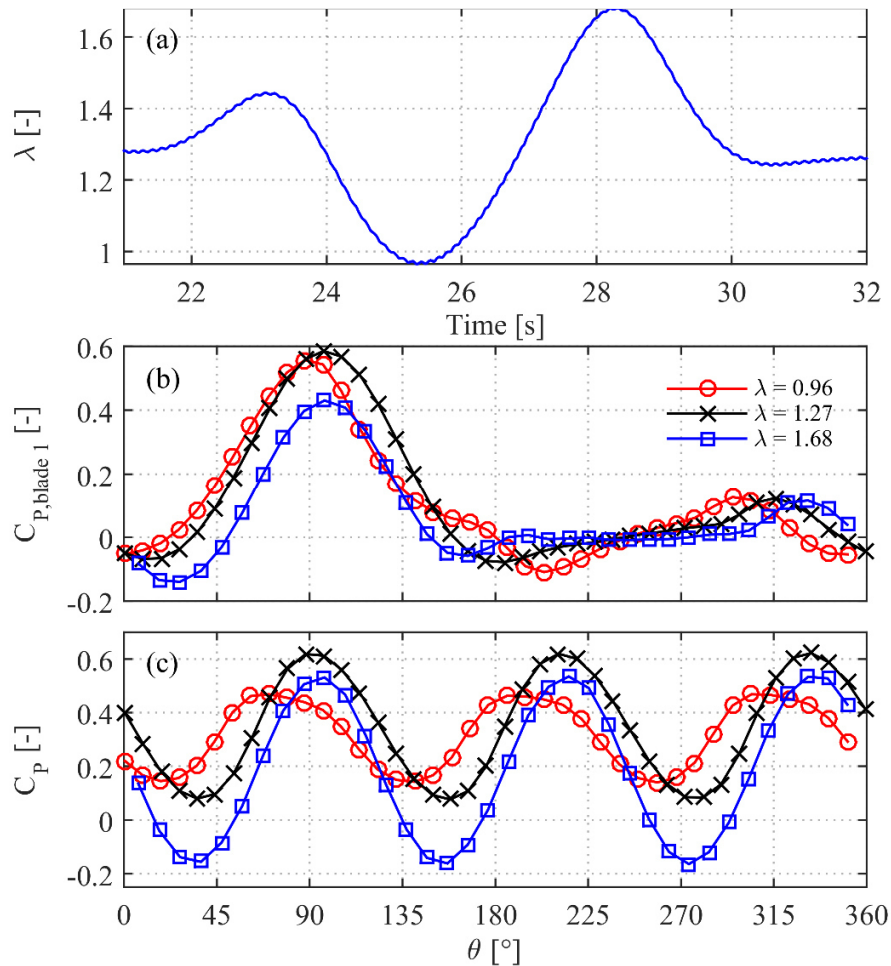


Figure 6.19: Variation of λ with respect to time (a) and unsteady C_P for the blade 1 (b) and cumulative C_P with respect to azimuth angle (c) at three revolutions with different λ values at transient-state.

In Figure 6.20, the angle of attack and C_P for each blade and the cumulative C_P are plotted with respect to the azimuth angle for one revolution for steady wind (i.e., for $39.18 \leq t \leq 39.59$ s and $\lambda = 1.275$). C_P values tend to follow the same trend with α_{local} rather than $\alpha_{geometric}$. In addition, the geometric approach underestimates the maximum angle of attack ($\sim 20^\circ$) and overestimates the magnitude of the minimum angle of attack ($\sim 15^\circ$). According to the angle of attack from the velocity field in the upwind region, α_{local} and C_P for each blade have peaks of 72.5° and 0.585 at the angular positions of 93° and 98° , respectively; while in the downwind region, the minimum value of α_{local} is -33.4° and the C_P makes a smaller peak of 0.124 at the angular positions of 323° and 315° , respectively. The resulting cumulative C_P has a minimum value of 0.078 at the azimuth angles of 37° , 157° and 277° and peaks of 0.624 at the azimuth angles of 92° , 212° and 332° , with an average value of 0.349 for the complete revolution.

Figure 6.21 shows the $\alpha_{local} - C_P$ relationship for the blade 1 at three quasi-steady revolutions at different mean λ values involving the minimum and maximum tip-speed ratios during the gust and the tip-speed ratio at steady-state. It is seen that the $\alpha_{local} - C_P$ curves make hysteresis loops in counterclockwise direction. As λ increases, the $\alpha_{local} - C_P$ curve becomes narrower, and the C_P peaks at the both regions develop at larger magnitudes of α_{local} . On the other hand, the value of C_P does not change considerably for the smaller C_P peak corresponding to the downwind region, whereas the value changes as well for the larger peak occurring at the upwind region. Compared to the other cases, for the smallest λ corresponding to the highest wind velocity, the declination of C_P is lower until a steep descent at around $\alpha_{local} = 25^\circ$ as the blade rotates from the upwind to downwind region.

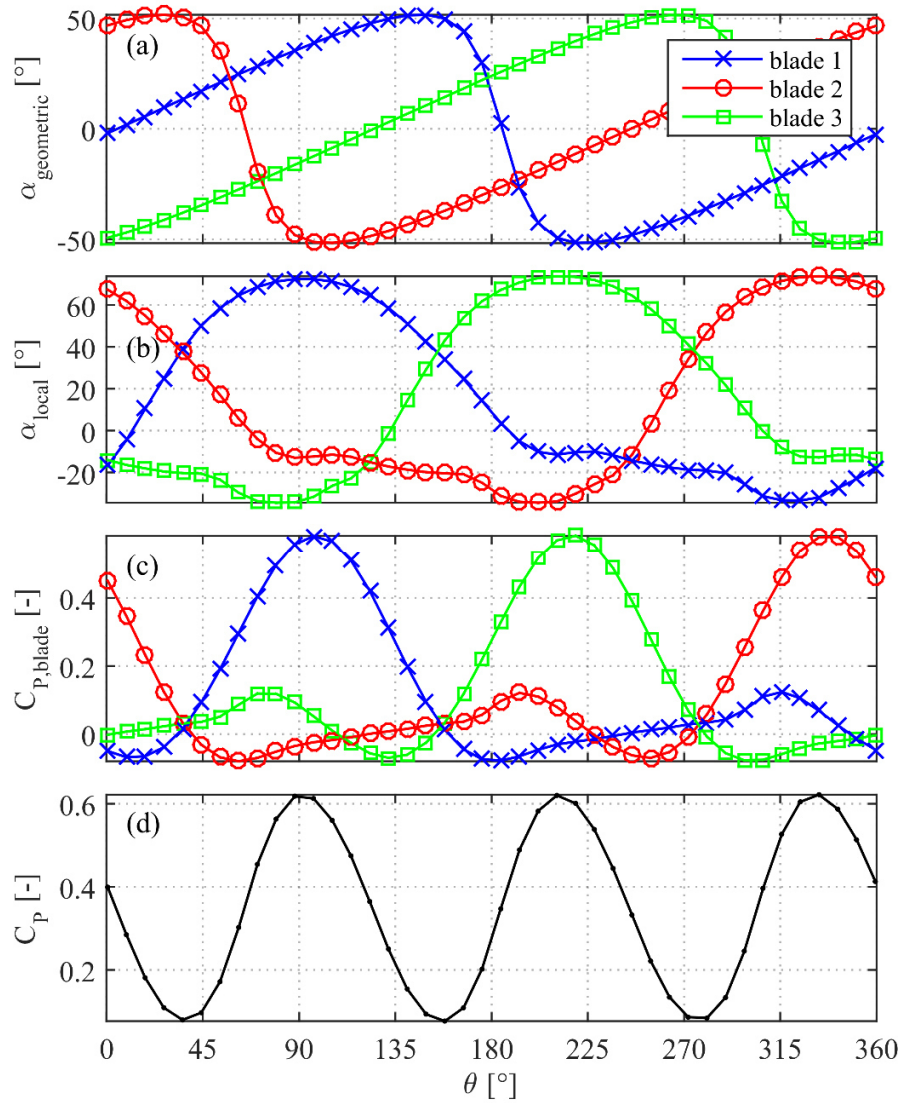


Figure 6.20: Variation of $\alpha_{\text{geometric}}$ (a), α_{local} (b) and C_P per blade (c) and the variation of cumulative C_P (d) with azimuth angle for one revolution at steady-state.

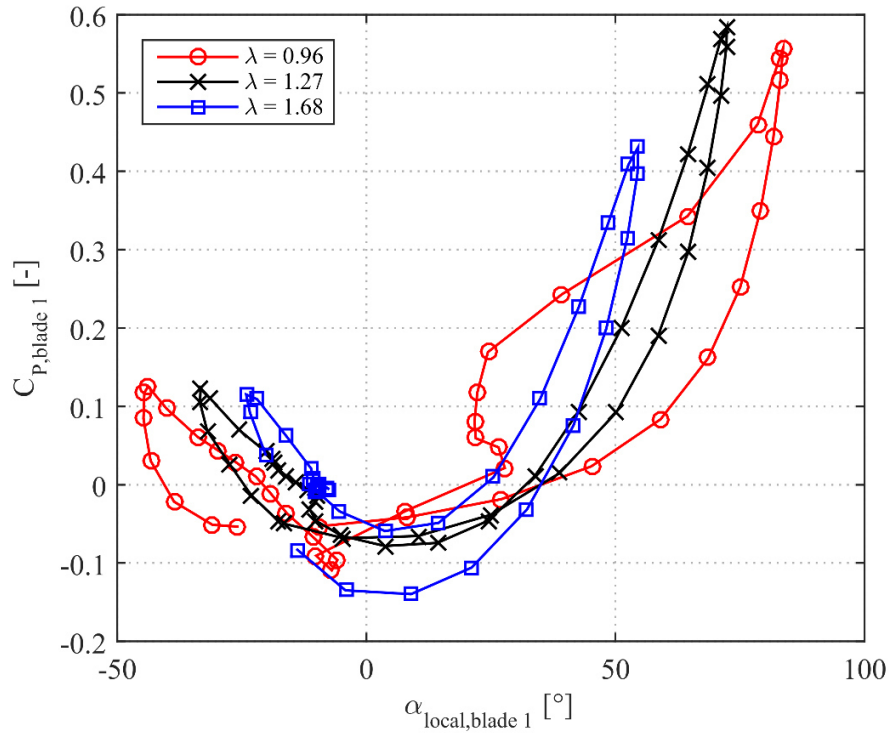


Figure 6.21: Variation of C_P with α_{local} for the blade 1 at three revolutions with different λ values at transient-state.

6.2. Simple Dynamic Simulation Results

6.2.1. Comparison of Simple Dynamic and CFD Simulations

In order to estimate the torque of the rotor induced by the wind (T_{wind}) to solve the rotor dynamics in (3.1), the CFD simulation uses the flow field obtained from the finite-element method, whereas the simple dynamic simulation uses the averaged quasi-steady $\lambda - C_P$ curve obtained from CFD simulations for steady wind. As a result, the difference between the computation times required for simple dynamic and CFD simulations is vast, i.e., milliseconds vs days. Thus, use of simple dynamic simulations instead of CFD simulations would be favorable especially to analyze the long-time behavior of the turbine that corresponds to hundreds of revolutions of the rotor (about 75 – 100 seconds).

In Figure 6.22, the dynamic responses of the load coefficient, rotor velocity, generator power, and wind torque for the large wind gust are compared for $20 \leq t \leq 35$ s of the CFD and simple dynamic simulations. The control variable, K_L , follows almost the same pattern in both simulations except the short delay (about 0.1 s) of the K_L for the simple dynamic simulation during the rise between 25th and 28th seconds (Figure 6.22b). Likewise, the variations of the rotor velocity for both simulations are almost identical excluding a slight delay of the ω for the simple dynamic simulation around $t = 27$ s, see Figure 6.22c. The combined effect of these discrepancies leads to a relatively large delay of the power output for the simple dynamic simulations yet still the patterns are very similar for both simulations, as shown in Figure 6.22d.

Although the unsteady behavior of the C_P and the large oscillations of the wind torque that are present due to the flow physics and blade-to-blade interactions in CFD simulations are omitted in simple dynamic simulations (see Figure 6.22e), the performance of the simple dynamic simulation can be deemed satisfactory from a dynamical analysis perspective, e.g., for evaluation of the performance of control designs.

On the other hand, the wind torque oscillations can be mimicked in the simple dynamic simulation by observing the amplitude of the C_P oscillations in CFD simulations. Figure 6.23 shows the amplitude of the C_P oscillations in quasi-steady regime of CFD simulations for steady wind and the fourth-order polynomial fit to this data, which can be used to estimate the amplitude from the tip-speed ratio. Furthermore, it is known that the frequency of the oscillations is 3ω due to the three-bladed configuration of the rotor, and the oscillations of the wind torque and the power coefficient are in-sync. Thus, the instantaneous value of the power coefficient can be calculated as a function of the tip-speed ratio and the time, as follows:

$$C_P(\lambda, t) = C_P(\lambda) + C_{P,amplitude}(\lambda) \sin(3\omega_{ref,0}t) \quad (5.14)$$

where $C_P(\lambda, t)$ is the instantaneous power coefficient, $C_P(\lambda)$ is the averaged quasi-steady power coefficient and $\omega_{ref,0}$ is the reference rotor velocity for the free-stream wind velocity U_0 .

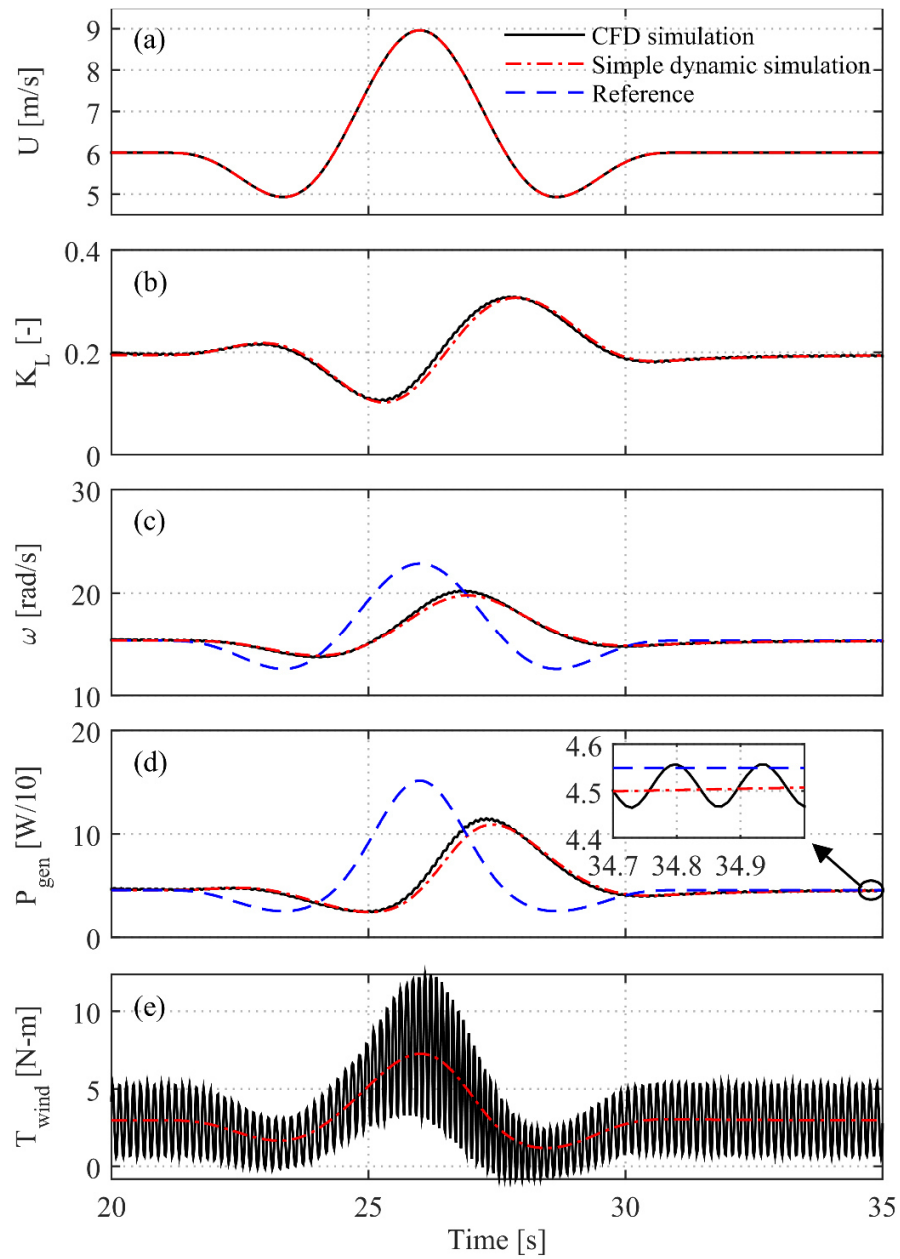


Figure 6.22: Large wind gust profile (a); dynamic responses of the load coefficient (b), rotor velocity (c), generator power (d), and wind torque (e) for CFD and simple dynamic simulations.

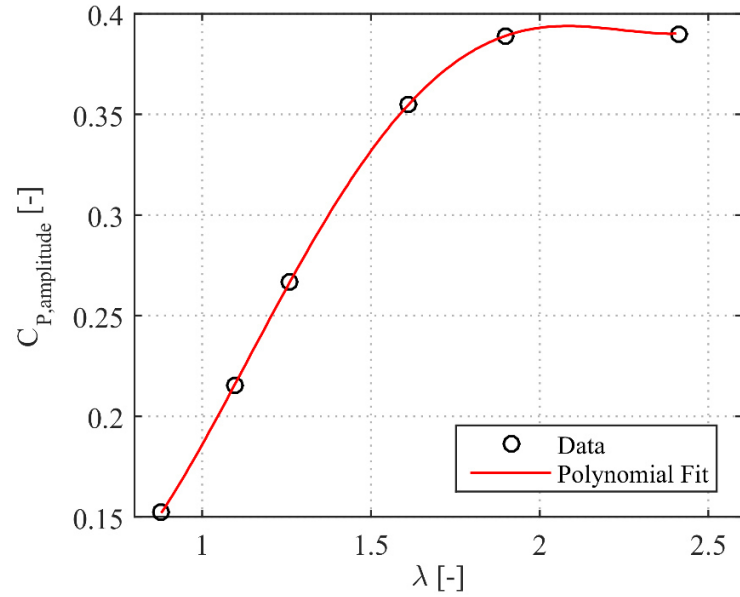


Figure 6.23: Amplitude of C_P oscillations in quasi-steady regime of CFD simulations for steady wind.

Figure 6.24 shows the dynamic responses of the load coefficient, rotor velocity, generator power, and wind torque for the CFD simulation and the simple dynamic simulation in which the C_P oscillates. Since the wind torque is calculated from the power coefficient as in (3.4) in simple dynamic simulations, the wind torque and other variables such as the generator power oscillate likewise the CFD simulation case, as shown in Figs. 6.24d and e. However, the effect of the C_P oscillations and the resulting oscillations on the dynamic response seem to be negligible. Thus, it can be said that the minor differences between the responses of the CFD and simple dynamic simulations are caused by the impact of the unsteady wind on the power coefficient rather than the C_P oscillations.

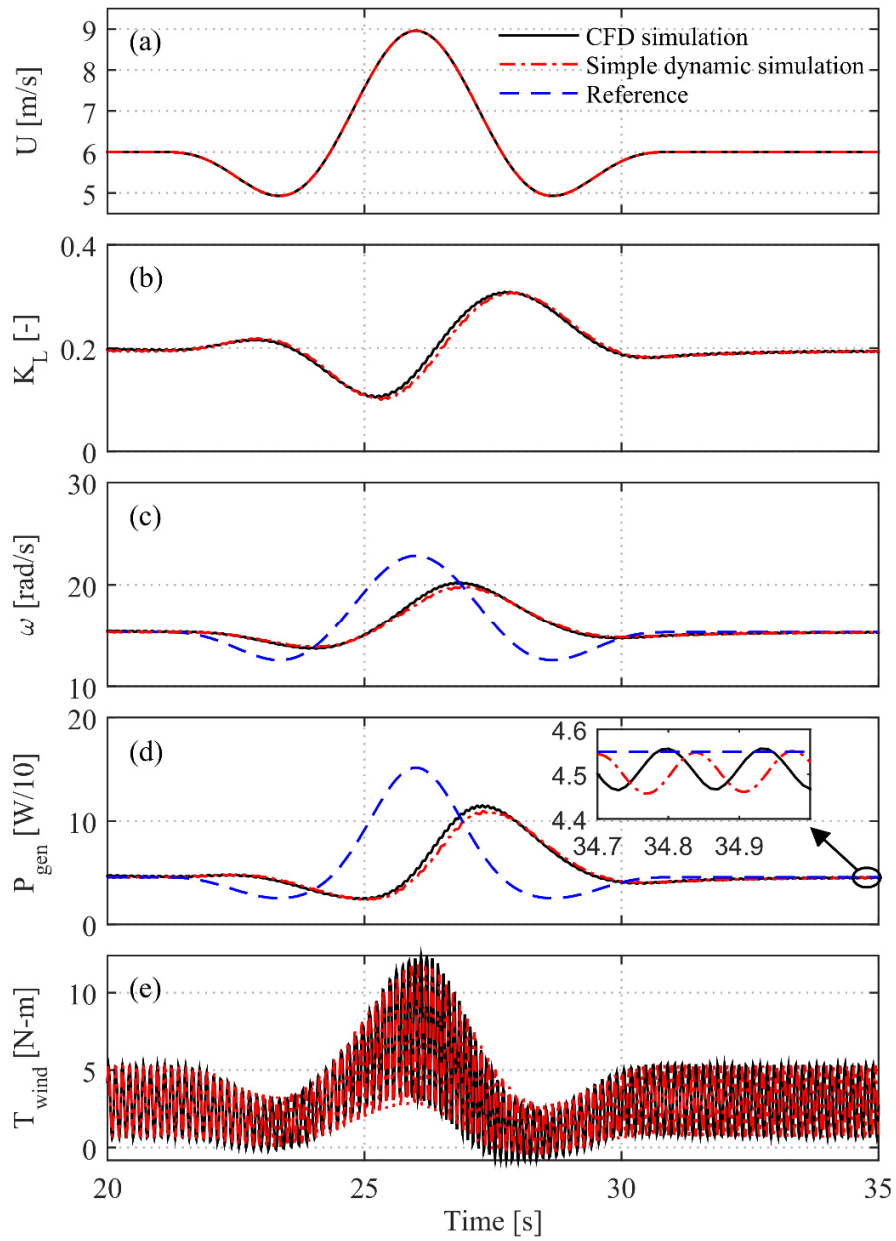


Figure 6.24: Large wind gust profile (a); dynamic responses of the load coefficient (b), rotor velocity (c), generator power (d), and wind torque (e) for the CFD simulation and the simple dynamic simulation with C_P oscillations.

6.2.2. Control Results

The comparison of the CFD and simple dynamic simulations shows that the simple dynamic simulation is sufficient to evaluate the performance of control designs. Thus, the simple dynamic simulation is employed to test and compare the control algorithms under various wind conditions to minimize the computational effort. The fixed- and variable-step MPPT algorithms, the MPC, and the MPC-mimicking SNC are simulated for a step wind, a wind gust, and a real wind data. For all simulations here, C_p oscillations are omitted, and the initial rotor velocity is 5 rad/s because the hill-climb search MPPT algorithms are incremental techniques. Since the control variable is the generator torque for the MPC and the load coefficient for the other methods, and plotting responses of all controllers in a single figure would be chaotic; results for the MPPT algorithms and the SNC and results for the MPC and the SNC are shown in separate figures.

First, the controllers are tested for a 60-second step wind (Figure 6.25a). In fact, a step wind is not realistic but still a step response is useful to observe the characteristics of a dynamical system. Figure 6.25 shows the responses of the fixed- and variable-step MPPT algorithms and the SNC for the step wind. At the beginning of the simulation and after the wind velocity steps up, the MPPT algorithms start to increase the K_L immediately; whereas, the MPC-mimicking SNC sets the K_L to zero and let the turbine to speed up in this period and then rises the K_L suddenly when the rotor velocity approaches to its optimal value, as shown in Figs. 6.25b and c. In spite of that all methods are capable of settling the power output to the MPP, the “greedy” behavior of the MPPT algorithms leads to a postponed (about 5 seconds) manifestation of the maximum power, see Figure 6.25d. As a result, the fixed-step MPPT, the variable-step MPPT, and the SNC methods harvest 93.20%, 92.94%, and 94.59% of the available energy, respectively. In other words, the MPC-mimicking SNC outperforms the model-free MPPT algorithms by generating about 100 Joules of more energy in a minute. On the other hand, the fixed-step MPPT control is found to perform slightly better than the variable-step version in terms of energy efficiency because the latter cannot turn variable step-size into advantage, i.e., smaller steps around the MPP to prevent jitters, since this is an idealized case in which there prevails neither wind fluctuations nor oscillations due to C_p oscillations and/or noise.

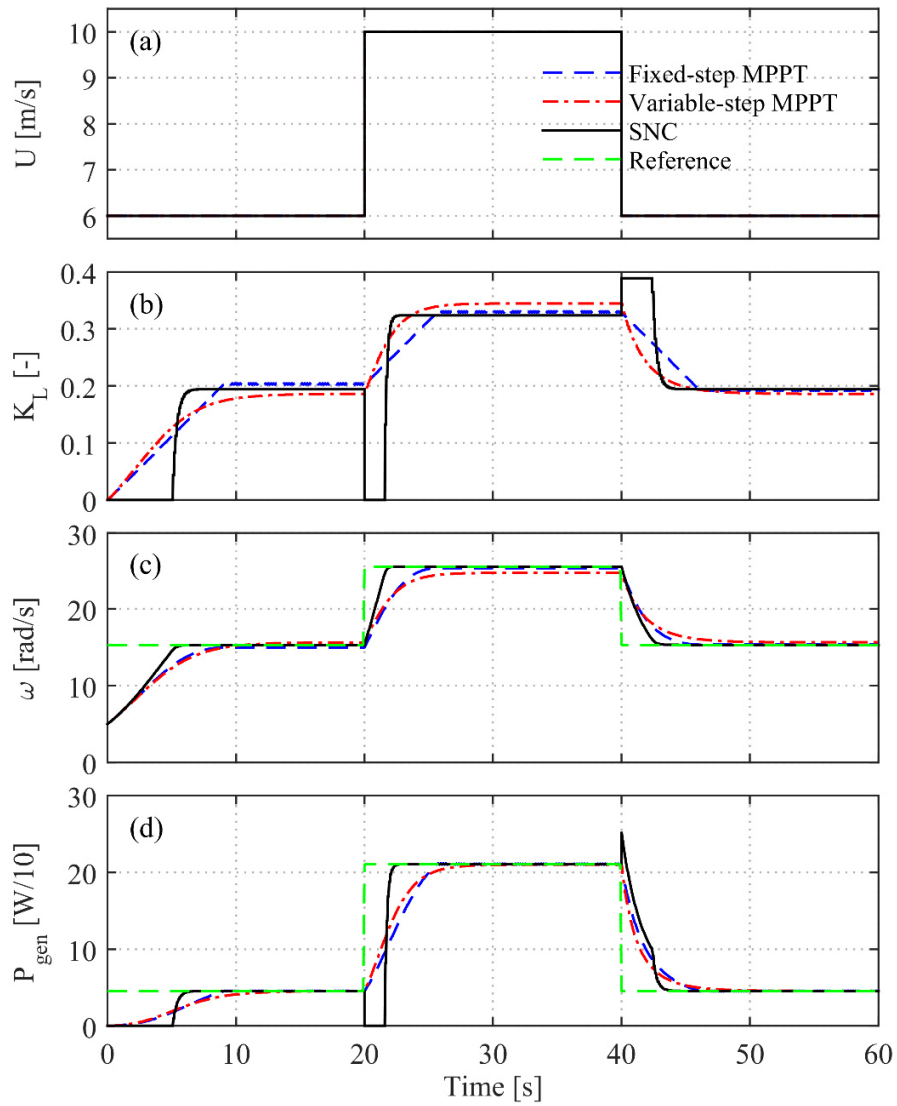


Figure 6.25: Step wind profile (a); dynamic responses of the load coefficient (b), rotor velocity (c), and generator power (d) for the MPPT and SNC algorithms for simple dynamic simulations.

Figure 6.26 shows the performances of the MPC and the SNC for the same step wind (Figure 6.26a). Since the control variables are different, both the load coefficient and the generator torque are plotted in this case (Figs. 6.26b and c). Although the control variables and the control sampling periods are different and the SNC does not exploit the wind velocity like the MPC, the similarity between the dynamic responses, especially the power output shown in Figure 6.26e, for the MPC and the SNC is undeniable. The most remarkable discrepancy between them is that the MPC decreases the generator load about 3 seconds prior to the rise of the wind velocity by the virtue of its prediction ability, whereas the SNC decreases the K_L when the wind velocity steps up; so, the power output for the MPC reaches to the maximum value about 1 s earlier than the SNC. The MPC behaves similarly when the wind velocity steps down as well. Consequently, the energy efficiency for the MPC is 95.30% while it is 94.59% for the SNC; admittedly, the performance of the SNC is satisfactory in the sense of MPC-mimicking.

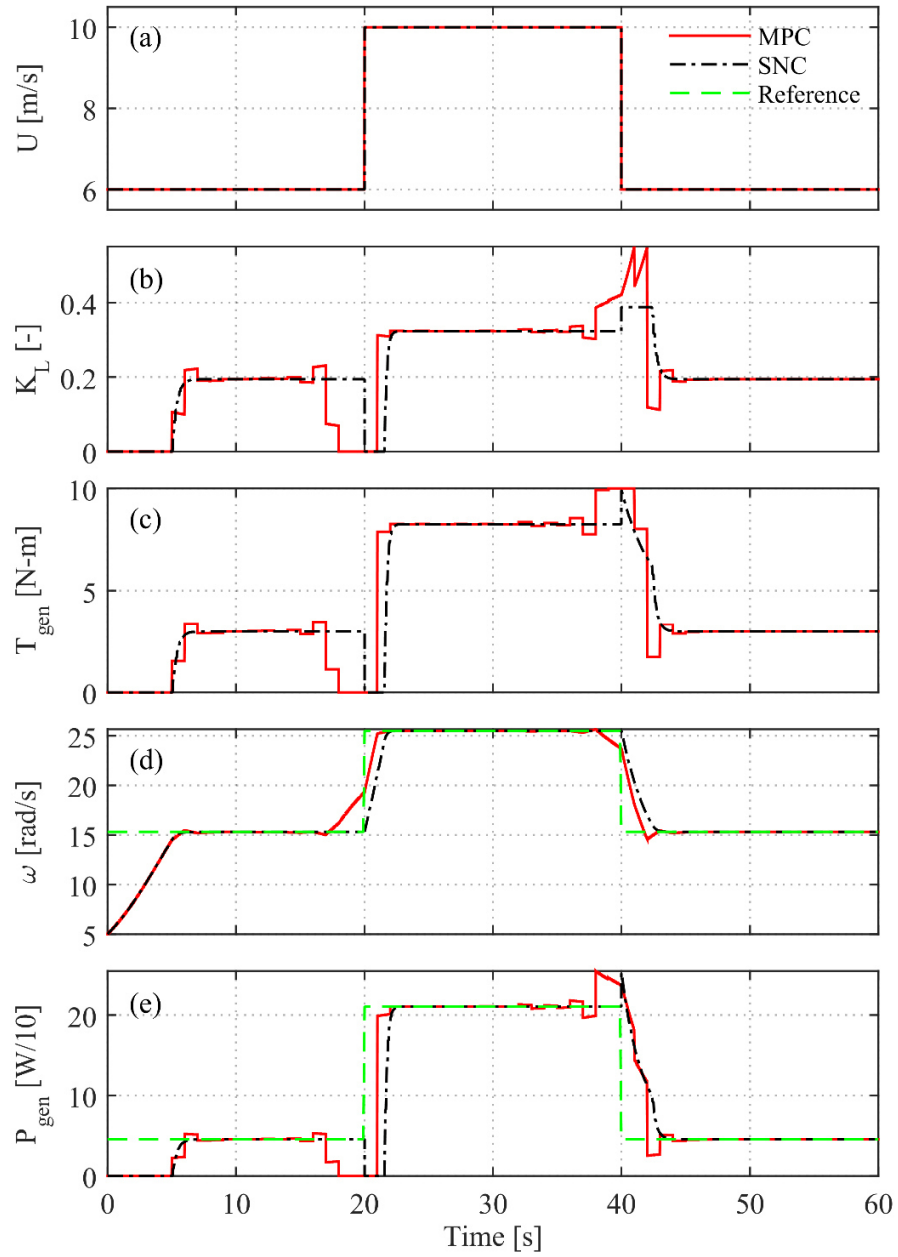


Figure 6.26: Step wind profile (a); dynamic responses of the load coefficient (b), generator torque (c), rotor velocity (d), and generator power (e) for the MPC and the SNC for simple dynamic simulations.

Second, the control methods are tested for a 40-second wind gust profile for which $t_0 = 15$ s, $T_g = 10$ s, and $u_e = 5$ m/s (Figure 6.27a). Wind gust is useful to observe the transient performance of the system. Figure 6.27 illustrates the responses of the MPPT algorithms and the SNC. The SNC manipulates the K_L aggressively during the gust, while the incremental MPPT algorithms vary the K_L more smoothly (see Figure 6.27b). It is also seen that the variation of the K_L for the variable-step MPPT is larger than the variation for the fixed-step algorithm due to the dependency of the step-size on the change of the rotor velocity; as a result, the power output reaches to higher values for the variable-step algorithm, as shown in Figure 6.27d. Additionally, the fixed-step MPPT settles the system to a different (i.e., lower generator load, higher angular velocity) operating point after the gust yet still maximizes the power output. The energy efficiencies for the fixed-step MPPT, the variable-step MPPT, and the SNC are 79.67%, 82.18%, and 84.95%, respectively; namely, the SNC again outperforms the MPPT algorithms, and the variable-step MPPT turns the variable step-size into an advantage and demonstrates a better performance than the fixed-step algorithm.

Figure 6.28 shows the responses of the MPC and the SNC for the same wind gust profile. Clearly, the responses of the MPC and the MPC-mimicking SNC are very close to each other. However, the MPC exploits the wind velocity prediction and sets the generator load to zero at the beginning of the gust and about 2 s before the SNC (see Figure 6.28b) so that the rotor velocity remains above the reference in contrast to the SNC case, as shown in Figure 6.28c. In addition, after the peak of the wind gust, the MPC adjusts the generator torque such that the rotor velocity almost perfectly tracks the reference despite the high control sampling period, whereas the SNC operates in the proportional control region but cannot track the reference velocity similarly. The resulting energy efficiencies for the MPC and the SNC are 87.01% and 84.95%, respectively.

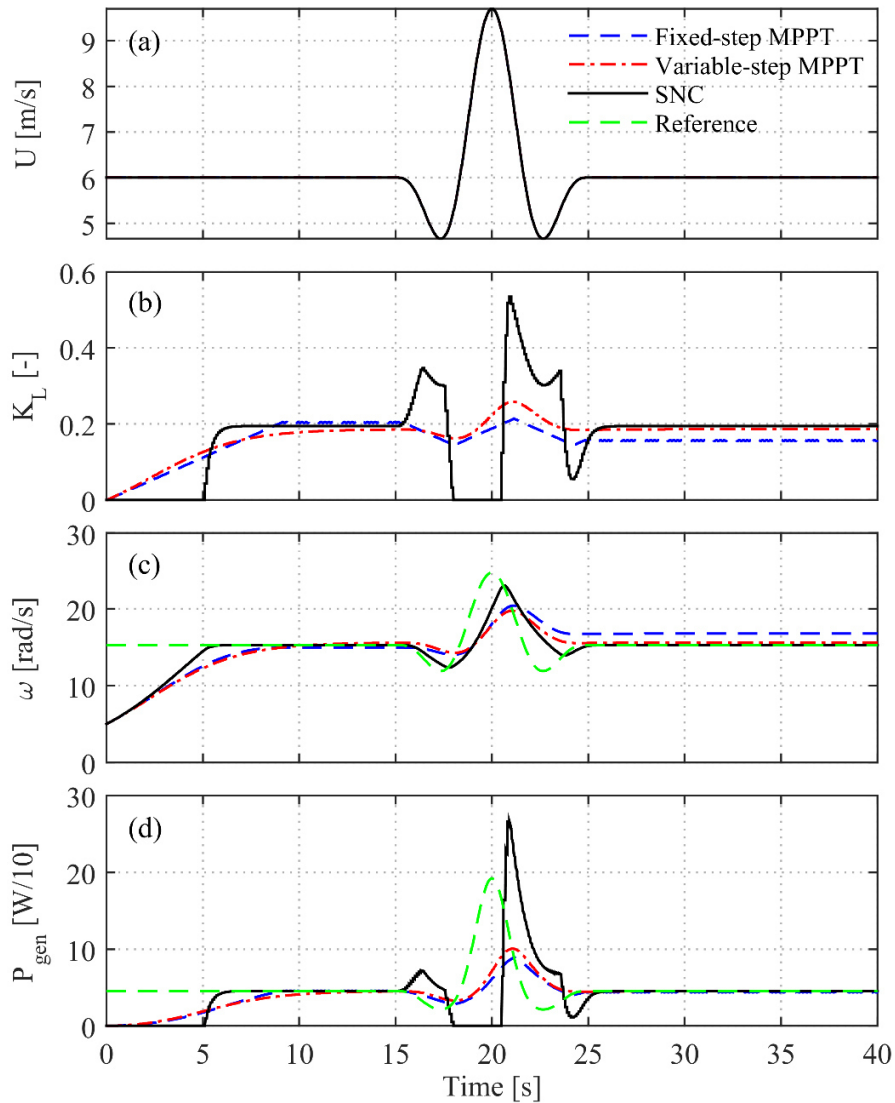


Figure 6.27: Wind gust profile (a); dynamic responses of the load coefficient (b), rotor velocity (c), and generator power (d) for the MPPT and SNC algorithms for simple dynamic simulations.

Last, the real wind data described in Chapter 4 (see Figure 6.29a) is used to evaluate the performances of the controllers under realistic wind conditions. The wind data, which was logged in an urban environment, has very fast dynamics and is 298 seconds long. It is seen that the fixed-step MPPT is not suitable to track the MPP for such a fast changing urban wind, see Figure 6.29d, whereas the variable-step algorithm performs effectively. On the other hand, the SNC changes the K_L very rapidly in a wide range while the incremental variable-step MPPT operates smoothly, as shown in Figure 6.29b. In consequence, the fixed-

step MPPT, the variable-step MPPT, and the SNC convert 29.40%, 94.21%, and 96.84% of the available energy into electricity.

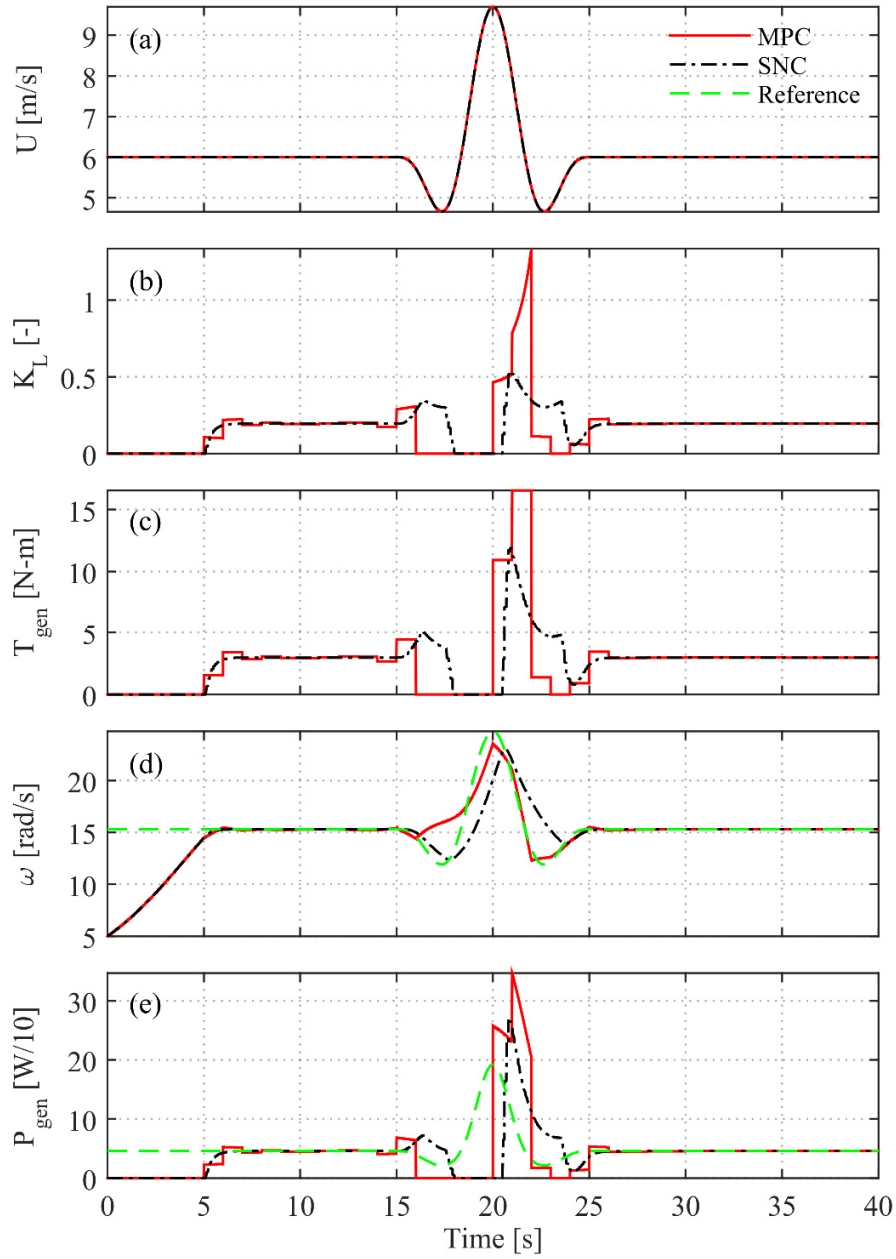


Figure 6.28: Wind gust profile (a); dynamic responses of the load coefficient (b), generator torque (c), rotor velocity (d), and generator power (e) for the MPC and the SNC for simple dynamic simulations.

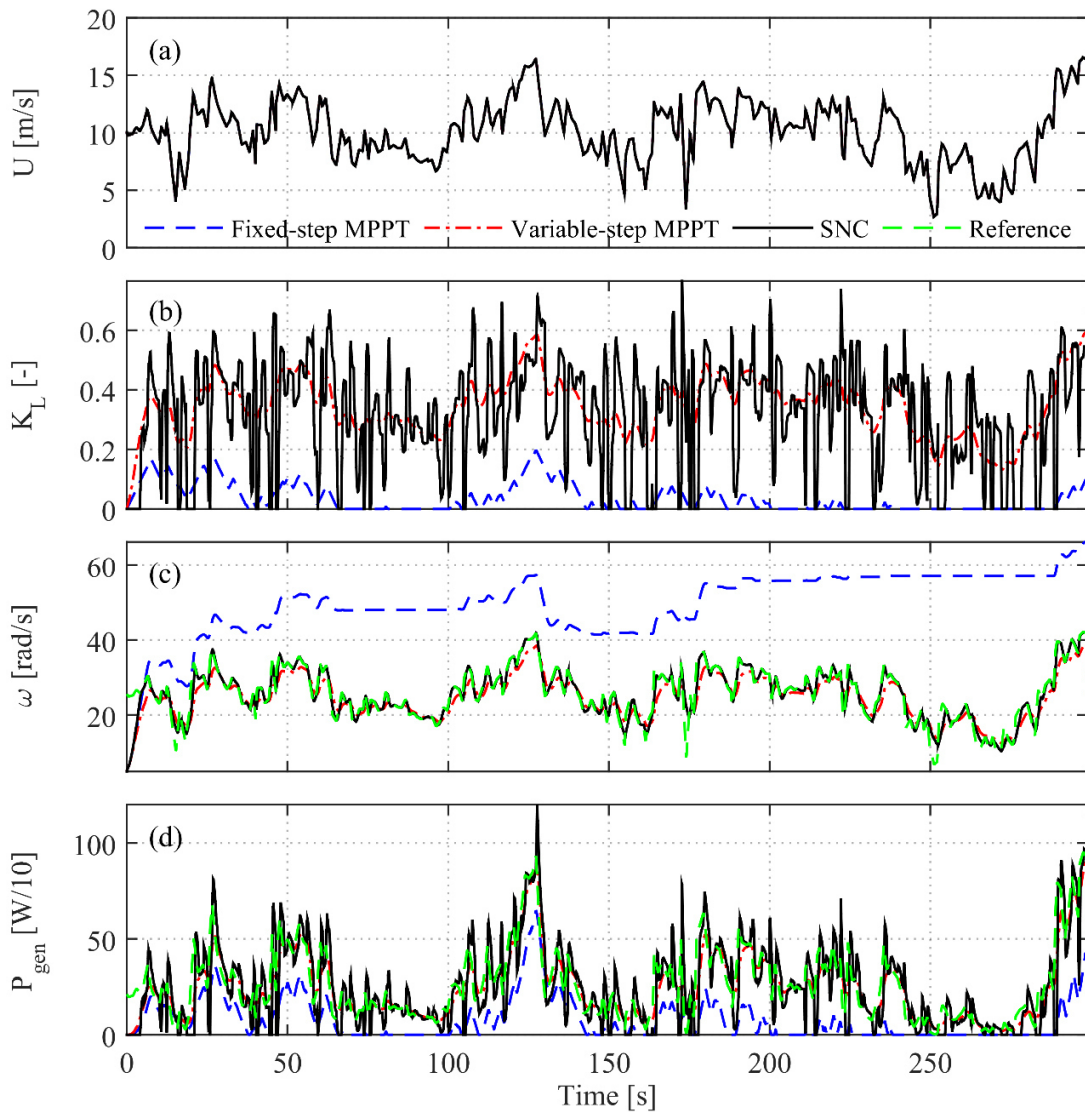


Figure 6.29: Real wind profile (a); dynamic responses of the load coefficient (b), rotor velocity (c), and generator power (d) for the MPPT and SNC algorithms for simple dynamic simulations.

The responses of the MPC and the SNC for the same wind input are depicted in Figure 6.30. Both algorithms perform similarly and varies the load very rapidly; however, the high sampling period of the MPC encumbers the MPC from applying fast changes in response to the fast wind dynamics. On the other hand, the SNC, which has an order of magnitude lower sampling period than the MPC, handles the K_L as necessary and prevents deviations from the reference rotor velocity in contrast to the MPC, as shown in Figure 6.30d. The resulting energy efficiencies for the MPC and the SNC are 96.36% and 96.84%, respectively; namely, the MPC-mimicking SNC slightly outperforms the MPC in this case owing to its agility.

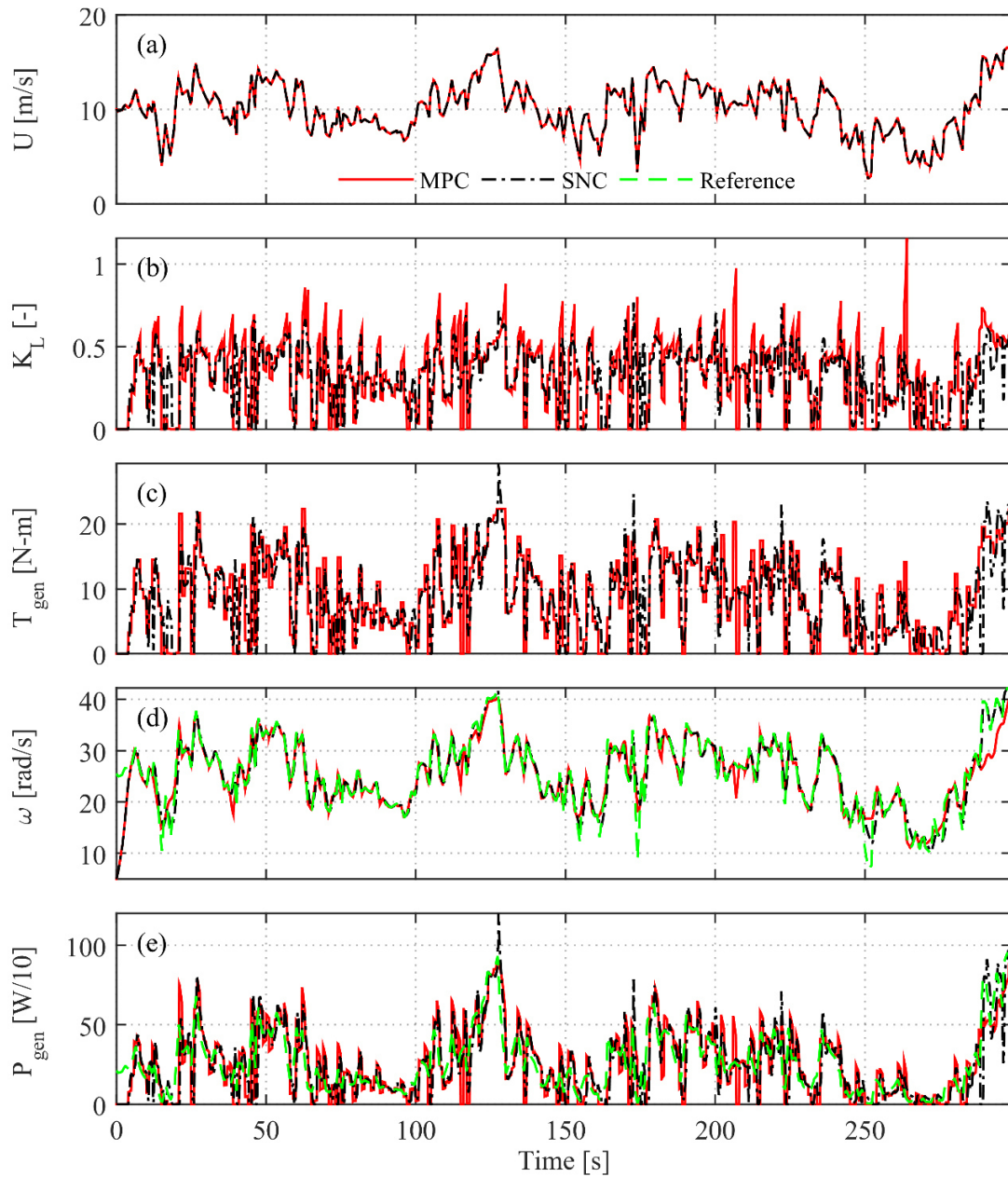


Figure 6.30: Real wind profile (a); dynamic responses of the load coefficient (b), generator torque (c), rotor velocity (d), and generator power (e) for the MPC and the SNC for simple dynamic simulations.

The energy efficiency results of the MPPT, MPC and SNC algorithms for the step wind, wind gust, and real wind inputs are tabularized in Table 6.2 and yield the following observations. First, the energy efficiency results for all control methods are very close to each other for the step wind case (i.e., the maximum difference is about 2%), in which steady-state performance has more weight; furthermore, only for this case the fixed-step MPPT generates

more energy than the variable-step algorithm. Hence, it can be admitted that all of the controllers are tuned properly and their performances are comparable.

Second, both the MPC and the SNC overcome the MPPT algorithms in terms of energy generation in all cases. This result is mainly caused by the fact that the MPPT control represents a “greedy” algorithm that maximizes the power output for instantaneous conditions, while the MPC and the SNC designs strategize and maximize the energy output of the turbine. Thus, it can be concluded that maximizing the instantaneous power does not mean maximizing the energy production. The results show that the MPC and the SNC allow deviations from the maximum power instantaneously for future gains in energy generation.

Third, the dynamic responses of the MPC and the SNC demonstrate similar characteristics, and the energy efficiency discrepancy between them is generally low for all cases. The energy efficiency difference peaks for the wind gust input (i.e., about 2%); for such an intense wind transient, the prediction ability of the MPC becomes a significant advantage, whereas its impact is limited for the other cases. On the other hand, the energy output of the SNC exceeds the MPC’s for the real wind case due to the low sampling rate of the MPC. As a result, the overall low differences between the dynamic responses and the resulting energy efficiencies of the MPC and the SNC show that the performance of the SNC is acceptable in the sense of mimicking the MPC.

Table 6.2: Energy efficiency results for simple dynamic simulations.

Control \ Wind	Fixed-step MPPT	Variable-step MPPT	MPC	SNC
Step Wind	93.1954%	92.9402%	95.2975%	94.4853%
Wind Gust	79.6680%	82.1837%	87.0061%	84.9540%
Real Wind	29.3973%	94.2100%	96.3625%	96.8382%

Last, the model-free and wind speed sensorless variable-step MPPT algorithm performs successfully for all wind inputs and yields energy efficiencies that are close to the maximum energy efficiencies achieved, e.g., for the real wind, the difference is about 2%. Therefore, the variable-step MPPT can be preferred over the SNC which requires both the power coefficient curve of the turbine and wind velocity measurement.

6.3. Hardware-in-the-loop Simulation Results

The CFD model and the simple dynamic model are based on an idealized electromechanical conversion model to investigate solely the aerodynamic performance of the turbine; in other words, the mechanical power output of the rotor, P_{wind} , and the electrical power output of the complete system, P_{gen} , are assumed to be equal for previous results. Notwithstanding, the power output of the complete system including the generator and power electronics components is expected to be lower than the mechanical power produced by the blades of the VAWT due to the inevitable losses of the actual components.

In order to analyze this effect, the electromechanical model, which is shown to be a valid tool to estimate the load voltage and the power output of the HIL test-bed for given rotor velocity and load current values, is employed. Electromechanical simulations are performed under steady wind conditions, and the power output is estimated as the rotor velocity and the load current are increased gradually. Figure 6.31 depicts the mechanical power captured by the rotor, P_{wind} , for a steady wind velocity of 6 m/s and the electrical power output of the load, P_{gen} , for the same conditions. This result demonstrates that the impact of the characteristics of the generator and power electronics components reduces the MPP, e.g., the maximum value of the electrical power output is 67% of the maximum value of the mechanical power output; additionally, it shifts the MPP as well as the shape of the curve to higher rotor velocities, which implies that the most dominant loss on this system is the resistive loss that is proportional to the square of the current rather than the inductive loss and emphasizes the importance of picking the right generator for the turbine.

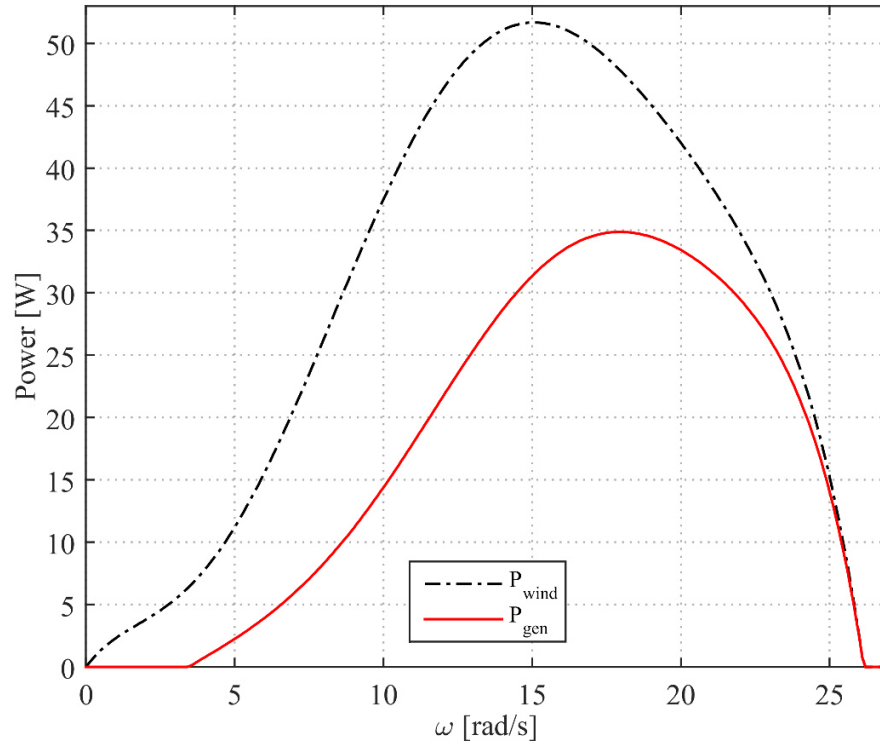


Figure 6.31: Mechanical power produced by the rotor, P_{wind} , and electrical power produced by the complete system, P_{gen} , vs the rotor velocity for $U = 6$ m/s.

Figure 6.2 shows that the aerodynamic power characteristics of a VAWT rotor can be represented by a single $\lambda - C_P$ curve independently of the wind velocity. Hence, one can expect that the electrical power characteristics can be represented by a $V_L/U - C_{Pgen}$ curve. However, Figure 6.32 shows that the electrical power characteristics for different wind velocities are not similar as $\lambda - C_P$ curves. The maximum C_{Pgen} value decreases as the wind velocity increases, and the difference between the maximum values is proportional to the difference between the wind velocities; whereas, the corresponding V_L/U value does not change considerably. Overall, these results reveal that the effect of the generator and power electronics components on the power characteristics is significant and should be taken into account for the overall system design including the controller and considering the wind characteristics for a given site.

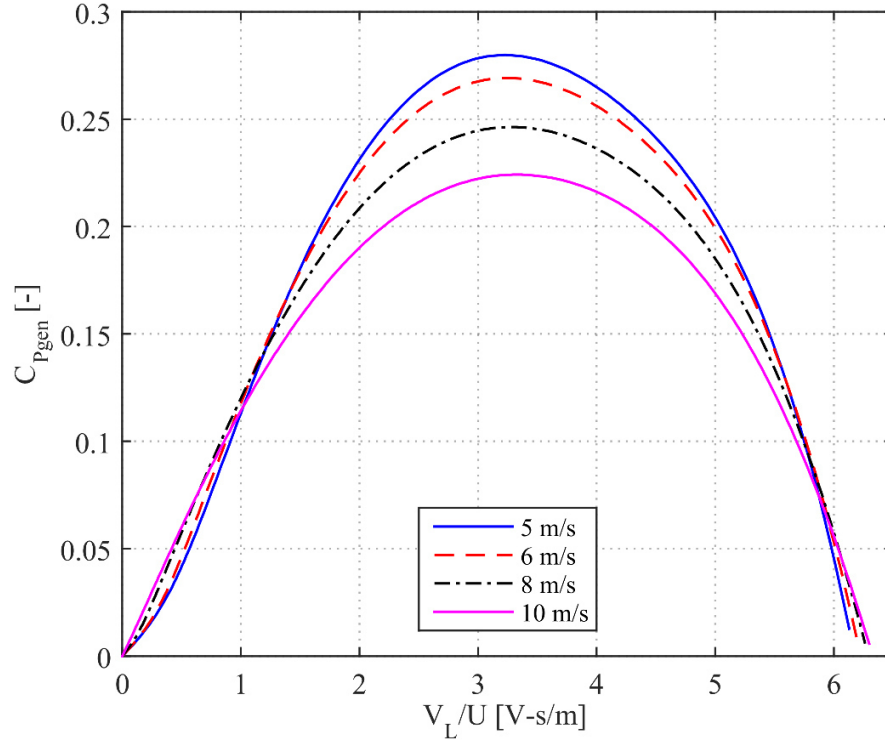


Figure 6.32: $V_L/U - C_{Pgen}$ curves for a range of steady wind velocities.

6.3.1. Electromechanical Simulation Control Results

The SNC algorithm is redesigned and tuned for HIL simulations through electromechanical simulations; moreover, our implementation of the MPC cannot operate in real-time. Hence, first, the electromechanical simulation is employed to test and compare the control algorithms under various wind conditions. The fixed- and variable-step MPPT algorithms, the MPC, and the MPC-mimicking SNC are simulated for a step wind, a wind gust, and a real wind data as in the simple dynamic simulation case. For all simulations here, the initial rotor velocity is 5 rad/s because the hill-climb search MPPT algorithms are incremental techniques. Since plotting responses of all controllers in a single figure would be chaotic; results for the MPPT and SNC methods and results for the MPC and the SNC are shown in separate figures.

First, the controllers are tested for a 60-second step wind (see Figure 6.33a). Step response is useful to observe dynamical characteristics such as time constant of the system including controller. Figure 6.33 shows the responses of the fixed- and variable-step MPPT algorithms and the SNC for the step wind. Clearly, the settling time is roughly the same for all controllers showing that they are tuned appropriately. According to Figs. 6.33c and d, the model-based SNC, expectedly, tracks the reference operating conditions, whereas, the model free fixed- and variable-step MPPT methods operate the system at different operating conditions; nonetheless, the resulting power outputs for the model-free variable-step MPPT control and the MPC-mimicking SNC are very similar to each other and seemingly converge to the MPP for both wind velocities but the power output for fixed-step MPPT algorithm has relatively large steady-state error, as shown in Figure 6.33e. Despite the similarity of the power output responses, the SNC outperforms the variable-step MPPT in terms of energy generation with an energy efficiency of 93.79%, while the energy efficiency for the variable-step MPPT is 91.41% and higher than the energy output of the fixed-step MPPT which is 88.74%.

Figure 6.34 shows the responses of the MPC and the SNC for the same wind profile. Due to the low value of γ , the SNC operates mostly in the proportional control region, see Figure 6.34c yet still successfully mimics the MPC, admittedly. The only difference is that the MPC decreases the load current slightly a short period prior to the wind velocity changes owing to its prediction ability. Nevertheless, its impact on the energy output is limited: the SNC captures 93.79% of the available energy, while the MPC captures 94.11%.

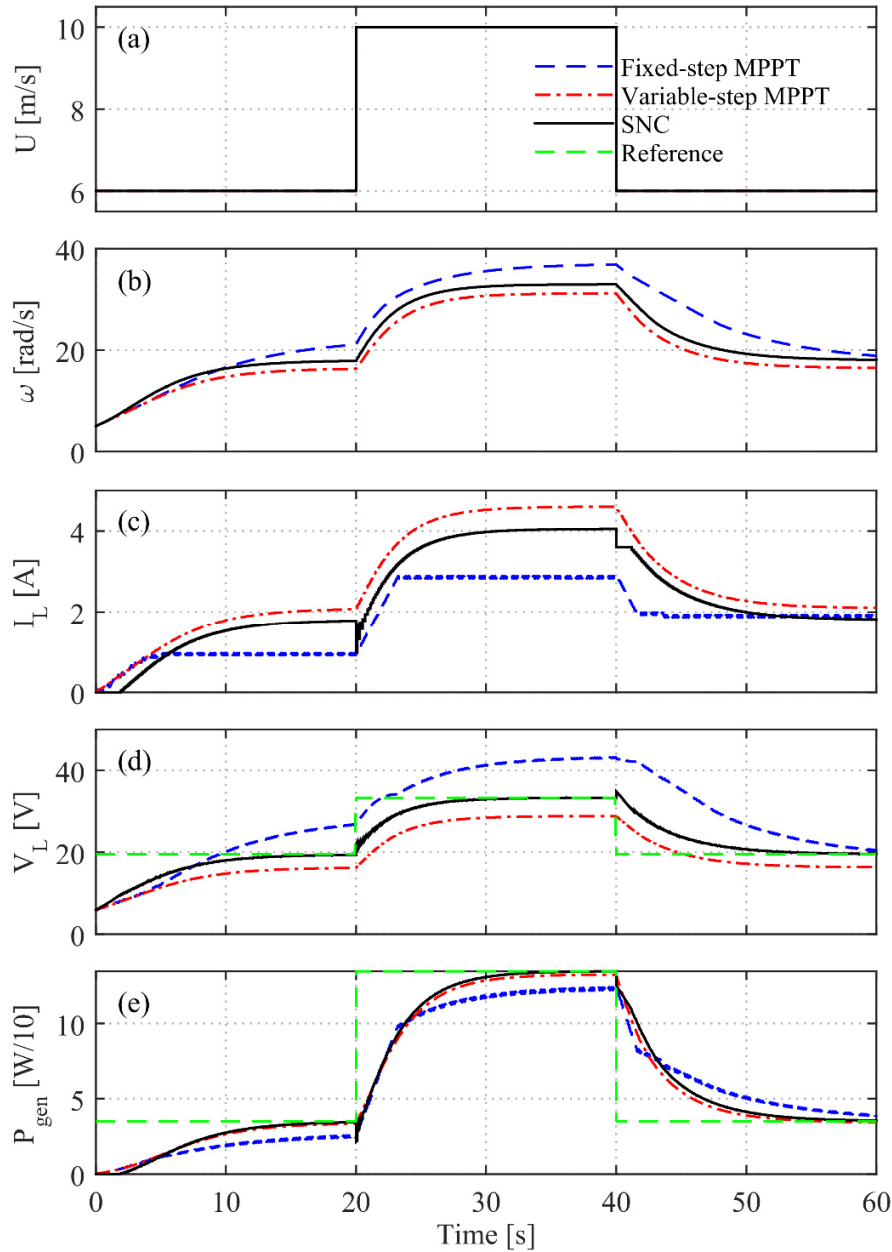


Figure 6.33: Step wind profile (a); dynamic responses of the load coefficient (b), rotor velocity (c), and generator power (d) for the MPPT and SNC algorithms for electromechanical simulations.

Second, the control methods are tested for the wind gust (Figure 6.35a). Figure 6.35 illustrates the responses of the MPPT algorithms and the SNC. For the fixed-step MPPT, first, the I_L settles to about 1 A, which does not correspond to the MPP; however, after the gust, the I_L settles to a higher value so that the P_{gen} converges to the MPP; while, the steady-state value of the I_L does not change for the other controllers, see Figure 6.35c.

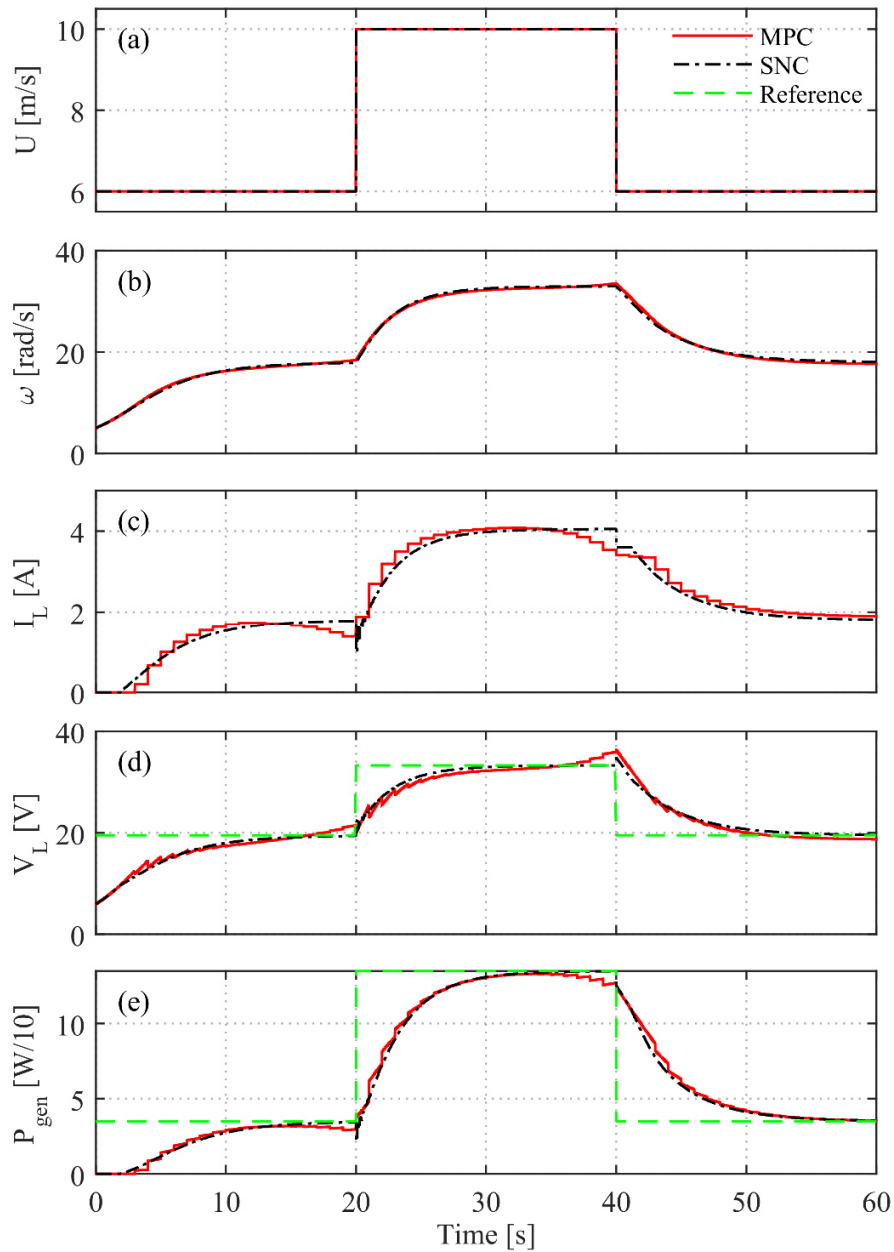


Figure 6.34: Step wind profile (a); dynamic responses of the load coefficient (b), rotor velocity (c), and generator power (d) for the MPC and SNC for electromechanical simulations.

The resulting energy efficiencies for the fixed- and variable-step MPPT, and the SNC are 78.93%, 79.43%, and 81.79%, respectively; namely, the SNC again outperforms the MPPT algorithms. However, it is remarkable that the fixed-step MPPT attains to an energy efficiency close to the other controllers, although its power output is well below the power

outputs of the other controllers for $t < 20$ s. This is because of the fact that it utilizes the kinetic energy of the rotor by setting the I_L to a higher value after the wind transient.

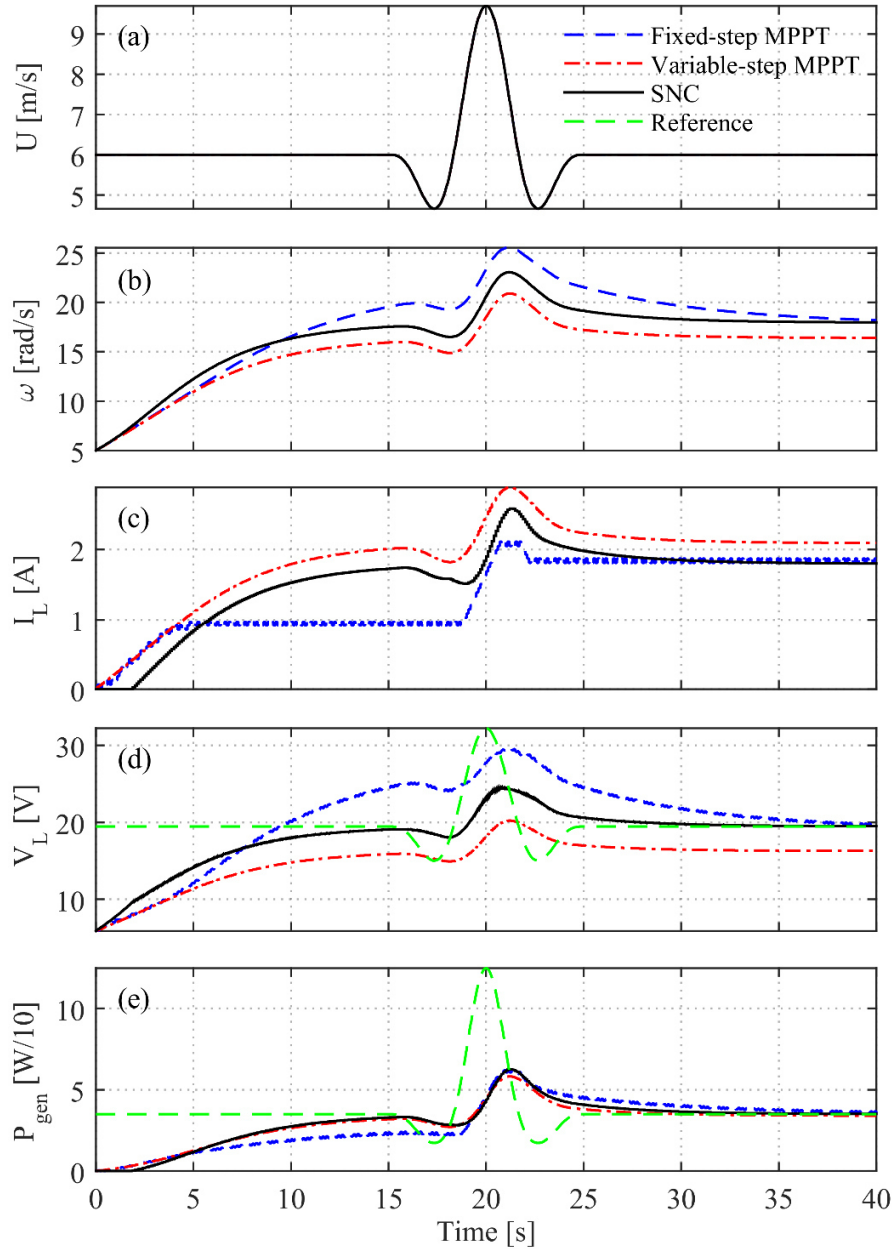


Figure 6.35: Wind gust profile (a); dynamic responses of the load coefficient (b), rotor velocity (c), and generator power (d) for the MPPT and SNC algorithms for electromechanical simulations.

Figure 6.36 shows that the SNC demonstrates a successful performance in the sense of mimicking the MPC for the wind gust profile, namely under a large wind transient, as well. Consistently, their energy yields are very close; the energy efficiency is 81.79% for the SNC

and 82.34% for the MPC. However, it is noteworthy that after the wind transient, the MPC settles the I_L slightly above the reference value as the fixed-step MPPT.

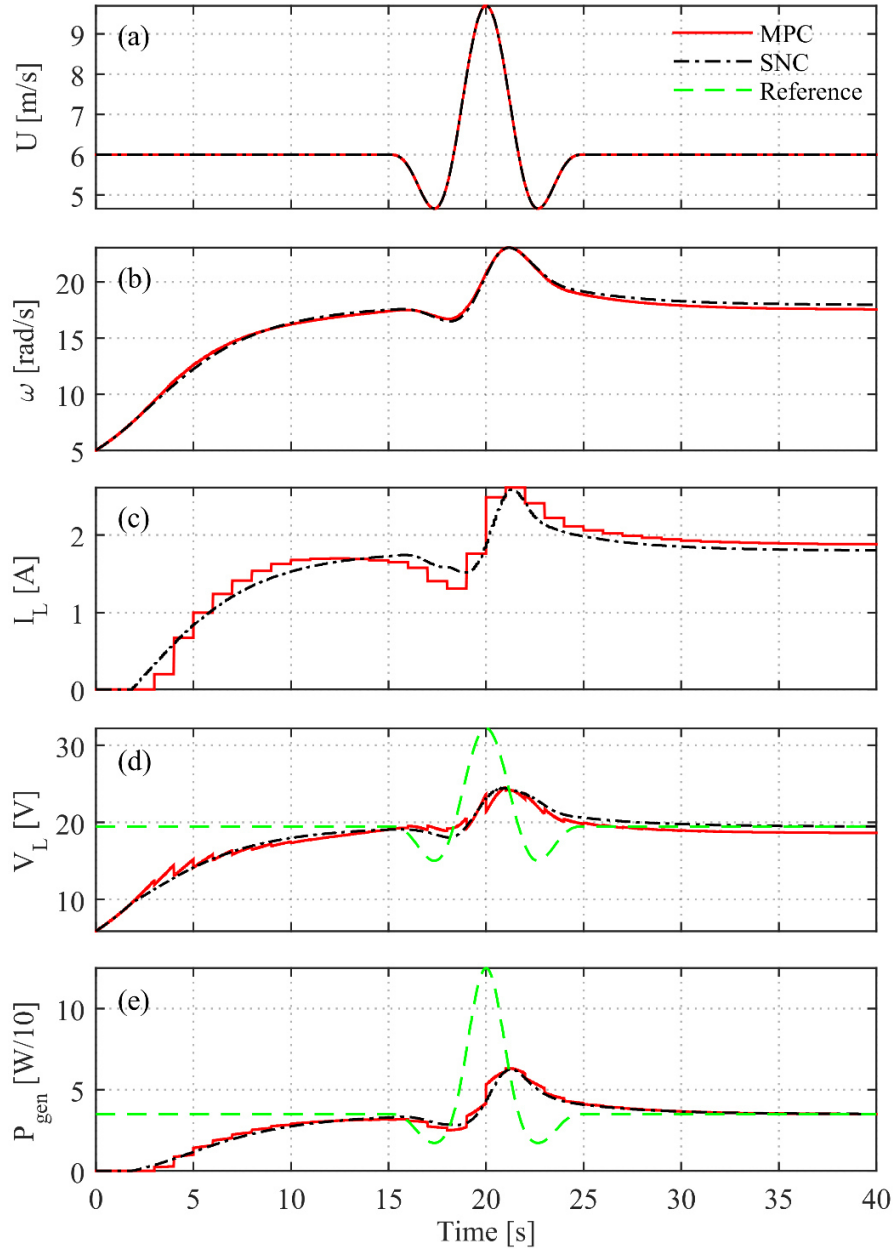


Figure 6.36: Wind gust profile (a); dynamic responses of the load coefficient (b), rotor velocity (c), and generator power (d) for the MPC and the SNC for electromechanical simulations.

Last, the performances of the controllers are compared under realistic conditions using the real wind data shown in Figure 6.37a. Figure 6.37e shows that the power outputs of the controllers are indistinguishable for most of the time despite the fact that the operating

conditions are visibly different (see Figs. 6.37b, c, and d). As a result, the fixed-step MPPT, the variable-step MPPT, and the SNC convert 91.19%, 95.54%, and 97.24% of the available energy into electricity.

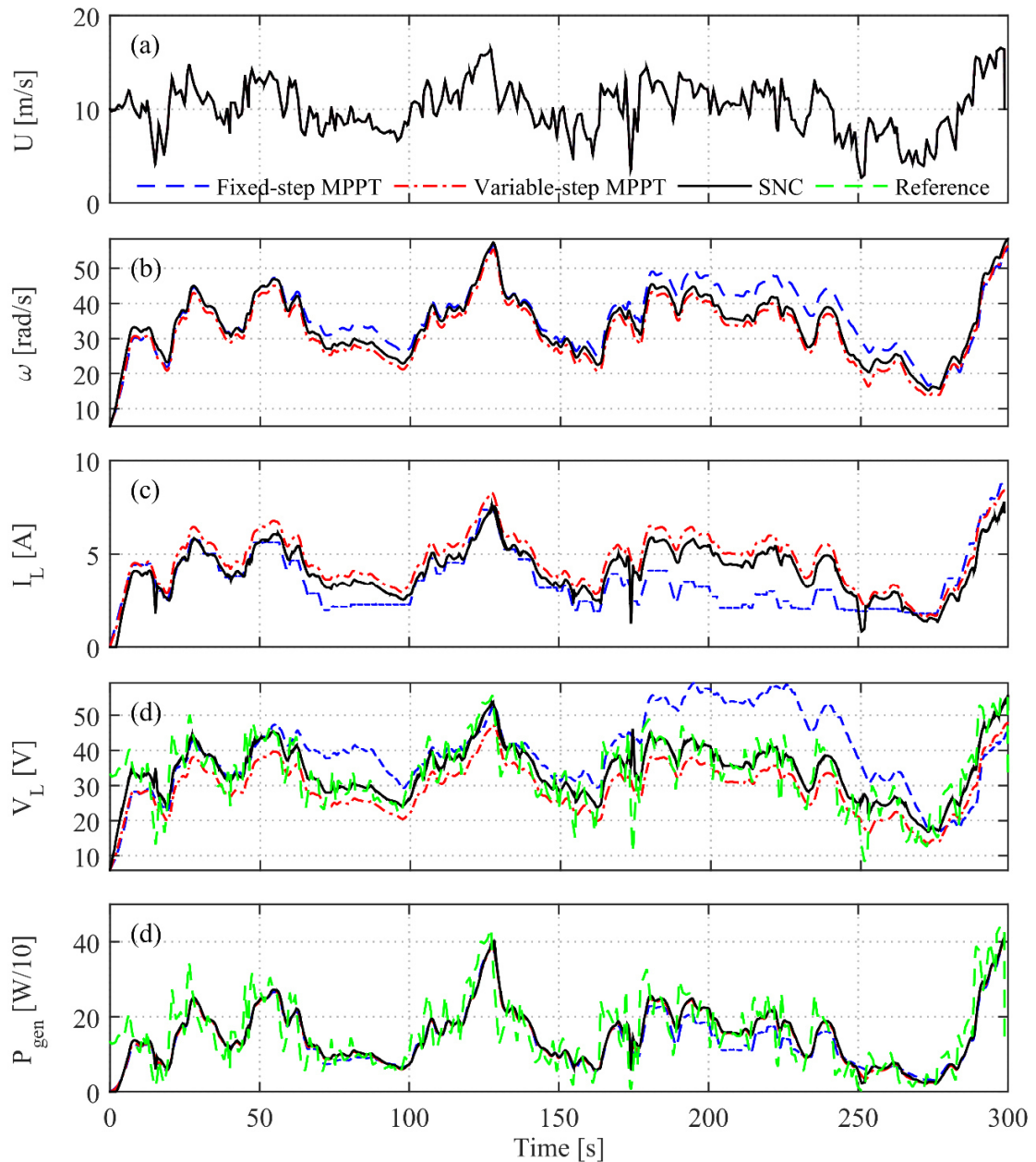


Figure 6.37: Real wind profile (a); dynamic responses of the load coefficient (b), rotor velocity (c), and generator power (d) for the MPPT and SNC algorithms for electromechanical simulations.

The responses of the MPC and the SNC for the real wind is depicted in Figure 6.38. Clearly, their responses are almost identical excluding the sudden drops of the I_L and corresponding peaks of the V_L around $t = \{20, 175, 250\}$ s for the SNC, see Figure 6.38c. Nevertheless, the MPC and the SNC harvest 97.32% and 97.24% of the available energy, respectively, namely their energy yields are almost equal.

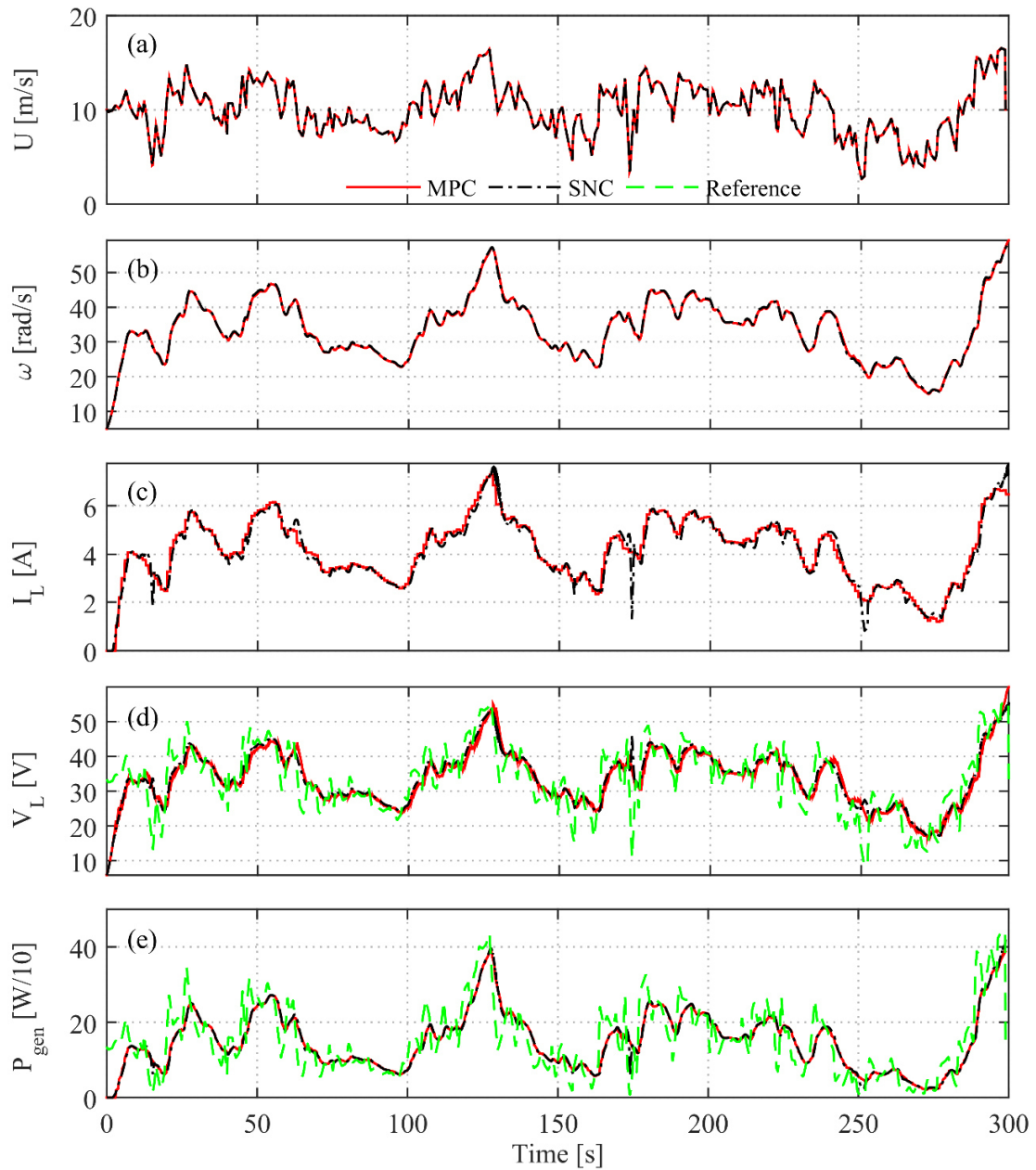


Figure 6.38: Real wind profile (a); dynamic responses of the load coefficient (b), rotor velocity (c), and generator power (d) for the MPC and SNC for electromechanical simulations.

The energy efficiency results of the MPPT, MPC and SNC algorithms for the step wind, wind gust, and real wind inputs are given in Table 6.3 and yield the following observations. First, the energy efficiencies for all of the controllers are in close proximity for each wind type. Hence, one can say that the control parameters are adjusted properly and the responses are comparable.

Second, both the MPC and the SNC overcome the MPPT algorithms in terms of energy generation in all cases. The most remarkable difference between the dynamic responses of the MPC and SNC algorithms and the MPPT algorithms is that the load current, load voltage and rotor velocity variables track the reference values for the model-based MPC and SNC methods, as anticipated, whereas they do not converge to the reference values for the model-free MPPT algorithms.

Third, the dynamic responses of the MPC and the SNC are undeniably similar for all cases, and the energy efficiency difference between them is very small for all cases, i.e., less than 1%. On the other hand, the SNC cannot turn the high sampling rate into an advantage as in the simple dynamic simulations. Nevertheless, the negligible discrepancies between the dynamic responses and the resulting energy efficiencies of the MPC and the SNC demonstrate that the performance of the SNC is acceptable in the sense of mimicking the MPC for electromechanical and HIL simulations as well.

Last, the variable-step MPPT outperforms the fixed-step MPPT in terms of energy generation in all cases, as in the simple dynamic simulations. Furthermore, it is also observed that the variable-step algorithm performs more stable than the fixed-step MPPT algorithm.

Table 6.3: Energy efficiency results for electromechanical simulations.

Control \ Wind	Fixed-step MPPT	Variable-step MPPT	MPC	SNC
Step Wind	88.7452%	91.4154%	94.1090%	93.7885%
Wind Gust	78.9251%	79.4256%	82.3379%	81.7859%
Real Wind	91.1855%	95.5427%	97.3192%	97.2437%

6.3.2. Hardware-in-the-loop Simulation Control Results

Heretofore, software-only simulations are employed to study the power characteristics and the dynamics the VAWT. Although these tools provide a significant insight into the performance of the VAWT system, HIL simulations need to be carried out in order to assess the real impact of the actual generator and power electronics components, measurement noise, and real-time control on the performance. Thus, experiments are carried out on the HIL test-bed for the step wind, wind gust, and real wind profiles; however, in this case, only the MPPT algorithms and the SNC are considered since the MPC cannot be implemented in real-time. Nonetheless, the SNC is found to mimic the MPC successfully.

Figure 6.39 shows the rotor velocity, load current, load voltage, and power output responses of the controllers for the step wind profile (Figure 6.39a). As in the electromechanical simulations, the SNC settles the system to reference operating conditions; whereas, the MPPT algorithms settle the system to higher current – lower voltage operating conditions (see Figs. 6.39c and d). As distinct from the electromechanical simulations, the I_L for the SNC has significant fluctuations after the wind velocity steps up, i.e., for $20 < t < 25$ s, which cause V_L and the P_{gen} to fluctuate as well. The SNC is a V_L -feedback control and the voltage drop is dependent on the change of the load current, moreover, measurement noise prevails in the HIL simulation, so the combined effect results in the I_L fluctuations which do not occur in electromechanical simulations. Nevertheless, the power output for the SNC seemingly exceeds the other power outputs throughout the simulation despite the fact that the power output for the variable-step MPPT is proximate, see Figure 6.39e; whereas, the P_{gen} for the fixed-step MPPT has relatively large steady-state error. Consequently, the fixed- and variable-step MPPT controllers and the SNC capture 84.41%, 92.40%, and 95.34% of the available energy, respectively.

The dynamic responses of the controllers for the wind gust profile (Figure 6.40a) are depicted in Figure 6.40. It is noteworthy that as in the electromechanical simulation case, the fixed-step MPPT sets the I_L to a higher value than the value before the gust, see Figure 6.40c, and utilizes the kinetic energy of the rotor that is increased before the gust when the I_L is low. Consequently, the P_{gen} for the fixed-step MPPT exceeds the P_{gen} for the variable-step MPPT during the gust, as shown in Figure 6.40e. On the other hand, the SNC keeps the system at

the reference operating conditions before and after the gust, and its power output exceeds the others, albeit slightly, throughout and after the wind transient.

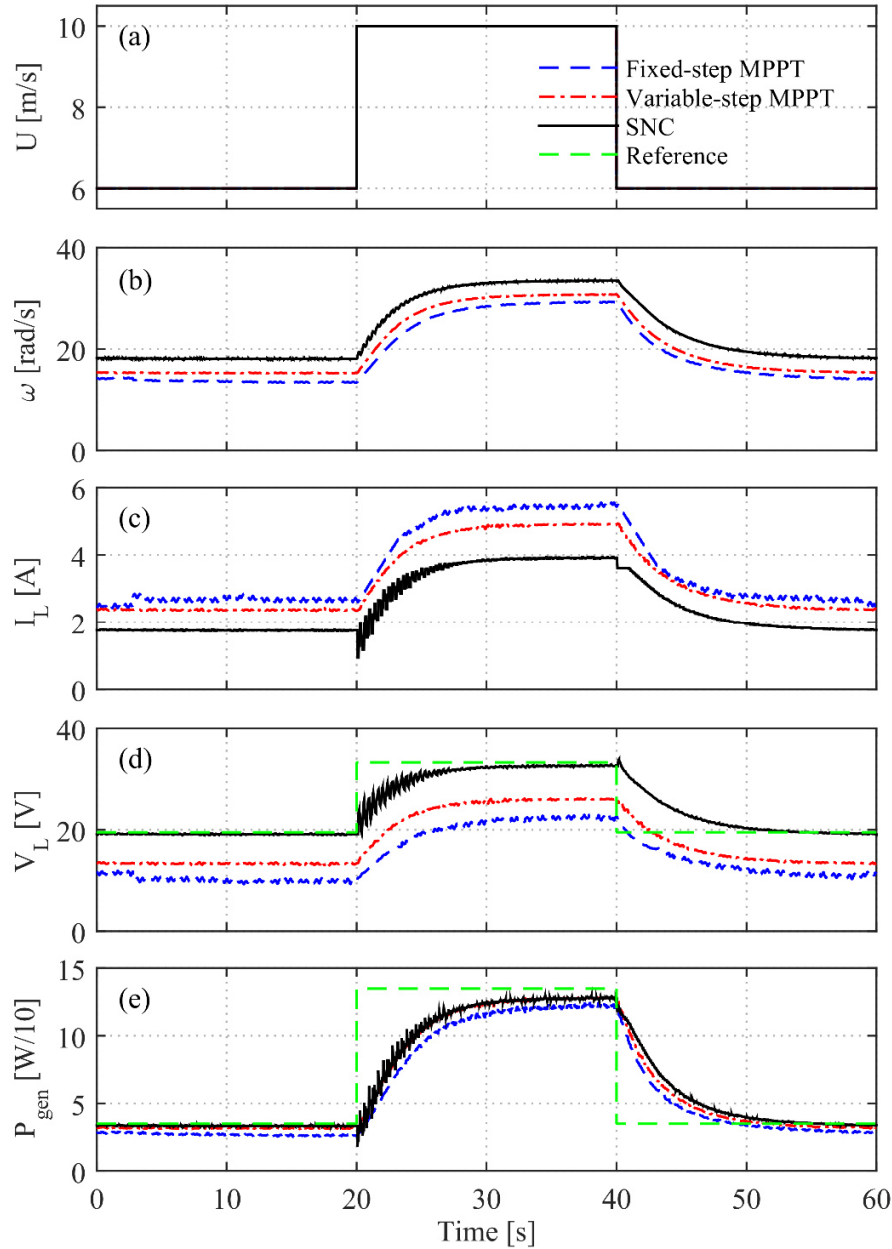


Figure 6.39: Step wind profile (a); dynamic responses of the load coefficient (b), rotor velocity (c), and generator power (d) for HIL simulations.

The resulting energy efficiencies for the fixed- and variable-step MPPT, and the SNC are 86.23%, 85.20%, and 94.34%, respectively. When the small differences between the responses are considered, it is remarkable that the SNC outperforms the MPPT algorithms

substantially, which implies that operating the system at reference conditions (i.e., through model-based methods) may lead to significant gains in energy generation.

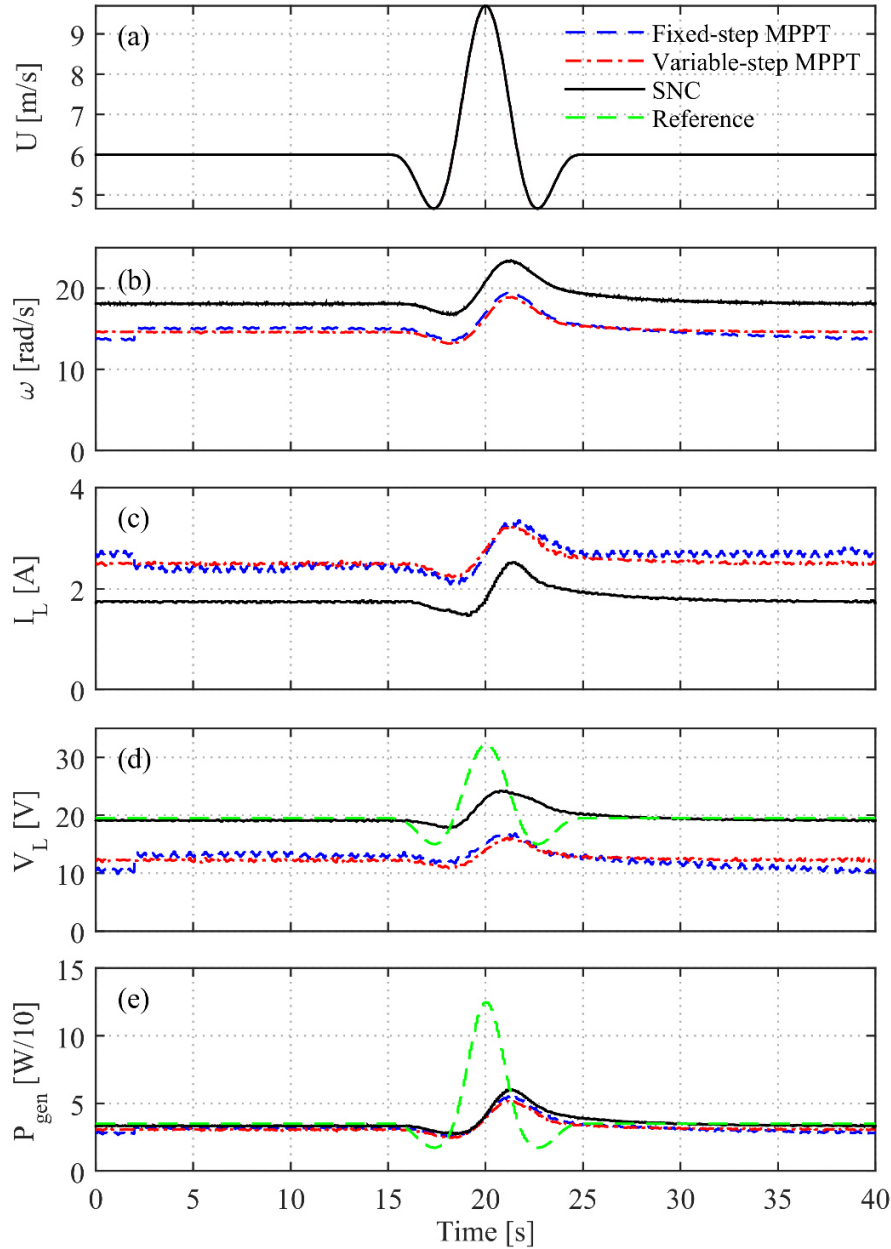


Figure 6.40: Wind gust profile (a); dynamic responses of the load coefficient (b), rotor velocity (c), and generator power (d) for HIL simulations.

Lastly, experiments for the real wind profile (Figure 6.41a) are conducted and the responses are depicted in Figure 6.41. First of all, it is seen that the rotor velocity saturates at about 40 rad/s (see Figure 6.41b), which is the maximum limit for the rotor velocity for HIL

simulations because the maximum velocity of the electrical motor is 4000 rpm, which corresponds to about 400 rpm (*ca* 40 rad/s) at the generator side; furthermore, this limitation saturates the load current, load voltage and power output variables as well, as seen in Figs. 6.41c, d, and e.

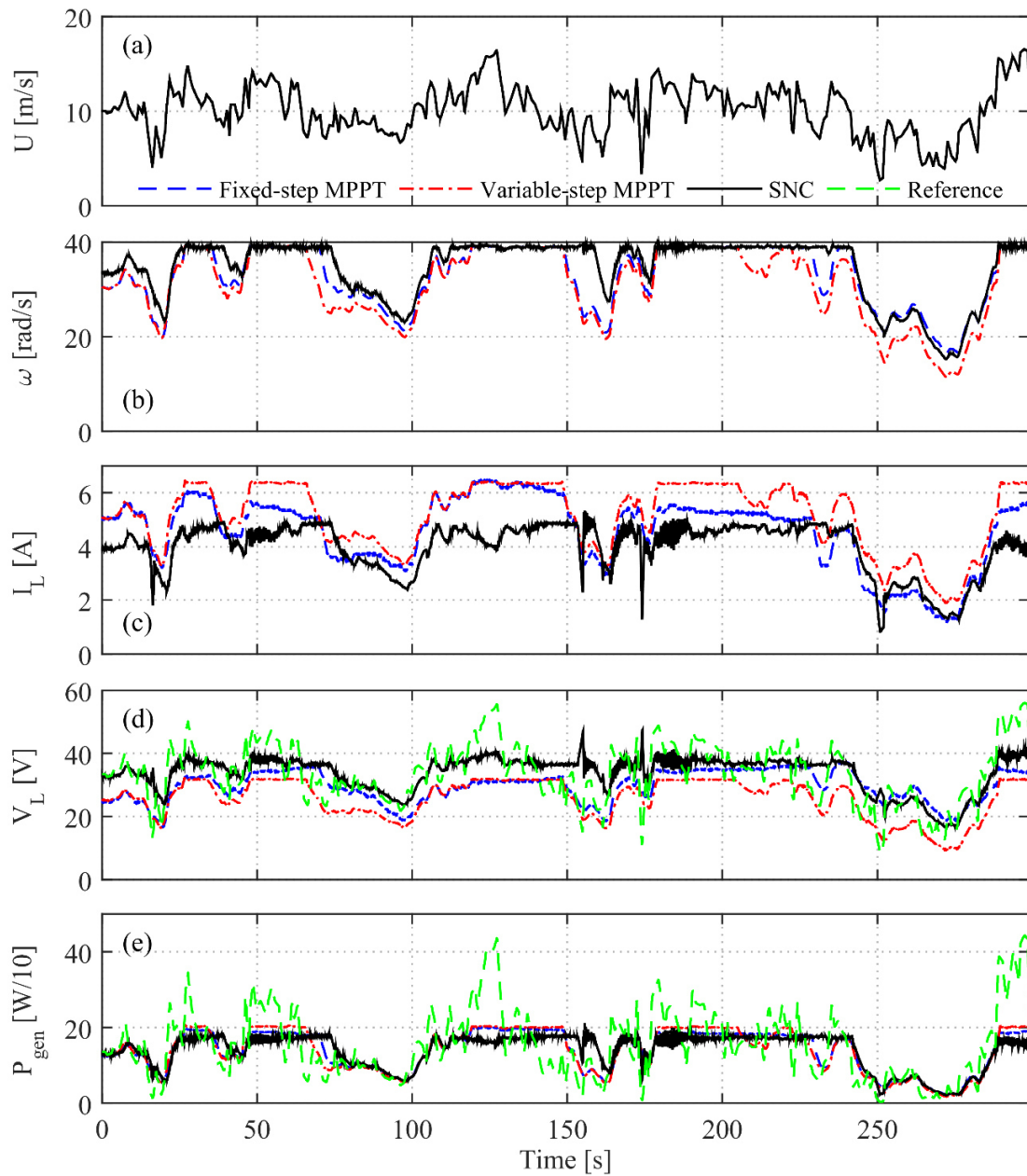


Figure 6.41: Real wind profile (a); dynamic responses of the load coefficient (b), rotor velocity (c), and generator power (d) for HIL simulations.

Since the MPPT algorithms operate the system at higher current – lower voltage operating conditions than the reference conditions, which should be tracked for the SNC, the rotor velocity, which is correlated to the load voltage, is generally lower for the MPPT controllers than the SNC; therefore, the SNC is affected by these saturations more than the MPPT methods. The power outputs for the MPPT controllers exceed the power output of the SNC during the saturation occasions (e.g., for $120 < t < 150$ s), as shown in Figure 6.41e. In addition, for the SNC, there are certain fluctuations in the I_L as well as in the resulting V_L and P_{gen} (see Figs. 6.41b, c, and d) particularly when the wind velocity changes rapidly in a wide range, e.g., for $150 < t < 175$ s.

At the end of the experiments, the fixed-step MPPT, the variable-step MPPT, and the SNC convert 90.30%, 90.52%, and 90.04% available energy into electrical energy, respectively. In accordance with this outcome, one can suggest that the discrepancies between the control algorithms are not significant in the long run. Nevertheless, it is obvious that rotor velocity saturation has a consequential impact on the performance of the SNC.

The energy efficiency results of the MPPT and SNC algorithms for the step wind, wind gust, and real wind inputs are tabularized in Table 6.4. The results obtained from the experiments yield the following observations. First, the experimental results proves that all of the controllers perform successfully for the step wind, wind gust, and real wind profiles. Furthermore, the dynamic responses of the controllers for HIL simulations are not significantly distinct from the responses for electromechanical simulations, and electromechanical simulations can be used to evaluate the performance of the VAWT system including the non-ideal generator and power electronics components as well as to design controllers accordingly and test their performance.

Second, the MPC-mimicking SNC outperforms the MPPT algorithms substantially for the step wind and wind gust profiles. On the other hand, for the real wind case, the energy efficiencies for all controllers are within a range of 0.5%. Moreover, the operation conditions for the model-based SNC are specified, while the incremental MPPT controllers, especially the fixed-step version, may diverge from the MPP due to error accumulation. Thus, the SNC can be deemed a more reliable and efficient method than the MPPT methods.

Third, among the fixed-step and variable-step MPPT algorithms, the variable-step MPPT is observed to be more stable since its responses are insensitive to wind transients, while the responses of the fixed-step algorithm are very sensitive to wind transients. Furthermore, the variable-step MPPT overcomes the fixed-step MPPT in terms of energy generation for the step and real wind cases, while the energy efficiency of the fixed-step MPPT is only about 1% greater than the variable-step MPPT's for the wind gust case. Thus, the variable-step MPPT can be preferred over the fixed-step MPPT.

Last, the MPPT techniques require neither the power coefficient curve of the turbine nor wind velocity measurement, as distinct from the SNC; therefore, they are more applicable than the SNC. Moreover, the operation of the variable-step MPPT is almost as stable as the SNC. Thus, although the SNC is found to be a more efficient method, the variable-step MPPT is an attractive option for small-scale VAWT applications.

Table 6.4: Energy efficiency results for HIL simulations.

Control \ Wind	Fixed-step MPPT	Variable-step MPPT	SNC
Step Wind	84.4068%	92.3979%	95.3387%
Wind Gust	86.2349%	85.1954%	94.3375%
Real Wind	90.3000%	90.5198%	90.0434%

6.4. Effect of Measurement Noise

In addition to the real responses of the hardware components rather than approximations, the HIL simulation contains inevitable measurement noises that are filtered out through low pass filters but still may affect control performance. Thus, in order to mimic this effect in the electromechanical simulation, a white Gaussian noise with a seed of 1 and an impedance of 0.05 (i.e., using `wgn` function of Matlab) is added to the load voltage signal, which is the feedback variable of the controllers except the MPC, and the performances of the MPPT and SNC algorithms are analyzed for the step wind, wind gust and real wind profiles through electromechanical simulations with noise.

Figure 6.42 illustrates the step wind performances of the controllers. It is seen that none of the controllers is significantly affected by the noise, albeit the visible jitters; moreover, the noise apparently improves the performance of the fixed-step MPPT by preventing it from being stuck at an operating point other than the MPP, which occurs in the electromechanical simulations without noise. Additionally, the P_{gen} responses in Figure 6.42e are very similar to the ones in Figure 6.39e. As a result, the fixed- and variable-step MPPT and the SNC harvest 93.38%, 91.44%, and 93.76%, respectively; namely, the fixed-step MPPT outperforms the variable-step algorithm and demonstrates a very similar performance to the SNC.

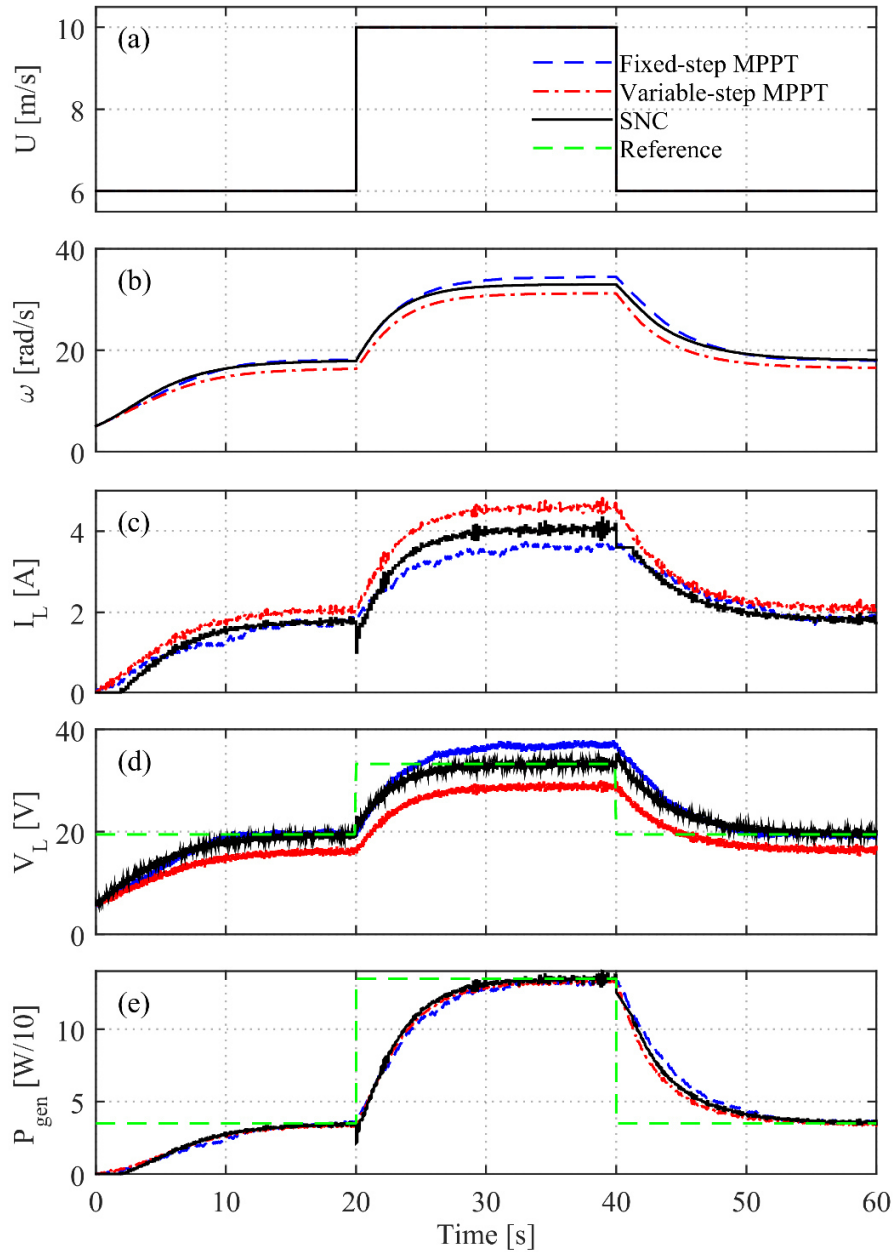


Figure 6.42: Step wind profile (a); dynamic responses of the load coefficient (b), rotor velocity (c), and generator power (d) for electromechanical simulations with noise.

The responses of the controllers for the wind gust are depicted in Figure 6.43. Figure 6.43c shows that the variable-step MPPT and the SNC is more robust to the noise in the load voltage than the fixed-step MPPT, for which there are large fluctuations in the I_L . Notwithstanding, the power output responses are quite similar to each other, as shown in

Figure 6.43e. The resulting energy efficiencies are 79.97%, 79.48%, and 81.77% for the fixed-step, variable-step MPPT methods and the SNC, respectively.

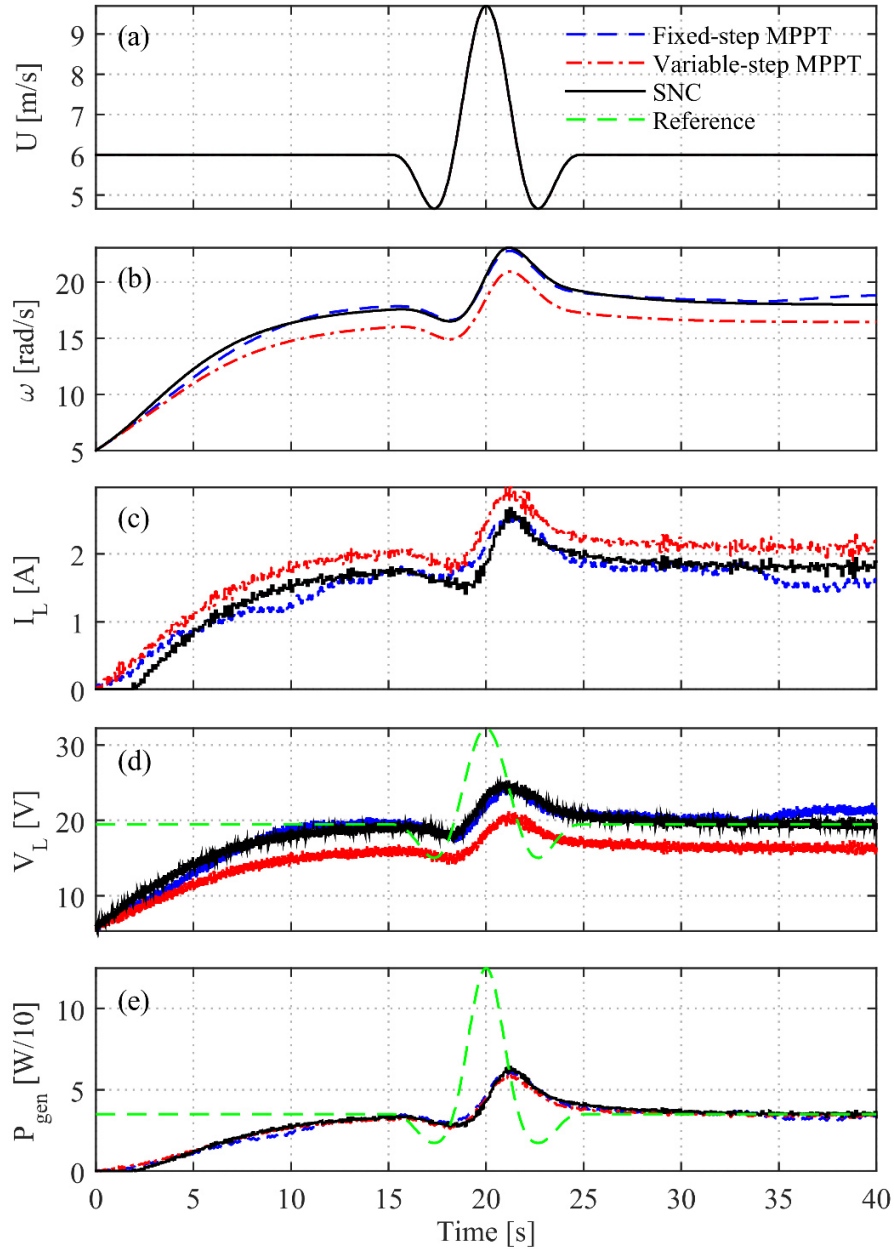


Figure 6.43: Wind gust profile (a); dynamic responses of the load coefficient (b), rotor velocity (c), and generator power (d) for electromechanical simulations with noise.

Lastly, the controllers are tested for the real wind in the presence of load voltage noise, and their responses are demonstrated in Figure 6.44. For the SNC, the I_L fluctuates substantially, inducing fluctuations in the V_L and the P_{gen} as well, around $t = 125$ s and $t =$

300 s because of quick switching among operation regions. This result is interesting since this situation occurs in HIL simulations (see Figure 6.41) but not in electromechanical simulations without noise (see Figure 6.37). Thus, it can be concluded that this behavior is caused by the combined effect of measurement noise and fast wind dynamics.

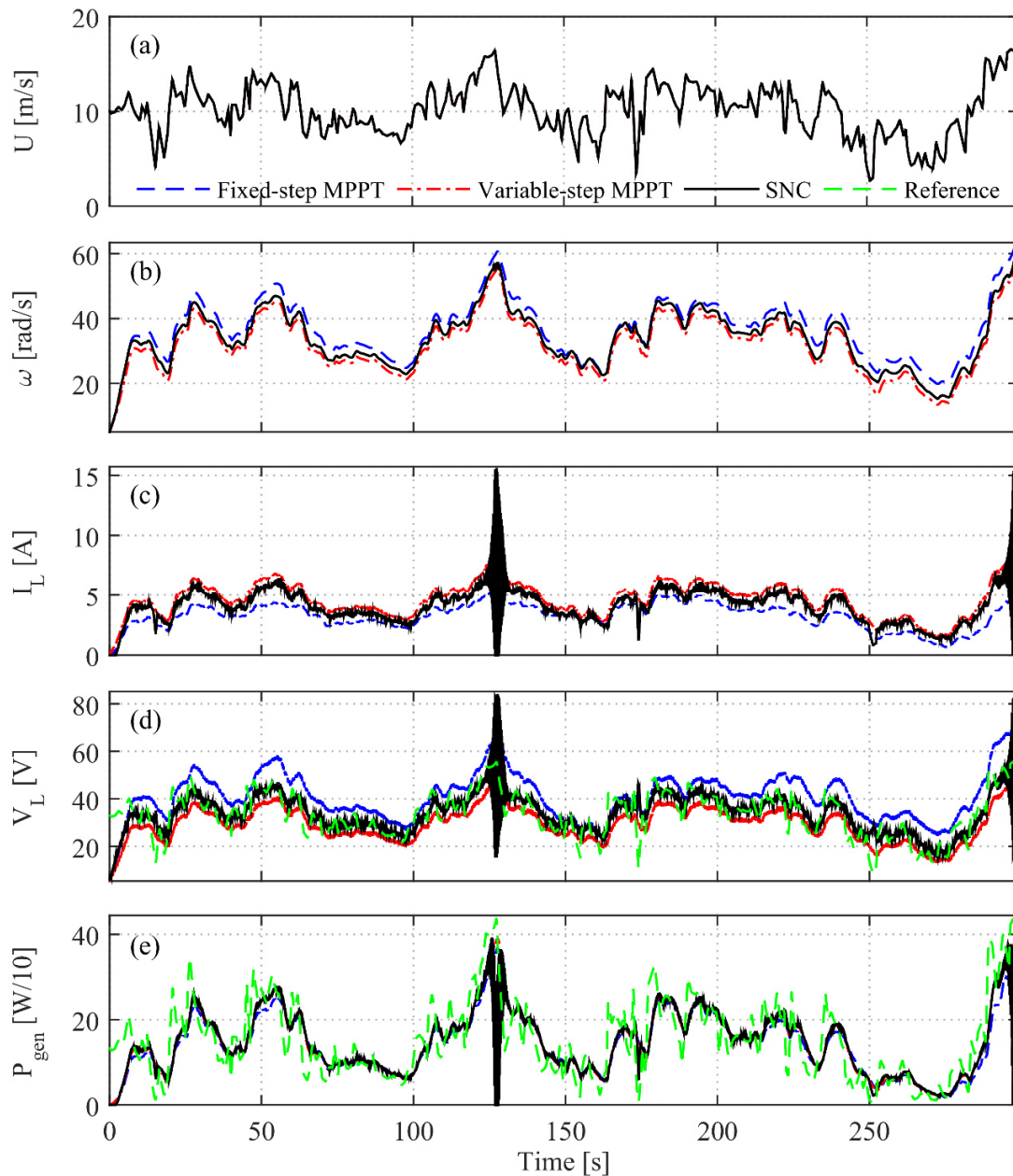


Figure 6.44: Real wind profile (a); dynamic responses of the load coefficient (b), rotor velocity (c), and generator power (d) for electromechanical simulations with noise.

Apart from that, the responses are quite similar to the responses for the electromechanical simulation without noise that are shown in Figure 6.37. At the end of these simulations, the fixed- and variable-step MPPT controllers and the SNC convert 92.27%, 95.63%, and 94.68% of the available energy into electricity, respectively. It is seen that the variable-step MPPT outperforms the fixed-step MPPT significantly in the long run despite the fact that the fixed-step MPPT is advantageous for the other cases, which also suggests that the variable-step algorithm is more reliable for realistic conditions. On the other hand, the fluctuations due to the noise on the load voltage signal and fast wind dynamics deteriorate the performance of the SNC significantly and lead to a slightly less efficient energy generation of the SNC compared to the variable-step MPPT. The energy efficiency results for all cases are summarized in Table 6.5.

Table 6.5: Energy efficiency results for electromechanical simulations with noise.

Control \ Wind	Fixed-step MPPT	Variable-step MPPT	SNC
Step Wind	93.3773%	91.4395%	93.7630%
Wind Gust	79.9702%	79.4752%	81.7722%
Real Wind	92.2692%	95.6264%	94.6815%

6.5. Effect of Power Coefficient Oscillations and Inertia

Results of CFD simulations show that the power coefficient, from which the wind torque is estimated in simple dynamic, electromechanical, and HIL simulations, has non-negligible oscillations. Although it is shown that C_P oscillations do not affect the dynamical performance of the VAWT system with an idealized electrical system considerably, see Figure 6.24, they may possess an impact on the VAWT system with non-ideal hardware components. Furthermore, the moment of inertia of the rotor plays a crucial role in filtering out these oscillations and reducing their impact by the virtue of the first-order dynamics of the rotor. Thus, here, the effect of the inertia, J , is observed in the presence of C_P oscillations through electromechanical simulations. The amplitude of C_P oscillations is dependent on the tip-speed ratio, λ , (see Figure 6.23) while the frequency is the triple of the rotor velocity, ω , and the resulting $C_P(\lambda, t)$ is obtained from (5.14).

For this purpose, electromechanical simulations, in which load voltage measurement is assumed to be noise-free, are run for $J = \{0.2, 1, 5\}$ kg-m² for a 120-second step wind (Figure 6.45a), and the SNC is employed as the controller. Figure 6.45 shows the rotor velocity, load current, load voltage, and power output responses for each J value.

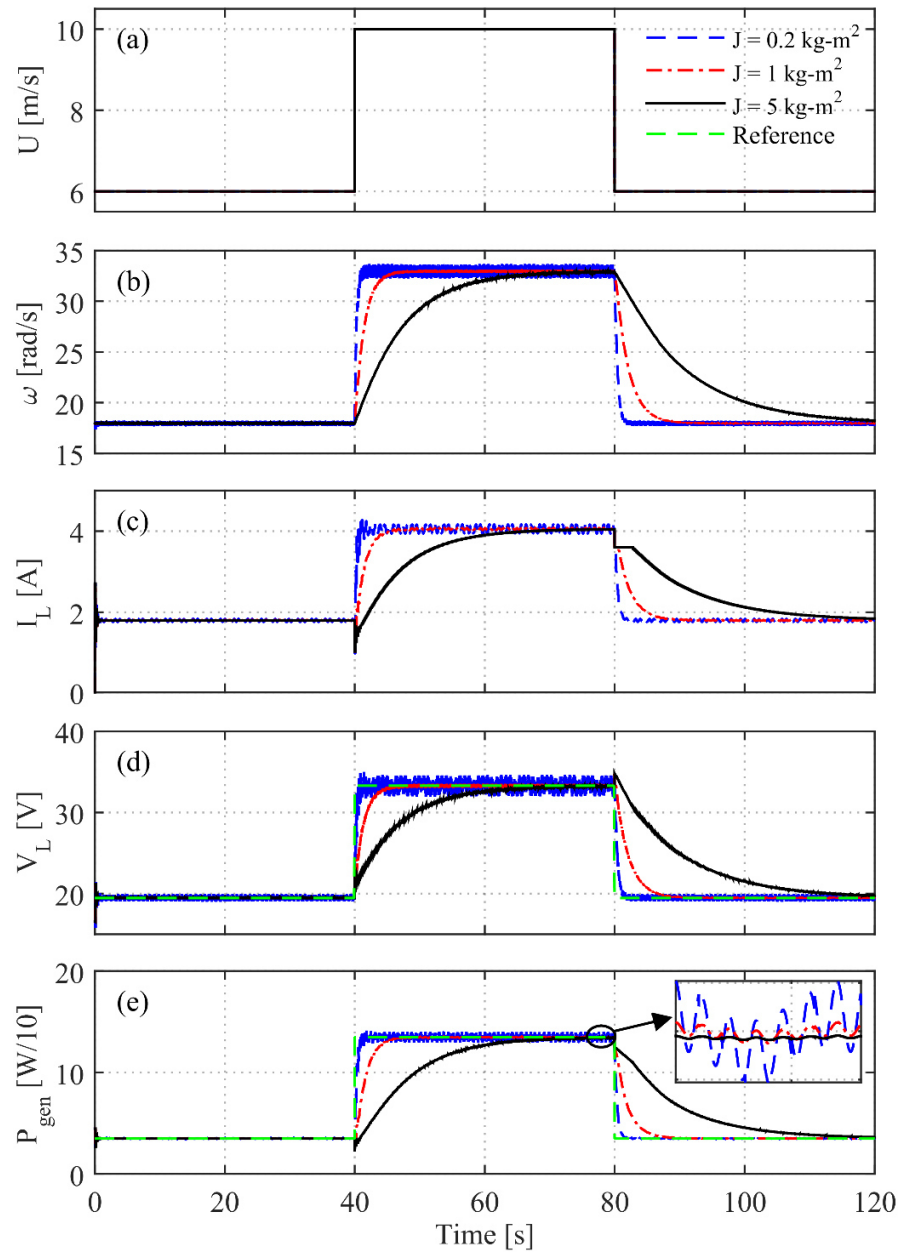


Figure 6.45: Responses of the SNC for different values of the inertia, J , in the presence of C_P oscillations.

First of all, for all J values, the SNC perform successfully which shows that the SNC is applicable for VAWTs with different mechanical configurations without a need for retuning. Second, the settling time of the dynamical system is proportional to the J , as expected. Third, there are significant jitters in all variables for the case in which $J = 0.2 \text{ kg-m}^2$, as shown in Figs. 6.45b, c, d, and e. C_P oscillations lead to ω oscillations that induces oscillations in the V_L due to the correlation between voltage and velocity, and eventually oscillations occur in the I_L , which is calculated from the V_L as well as affects the voltage drop; therefore, the V_L oscillations are apparently more remarkable than the others.

The subfigure in Figure 6.45e shows the zoomed in views of the power outputs for $79 < t < 80 \text{ s}$. Clearly, the amplitude of the oscillations are very large for $J = 0.2 \text{ kg-m}^2$, while the oscillations are nearly invisible for $J = 5 \text{ kg-m}^2$. This result proves that the moment of inertia of the rotor acts as a low-pass filter by filtering out the oscillations with high frequency. Furthermore, at the end of two minutes, the rotors with $J = \{0.2, 1, 5\} \text{ kg-m}^2$ capture $\{99.9602\%, 99.9728\%, 99.9745\%\}$ of the available energy; namely, the energy yield enhances, albeit slightly, as the J increases for this case, despite the fact that the power output tracks the MPP almost perfectly for the smallest J .

6.6. Effect of Inertia on Steady-periodic Performance

Although a perfect sinusoidal wind is not realistic, wind can demonstrate characteristics similar to periodic signals. Furthermore, the moment of inertia of the rotor may possess a significant impact on the steady-periodic performance of the VAWT, as in the C_P oscillations case. Hence, here, the steady-periodic performances of VAWTs with different inertia values are investigated for a sinusoidal wind input. 30-second electromechanical simulations, in which neither C_P oscillations nor noises prevail, are carried out for a sinusoidal wind profile with a period of 10 s, a mean of 6 m/s, and an amplitude of 2 m/s (i.e., $\pm 33\%$ fluctuation), see Figure 6.46a, for. Again, rotors with $J = \{0.2, 1, 5\} \text{ kg-m}^2$ are considered, and the SNC is employed as the controller. The actual and reference energy outputs (E_{gen} and E_{ref}) are calculated within a 10-second moving window to attain the energy efficiency in the last period.

Figure 6.46 depicts the results of this study. Since the system seemingly reaches to a steady-periodic-state, the responses only in the last period of the wind velocity are shown in the figure. The responses show that the moment of inertia of the rotor filters out the high frequency components due to wind dynamics as well owing to the first-order dynamics of the rotor.

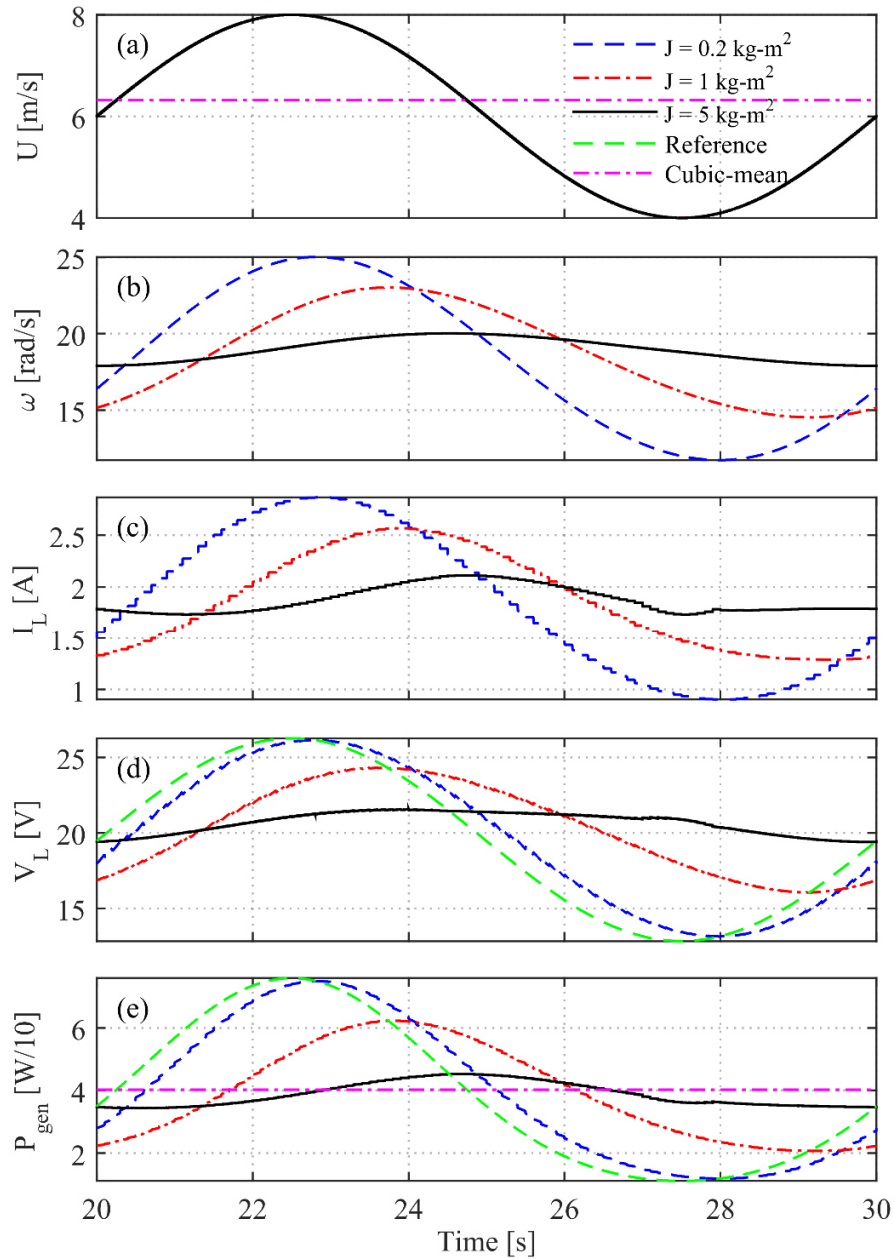


Figure 6.46: Responses of the SNC for different values of the inertia, J , for sinusoidal wind profile.

According to Figure 6.46e, the P_{gen} for $J = 2 \text{ kg-m}^2$ tracks the reference power output with a little phase delay; while, the P_{gen} for $J = 1 \text{ kg-m}^2$ fluctuate within a narrower range with a larger phase delay corresponding to *ca* 1.5 s; on the other hand, the P_{gen} for $J = 5 \text{ kg-m}^2$ is almost steady, i.e., fluctuates with a very small amplitude, due to the filtering effect of the inertia of the rotor.

The resulting energy efficiencies are 99.9580%, 99.1867%, and 98.4653% for the rotors with $J = \{0.2, 1, 5\} \text{ kg-m}^2$, respectively; namely, the energy output of the VAWT decreases as the inertia increases for this case, in contrast to the outcome of the C_P oscillations case. This result is caused by the fact that the P_{gen} converges to the mean value of the reference power output (i.e., 39.25 W) as the J increases and filters out the fluctuations; however, the power output is proportional to the cube of the wind velocity, and therefore the available wind power (i.e., 40.28 W) that is obtained from the cubic mean of the wind velocity (i.e., 6.32 m/s) is actually greater than the mean value of the reference power output. Thus, it can be concluded that the energy efficiency of the VAWT deteriorates when the wind dynamics is faster than the rotor dynamics if it is not controlled accordingly, which is consistent with the results reported by McIntosh et al. [40].

Chapter 7

CONCLUSIONS & FUTURE WORK

7.1. Conclusions

This thesis presents a framework for the assessment of the performance of a small-scale VAWT system that includes a three-straight-bladed, high-solidity rotor, electromechanical and power electronics components, and controller. Within this framework, we use a time-dependent, two-dimensional CFD model for a height-normalized, three-straight-bladed VAWT rotor with high solidity and a HIL test-bed including the actual electromechanical and power electronics components.

The CFD model is coupled with the dynamics of the rotor in order to calculate the transient angular velocity of the rotor for a given generator load and validated with measurements from an experimental VAWT. The CFD modeling approach is used to obtain the flow around the rotor and the stresses on the blades. The $k-\epsilon$ turbulence model is used to approximate unsteady Reynolds-averaged Navier-Stokes equations. The coupled CFD/rotor dynamics model provides an environment to analyze the realistic transient behavior of the VAWT rotor subject to the generator load manipulated by the control algorithm and the inertia of the rotor.

CFD simulations are performed for steady wind flow to study the aerodynamic performance and flow physics of the VAWT which yield the following observations. First, quasi-steady power coefficient curves are obtained against the tip-speed ratio for a range of steady wind velocities, and it is shown that the power coefficient curve does not change with the wind velocity considerably, therefore the aerodynamic performance of the VAWT can be represented by a single power coefficient curve. Second, according to simulations, the

presence of the shaft at the rotor center does not have a significant impact on the flow distribution and on the rotor velocity. Third, local angle of attack is calculated based on the local velocity field, and compared with the geometric angle of attack; the power coefficient values tend to follow the same trend with the local angle of attack rather than the geometric angle of attack.

Owing to the coupled dynamic modeling approach, the transient response of the VAWT is obtained for standard wind gusts through CFD simulations. Instantaneous power coefficient is oscillatory due to the oscillations in the wind torque. However, the oscillations in the generator torque are much smaller than the wind torque, about $1/100^{\text{th}}$. A variable-step control strategy, i.e., proportional control, allows more than 95% of the energy in the gust to be captured. Average of the transient power coefficients peaks at a smaller tip-speed ratio for wind gusts than steady winds. Instantaneous power coefficients make hysteresis lops in counterclockwise direction versus the local angle of attack calculated from the local velocity field. The results show that the proposed model provides a reliable and effective approach for system-level design and analysis of VAWTs.

CFD simulations take an excessive amount of computation time, hence a simple dynamic simulation is developed using the tip-speed ratio – power coefficient characteristics obtained from CFD simulations in order to design and test control algorithms. A comparison between the results of CFD and simple dynamic simulations shows that the simple dynamic simulation is sufficiently accurate to evaluate the dynamic performance of the VAWT system including the controller.

Model-free, wind speed sensorless fixed- and variable-step hill-climb search MPPT algorithms, a model predictive control for maximization of energy generation subject to electrical limitations of the system, and an MPC-mimicking simple nonlinear control are designed and tested through simple dynamic simulations. The performances of the controllers are compared for step wind, wind gust and real wind profiles. Simulation results show that the MPC and the SNC outperform the MPPT algorithms in terms of energy generation for all wind types. Thus, it can be said that maximizing the instantaneous power does not mean maximizing the energy generation, and the energy output can be enhanced by allowing deviations from the maximum power instantaneously for future gains in energy generation.

Moreover, the proposed SNC demonstrates a successful performance in the sense of MPC-mimicking.

The CFD and simple dynamic simulations are based on an ideal electromechanical energy conversion assumption. However, the real characteristics of the generator and power electronics components that convert the mechanical energy of the rotor into DC power are, in fact, far from being ideal. Thus, in order to observe the impact of the actual electromechanical and power electronics components on the power characteristics of the VAWT system, we employ the HIL test-bed developed in [16,19], in which an electrical motor emulates the VAWT rotor based on a power coefficient curve obtained from CFD simulations. Furthermore, a simple electromechanical model, which is the simplified DC equivalent of the HIL test-bed, is developed and validated through experimental data. According to simulation results, the impact of the characteristics of the generator and power electronics components reduces the maximum power point and shifts it higher rotor velocities, which implies that the most dominant loss on this system is the resistive loss that is proportional to the square of the current. In other words, the generator and power electronics components have a profound effect on the overall power output and efficiency of the VAWT system. Hence, the electromechanical simulation is used to redesign and tune the fixed- and variable-step MPPT, SNC and MPC methods accordingly.

Since the MPC is a computationally expensive method and cannot operate in real-time in this case, first, the control algorithms are tested through electromechanical simulations. Then, HIL simulations are conducted to test the performance of the VAWT system including actual electromechanical and power electronics components and real-time control (excluding the MPC). Results show that the controllers perform satisfactorily for step wind, wind gust, and real wind inputs, and the experimental results for the MPPT and SNC algorithms are similar to the electromechanical simulation results which means that the electromechanical model is a reliable tool to design and evaluate control algorithms for actual VAWT systems. Additionally, the influence of measurement noise that inevitably prevails in HIL simulations is investigated by adding a white Gaussian noise to the voltage signal in electromechanical simulations, and it is seen that the noise is useful to attain a more realistic analogy of the HIL simulation.

The moment of inertia of the rotor plays an important role on the performance of the VAWT since it filters out the oscillations in the system response by the virtue of the first-order dynamics of the rotor. Hence, its effect on the performance in the presence of power coefficient oscillations is analyzed through electromechanical simulations. According to results, the energy efficiency improves as the moment of inertia increases despite almost perfect tracking of wind dynamics when the inertia is small. Moreover, the impact of the inertia on the steady-periodic performance, i.e., for a periodic wind input, is studied, and it is shown that the energy efficiency of the VAWT deteriorates when the wind dynamics is faster than the rotor dynamics if it is not controlled accordingly.

7.2. Future Work

Further research into the following subjects might be interesting:

- Implementing control designs on the experimental VAWT system.
- Deriving the exact solution of the optimal control problem so that MPC can be implemented in real-time.
- Using a pseudo-spectral collocation method to solve the optimal control problem for MPC so that the prediction horizon can be extended.
- Investigating the interaction between the rotor and wind dynamics further, determining the optimal inertia for a given wind condition, and trying inertia control in simple dynamic or electromechanical simulations.
- Controlling pitch angle of the blades in the CFD simulation and determining the optimal pitch angle trajectory of a blade throughout a revolution.

BIBLIOGRAPHY

- [1] Sahin, A. D. (2004). Progress and recent trends in wind energy. *Progress in Energy and Combustion Science*, 30(5), 501-543.
- [2] Herbert, G. J., Iniyar, S., Sreevalsan, E., & Rajapandian, S. (2007). A review of wind energy technologies. *Renewable and Sustainable Energy Reviews*, 11(6), 1117-1145.
- [3] Deal, W. F. (2010). Wind Power: An Emerging Energy Resource. *Technology and Engineering Teacher*, 70(1), 9-15.
- [4] Kaldellis, J. K., & Zafirakis, D. (2011). The wind energy (r) evolution: A short review of a long history. *Renewable Energy*, 36(7), 1887-1901.
- [5] Leung, D. Y., & Yang, Y. (2012). Wind energy development and its environmental impact: A review. *Renewable and Sustainable Energy Reviews*, 16(1), 1031-1039.
- [6] Da Rosa, A.V. (2013). *Fundamentals of Renewable Energy Processes*, Academic Press.
- [7] Manwell, J. F., McGowan, J. G., & Rogers, A. L. (2010). *Wind energy explained: theory, design and application*. John Wiley & Sons.
- [8] Eriksson, S., Bernhoff, H., & Leijon, M. (2008). Evaluation of different turbine concepts for wind power. *Renewable and Sustainable Energy Reviews*, 12(5), 1419-1434.
- [9] Tummala, A., Velamati, R. K., Sinha, D. K., Indraja, V., & Krishna, V. H. (2016). A review on small scale wind turbines. *Renewable and Sustainable Energy Reviews*, 56, 1351-1371.
- [10] Riegler, H. (2003). HAWT versus VAWT: Small VAWTs find a clear niche. *Refocus*, 4(4), 44-46.
- [11] Pope, K., Dincer, I., & Naterer, G. F. (2010). Energy and exergy efficiency comparison of horizontal and vertical axis wind turbines. *Renewable Energy*, 35(9), 2102-2113.
- [12] Sutherland, H. J., Berg, D. E., & Ashwill, T. D. (2012). A retrospective of VAWT technology. *SAND2012-0304*. Sandia National Laboratories.

- [13] Bhutta, M. M. A., Hayat, N., Farooq, A. U., Ali, Z., Jamil, S. R., & Hussain, Z. (2012). Vertical axis wind turbine—A review of various configurations and design techniques. *Renewable and Sustainable Energy Reviews*, 16(4), 1926-1939.
- [14] Ishugah, T. F., Li, Y., Wang, R. Z., & Kiplagat, J. K. (2014). Advances in wind energy resource exploitation in urban environment: A review. *Renewable and Sustainable Energy Reviews*, 37, 613-626.
- [15] Hau, E. and von Renouard, H. (2013). *Wind Turbines: Fundamentals, Technologies, Application, Economics*. SpringerLink: Bücher, Springer Berlin Heidelberg.
- [16] Sancar, U. (2015). *Hardware-in-the-loop Simulations and Control Designs for a Vertical Axis Wind Turbine* (Master's thesis). Sabanci University.
- [17] Islam, M., Ting, D. S. K., & Fartaj, A. (2008). Aerodynamic models for Darrieus-type straight-bladed vertical axis wind turbines. *Renewable and Sustainable Energy Reviews*, 12(4), 1087-1109.
- [18] Jacobson, M. Z., & Archer, C. L. (2012). Saturation wind power potential and its implications for wind energy. *Proceedings of the National Academy of Sciences*, 109(39), 15679-15684.
- [19] Sancar, U., Onol, A.O., Onat, A., & Yesilyurt, S. (2015, November). Hardware-in-the-loop simulations and control design for small vertical axis wind turbines. In *2015 XXV International Conference on Information, Communication and Automation Technologies (ICAT)*. IEEE.
- [20] Sheldahl, R. E., & Klimas, P. C. (1981). Aerodynamic characteristics of seven symmetrical airfoil sections through 180-degree angle of attack for use in aerodynamic analysis of vertical axis wind turbines. *SAND-80-2114*. Sandia National Laboratories.
- [21] Sheldahl, R. E. (1981). Comparison of field and wind-tunnel Darrieus wind-turbine data. *Journal of Energy*, 5(4), 254-256.
- [22] Ashwill, T. D. (1990). Initial structural response measurements and model validation for the Sandia 34-meter VAWT test bed. *SAND88-0633*. Sandia National Laboratories.
- [23] Jin, X., Zhao, G., Gao, K., & Ju, W. (2015). Darrieus vertical axis wind turbine: Basic research methods. *Renewable and Sustainable Energy Reviews*, 42, 212-225.

- [24] Chen, J., Yang, H., Yang, M., Xu, H., & Hu, Z. (2015). A comprehensive review of the theoretical approaches for the airfoil design of lift-type vertical axis wind turbine. *Renewable and Sustainable Energy Reviews*, 51, 1709-1720.
- [25] Ferreira, C. S., & Geurts, B. (2014). Aerofoil optimization for vertical-axis wind turbines. *Wind Energy*, 18(8), 1371-1385.
- [26] Ragni, D., Ferreira, C. S., & Barone, M. (2014). Experimental and numerical investigation of an optimized airfoil for vertical axis wind turbines. In *AIAA SciTech: 32nd ASME Wind Energy Symposium* (pp. 1-10).
- [27] Vassberg, J. C. (2005, January). Revisiting the Vertical-Axis Wind-Turbine Design using Advanced Computational Fluid Dynamics. In *43rd AIAA Aerospace Sciences Meeting and Exhibit, Reno, Nevada*.
- [28] Howell, R., Qin, N., Edwards, J., & Durrani, N. (2010). Wind tunnel and numerical study of a small vertical axis wind turbine. *Renewable Energy*, 35(2), 412-422.
- [29] McLaren, K., Tullis, S., & Ziada, S. (2012). Computational fluid dynamics simulation of the aerodynamics of a high solidity, small-scale vertical axis wind turbine. *Wind Energy*, 15(3), 349-361.
- [30] Li, C., Zhu, S., Xu, Y. L., & Xiao, Y. (2013). 2.5 D large eddy simulation of vertical axis wind turbine in consideration of high angle of attack flow. *Renewable Energy*, 51, 317- 330.
- [31] Almohammadi, K. M., Ingham, D. B., Ma, L., & Pourkashanian, M. (2015). 2-D-CFD Analysis of the Effect of Trailing Edge Shape on the Performance of a Straight-Blade Vertical Axis Wind Turbine. *Sustainable Energy, IEEE Transactions on*, 6(1), 228-235.
- [32] Scheurich, F., & Brown, R. E. (2013). Modelling the aerodynamics of vertical-axis wind turbines in unsteady wind conditions. *Wind Energy*, 16(1), 91-107.
- [33] Kooiman, S., & Tullis, S. (2010). Response of a vertical axis wind turbine to time varying wind conditions found within the urban environment. *Wind Engineering*, 34(4), 389-402.
- [34] Danao, L. A., Eboibi, O., & Howell, R. (2013). An experimental investigation into the influence of unsteady wind on the performance of a vertical axis wind turbine. *Applied Energy*, 107, 403-411. 23.

- [35] Danao, L. A., Edwards, J., Eboibi, O., & Howell, R. (2014). A numerical investigation into the influence of unsteady wind on the performance and aerodynamics of a vertical axis wind turbine. *Applied Energy*, 116, 111-124. 24.
- [36] Wekesa, D. W., Wang, C., Wei, Y., & Danao, L. A. M. (2014). Influence of operating conditions on unsteady wind performance of vertical axis wind turbines operating within a fluctuating free-stream: A numerical study. *Journal of Wind Engineering and Industrial Aerodynamics*, 135, 76-89. 25.
- [37] Wekesa, D. W., Wang, C., Wei, Y., Kamau, J. N., & Danao, L. A. M. (2015). A numerical analysis of unsteady inflow wind for site specific vertical axis wind turbine: A case study for Marsabit and Garissa in Kenya. *Renewable Energy*, 76, 648-661. 26.
- [38] Bausas, M. D., & Danao, L. A. M. (2015). The aerodynamics of a camber-bladed vertical axis wind turbine in unsteady wind. *Energy*, 93, 1155-1164. 27.
- [39] Hara, Y., Hara, K., & Hayashi, T. (2012). Moment of inertia dependence of vertical axis wind turbines in pulsating winds. *International Journal of Rotating Machinery*, 2012. 28.
- [40] McIntosh, S. C., Babinsky, H., & Bertenyi, T. (2007, January). Optimizing the energy output of vertical axis wind turbines for fluctuating wind conditions. In *45th AIAA Aerospace Sciences Meeting and Exhibit, Reno, Nevada*.
- [41] McIntosh, S. C., Babinsky, H., & Bertenyi, T. (2008, January). Unsteady power output of vertical axis wind turbines operating within a fluctuating free-stream. In *46th AIAA Aerospace Sciences Meeting and Exhibit, Reno, Nevada*.
- [42] Salle, S. D. L., Reardon, D., Leithead, W. E., & Grimble, M. J. (1990). Review of wind turbine control. *International Journal of Control*, 52(6), 1295-1310.
- [43] Johnson, K. E., Pao, L. Y., Balas, M. J., & Fingersh, L. J. (2006). Control of variable-speed wind turbines: standard and adaptive techniques for maximizing energy capture. *IEEE Control Systems*, 26(3), 70-81.
- [44] Koutroulis, E., & Kalaitzakis, K. (2006). Design of a maximum power tracking system for wind-energy-conversion applications. *IEEE Transactions on Industrial Electronics*, 53(2), 486-494.
- [45] Hui, J., & Bakhshai, A. (2008, June). A new adaptive control algorithm for maximum power point tracking for wind energy conversion systems. In *2008 IEEE Power Electronics Specialists Conference* (pp. 4003-4007). IEEE.

- [46] Barakati, S. M., Kazerani, M., & Aplevich, J. D. (2009). Maximum power tracking control for a wind turbine system including a matrix converter. *IEEE Transactions on Energy Conversion*, 24(3), 705-713.
- [47] Kazmi, S. M. R., Goto, H., Guo, H. J., & Ichinokura, O. (2011). A novel algorithm for fast and efficient speed-sensorless maximum power point tracking in wind energy conversion systems. *IEEE Transactions on Industrial Electronics*, 58(1), 29-36.
- [48] Kesraoui, M., Korichi, N., & Belkadi, A. (2011). Maximum power point tracker of wind energy conversion system. *Renewable Energy*, 36(10), 2655-2662.
- [49] Abdullah, M. A., Yatim, A. H. M., Tan, C. W., & Saidur, R. (2012). A review of maximum power point tracking algorithms for wind energy systems. *Renewable and Sustainable Energy Reviews*, 16(5), 3220-3227.
- [50] Dang, D. Q., Wu, S., Wang, Y., & Cai, W. (2010, October). Model predictive control for maximum power capture of variable speed wind turbines. In *IPEC, 2010 Conference Proceedings* (pp. 274-279). IEEE.
- [51] Mirzaei, M., Kj, N., & Niemann, H. H. (2012, June). Robust model predictive control of a wind turbine. In *2012 American Control Conference (ACC)* (pp. 4393-4398). IEEE.
- [52] Schlipf, D., Schlipf, D. J., & Kühn, M. (2013). Nonlinear model predictive control of wind turbines using LIDAR. *Wind Energy*, 16(7), 1107-1129.
- [53] Spencer, M. D., Stol, K. A., Unsworth, C. P., Cater, J. E., & Norris, S. E. (2013). Model predictive control of a wind turbine using short-term wind field predictions. *Wind Energy*, 16(3), 417-434.
- [54] Hovgaard, T. G., Larsen, L. F., Jørgensen, J. B., & Boyd, S. (2013, July). MPC for wind power gradients—utilizing forecasts, rotor inertia, and central energy storage. In *Control Conference (ECC), 2013 European* (pp. 4071-4076). IEEE.
- [55] Hovgaard, T. G., Boyd, S., & Jørgensen, J. B. (2015). Model predictive control for wind power gradients. *Wind Energy*, 18(6), 991-1006.
- [56] Henriksen, L. C., Poulsen, N. K., & Hansen, M. H. (2011). Nonlinear model predictive control of a simplified wind turbine. *IFAC Proceedings Volumes*, 44(1), 551-556.
- [57] Henriksen, L. C., Hansen, M. H., & Poulsen, N. K. (2012). Wind turbine control with constraint handling: a model predictive control approach. *IET Control Theory & Applications*, 6(11), 1722-1734.

- [58] Steurer, M., Bogdan, F., Ren, W., Sloderbeck, M., & Woodruff, S. (2007, June). Controller and power hardware-in-loop methods for accelerating renewable energy integration. In *Power Engineering Society General Meeting, 2007* (pp. 1-4). IEEE.
- [59] Bouscayrol, A. (2008, June). Different types of Hardware-In-the-Loop simulation for electric drives. In *2008 IEEE International Symposium on Industrial Electronics* (pp. 2146-2151). IEEE.
- [60] Song, S. H., Jeong, B. C., Lee, H. I., Kim, J. J., Oh, J. H., & Venkataramanan, G. (2005, March). Emulation of output characteristics of rotor blades using a hardware-in-loop wind turbine simulator. In *20th Annual IEEE Applied Power Electronics Conference and Exposition, 2005. APEC 2005*. (Vol. 3, pp. 1791-1796). IEEE.
- [61] Li, H., Steurer, M., Shi, K. L., Woodruff, S., & Zhang, D. (2006). Development of a unified design, test, and research platform for wind energy systems based on hardware-in-the-loop real-time simulation. *IEEE Transactions on Industrial Electronics*, 53(4), 1144-1151.
- [62] Neammanee, B., Sirisumrannukul, S., & Chatratana, S. (2007). Development of a wind turbine simulator for wind generator testing. *International Energy Journal*, 8(1), 21-28.
- [63] Munteanu, I., Bratcu, A. I., Bacha, S., Roye, D., & Guiraud, J. (2010). Hardware-in-the-loop-based simulator for a class of variable-speed wind energy conversion systems: Design and performance assessment. *IEEE Transactions on Energy Conversion*, 25(2), 564-576.
- [64] Muntean, N., Tutelea, L., Petrila, D., & Pelan, O. (2011, September). Hardware in the loop wind turbine emulator. In *International Aegean Conference on Electrical Machines and Power Electronics and Electromotion, Joint Conference* (pp. 53-58). IEEE.
- [65] Hardy, T., & Jewell, W. (2014). Hardware-in-the-loop wind turbine simulation platform for a laboratory feeder model. *IEEE Transactions on Sustainable Energy*, 5(3), 1003-1009.
- [66] Zhao, Y., Wei, C., Zhang, Z., & Qiao, W. (2013). A review on position/speed sensorless control for permanent-magnet synchronous machine-based wind energy conversion systems. *IEEE Journal of Emerging and Selected Topics in Power Electronics*, 1(4), 203-216.
- [67] COMSOL AB. COMSOL Multiphysics® v. 5.2. www.comsol.com.

- [68] COMSOL AB. (2015). *CFD Module User's Guide: Theory for Turbulent Flow Interfaces* (COMSOL Multiphysics® v. 5.2).
- [69] Wilcox, D. C. (1998). *Turbulence modeling for CFD* (Vol. 2, pp. 103-217). La Canada, CA: DCW Industries.
- [70] COMSOL AB. (2015). *Reference Manual* (COMSOL Multiphysics® v. 5.2).
- [71] Padrón, A. S., Alonso, J. J., Palacios, F., Barone, M., & Eldred, M. S. (2014). Multi-Fidelity Uncertainty Quantification: Application to a Vertical Axis Wind Turbine under an Extreme Gust. In *15th AIAA/ISSMO Multidisciplinary Analysis and Optimization Conference* (p. 3013).
- [72] International Electrotechnical Commission. (2005). IEC 61400-1: Wind turbines part 1: Design requirements. *International Electrotechnical Commission*.
- [73] Monteiro, J. P., Silvestre, M. R., Piggott, H., & André, J. C. (2013). Wind tunnel testing of a horizontal axis wind turbine rotor and comparison with simulations from two Blade Element Momentum codes. *Journal of Wind Engineering and Industrial Aerodynamics*, 123, 99-106.